Development of Ultra-Broadband Modulators

by

Orit A. Shamir

B.S. Electrical Engineering
Massachusetts Institute of Technology, 2007

Submitted to the Department of Electrical Engineering and Computer Science in partial fulfillment of the requirements for the degree of

Master of Engineering in Electrical Engineering and Computer Science

at the
MASSACHUSETTS INSTITUTE OF TECHNOLOGY

June 2008

Author . . . . . .
Orit A. Shamir
Department of Electrical Engineering and Computer Science
May 23, 2008

Certified by . . . . . .
Leslie A. Kolodziejski
Professor of Electrical Engineering and Computer Science
Thesis Supervisor

Accepted by . . . . . .
Arthur C. Smith
Chair, Department Committee on Graduate Students

Development of Ultra-Broadband Modulators

by

Orit A. Shamir

Submitted to the Department of Electrical Engineering and Computer Science
on May 23, 2008, in partial fulfillment of the
requirements for the degree of
Master of Engineering in Electrical Engineering and Computer Science

Abstract

Optical signal modulation is a cornerstone of communication, allowing the transfer of information by electrically encoding data onto an optical carrier. Modulation with ultra-broadband capability enables the generation of arbitrary waveforms using the electro-optic effect. By separating an incoming pulsed optical source into a frequency comb through the use of arrayed waveguide gratings, and employing both phase and amplitude modulation using Mach Zehnder Interferometers, an arbitrary waveform is constructed following frequency channel recombination.

Modulation of frequency combs centered at an operational frequency of 800nm requires the use of GaAs-based and InP-based materials that are transparent at 800nm. The design and growth of III-V structures, the fabrication of ultra-broadband modulators and the design of arrayed waveguide gratings are detailed in this work. Three distinct structures are presented along with a compatible fabrication procedure for the construction of discrete modulators. The work is culminated with a discussion of further steps in the realization of an optical arbitrary waveform generating system.

Thesis Supervisor: Leslie A. Kolodziejski
Title: Professor of Electrical Engineering and Computer Science

Acknowledgments

It only seems fitting that this thesis begins with the opportunity to thank all who have supported me and helped me push through the best and the worst of times.

My incredible advisor, Professor Leslie Kolodziejski, has given me the greatest of opportunities in making me part of her group. Her guidance and high spirits kept me grounded and focused, and her humor always provided relief from the daily stress. What I have learned from her extends far beyond the laboratory or classroom, and I cherish the experiences she has afforded me over the last two years.

Dr. Gale Petrich is truly one of the greatest resources at MIT. A day has yet to go by when I do not have a question to run by him, and the answers have always been more than helpful. I thank him for all the knowledge he has imparted to me, and for his generosity both in and out of the lab.

I would like to thank all who are involved in the Optical Arbitrary Waveform Generation project: Marcus Dahlem, Ali Motamedi, Dave Chao, Jason Sickler, Jeff Chen, Jonathan Morse, Michelle Sander, Professor Erich Ippen, Professor Franz Kaertner, and all others who are involved directly or indirectly. I am excited to be part of this effort and am looking forward to what the future (and a lot of hard work) will bring.

This work would not have been possible without my colleagues in the Nanostructures Laboratory (NSL) and the Microsystems Technology Laboratory (MTL). I want to thank Professors Henry Smith and Karl Berggren for granting me access to their laboratory as well as to their students, including but certainly not limited to Amil Patel, Trey Holzwarth, Euclid Moon, Bryan Cord, Sidney Tsai, Joel Yang, and Donald Winston, who are always willing to help. Jim Daley, who provides a wonderful work environment, great advice and whom I consider a great friend, cannot be thanked enough. He has contributed immensely to this project and to my experience at MIT. I am also very grateful to Dennis Ward for all his help and sense of humor.

I would like to acknowledge the wonderful students in the Integrated Photonics and Materials Group. I have had two amazing office mates, Ryan Williams and Ta-Ming Shih, who have put up with me in a window-less room for a year each and

with whom I have shared many laughs and conversations, and sometimes even a blackboard drawing. I also thank Reginald Bryant, Alex Grine, Natalija Jovanovic, Sheila Nabanja, Pei-Chun (Amy) Chi and Mohammad Araghchini. I could not wish for a better group.

Last, but certainly not least, I must thank my family and friends. To my mother and father, who have worked harder than anyone I know to give me the life and the love that I have, I cannot thank you enough. Their strength has kept me strong. I must thank my brothers, Erez and Oren, for their humor and perspective and the occasional e-mail that puts the smile back on my face. My grandparents, Rivka and Sami Haimof and Sarah and Petachia Shamir, who are an emblem to me of all that a person should be; they enrich my life. My friends, at MIT and abroad, have my gratitude for all the wonderful memories that I carry with me. To Tomer Levkov, whose support and devotion across the greatest of distances has meant more to me than words could ever possibly express.

Finally, to my country on its 60th birthday. Thank you.

Cambridge, 2008 O A S

Contents

List of Figures

List of Tables

Chapter 1

Introduction

Optical signal modulation is a cornerstone of communication, allowing the transfer of information by electrically encoding data onto an optical carrier. Modulation with ultra-broadband capability enables the generation of arbitrary waveforms using the electro-optic effect. By separating an incoming pulsed optical source into a frequency comb through the use of arrayed waveguide gratings, and employing both phase and amplitude modulation using Mach Zehnder Interferometers, an arbitrary waveform is constructed following frequency channel recombination.

Modulation of frequency combs centered at an operational frequency of 800nm requires the use of GaAs-based and InP-based materials that are transparent at 800nm. The design and growth of III-V structures, the fabrication of ultra-broadband modulators and the design of arrayed waveguide gratings are detailed in this work. Three distinct structures are presented along with a compatible fabrication procedure for the construction of discrete modulators. The fabrication process consists of four photolithography steps, reactive ion etching, metalization, planarization and passivation steps. The work is culminated with a discussion of future efforts in the realization of an optical arbitrary waveform generating system.

1.1 Thesis Organization

This thesis is organized as follows:

- Chapter two explains the modulation process, and presents different methods and designs by which it may be achieved.

- Chapter three commences with a report of the simulation tools used in this work, and progresses with a discussion on the engineering of the modulator epitaxial heterostructures. Finally, the mask design and its various details is addressed.

- Chapter four describes the fabrication process and distinct approaches taken. The final results and testing apparatus are also examined.

- Chapter five details the integration of modulators with arrayed waveguide gratings, and introduces new heterostructures with added advantages.

- Chapter six summarizes and concludes the thesis, and examines the direction in which future work can proceed.

Chapter 2

Background

Arbitrary waveform generation at a central wavelength of 800nm requires an incoming optical beam, in the form of a frequency comb generated by an ultra-short pulse laser, and a modulation device operating at 800 nm to accommodate a laser with that lasing wavelength (such as a Ti:sapphire laser). Material choices and device configuration are dictated by the requirement that the modulator be ultra-broadband and the selected method of modulation - the electro-optic effect. The frequency comb is separated into various frequency components that undergo phase and amplitude modulation and then recombined to produce the desired waveform.

Though optical signal modulation is a well-researched topic in the area of nonlinear optics, modulation of signals in the 800nm range remains relatively unexplored. This chapter provides an overview of the process of frequency comb generation and modulation techniques using a variety of effects explored in literature.

2.1 Frequency Combs

The laser, a light generating device and an acronym for Light Amplification by Stimulated Emission Radiation, is an important optical-electronic component of the integrated photonics field. Incoming light circulates within a laser comprised of a gain or amplifying medium situated inside a cavity. The medium is optically or electrically energized to efficiently excite atoms into higher energy states. The excited state

atoms eventually decay to lower energy states and release photons of a specific wavelength. These photons proceed to travel through the laser cavity, reflect off mirrors back into the cavity and stimulate the emission of more photons with the same phase and wavelength. At one end of the laser cavity, a mirror with slightly lower reflectivity allows a portion of the photons to exit the cavity, forming the output beam from the laser; the rest of the photons are reflected back into the cavity. The light released by the laser is very intense and may be tuned to a certain wavelength.

Some lasers, such as the titanium-doped sapphire laser used in this work (where the Ti:sapphire signifies the amplifying medium), have extremely large optical bandwidths on the order of THz and can generate ultrashort, femtosecond pulses through a technique known as mode locking. The mode locking ability allows the laser to generate pulse trains in the time domain that translate into a spectrum of equidistant discrete lines in the frequency domain known as a frequency comb. A simplified discussion of the generation of frequency combs is included in this section, but the works of Riehle [7], Cundiff and Ye [1], and Cundiff et. al. [8] may be consulted for more information.

2.1.1 Time Domain

An optical pulse generated by a laser in the time domain is formed by the multiplication of a carrier wave, in the form of an oscillating sine wave, and an envelope function. When the envelope has a repeating pattern (such as a square wave), the multiplication of the carrier and the envelope function yields a train of pulses in the time domain, as shown in the top image of Figure 2-1 [1]. The pulses repeat every T_{rep} as determined by

$$T_{rep} = l_c/v_g \tag{2.1}$$

where l_c is the length of the laser cavity and v_g is the round trip group velocity. The cavity length-dependent repetition rate can be amplified by mode-locking the laser using a Fabry-Perot grating-lens cavity. By connecting the output of the Fabry-Perot cavity to the input of the semiconductor laser, the pulse circulation path is

lengthened, increasing T_{rep} [9].

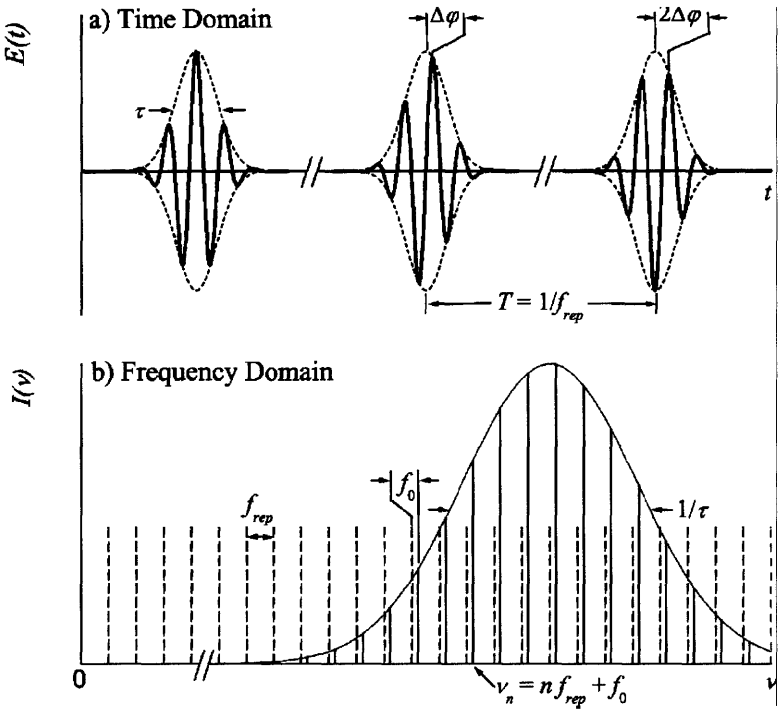

Figure 2-1: Optical pulse generation (top) by envelope superposition over a carrier wave in the time domain, and resultant frequency comb generation (bottom) in the frequency domain [1]. The pulse are separated in time by T_{rep}

2.1.2 Frequency Domain

After applying a Fourier Transform over time to a given pulse train, its optical spectrum consists of equally spaced, distinct lines in the frequency domain. The line spacing of the frequency comb, as seen in the bottom image of Figure 2-1, is given by $f_{rep} = 1/T_{rep}$. Ideally, the phase and group velocities, v_p and v_g, within the laser cavity would be identical, so that the phase shift between pulses would be $\Delta\phi = 0$ through

$$\Delta\phi = \left(\frac{1}{v_g} - \frac{1}{v_p}\right) l_c \omega_c \cdot mod\, 2\pi \tag{2.2}$$

for a carrier frequency of ω_c. However, dispersion exists within the cavity such that $v_p \neq v_g$, creating an offset $\Delta\phi$ as observed in the time domain in Figure 2-1. As a

result, a comb offset of

$$f_0 = \frac{1}{2\pi} f_{rep} \Delta\phi \tag{2.3}$$

is experienced. Hence, the comb line optical frequencies, υ_n, centered at ω_c are described by [1]

$$\upsilon_n = n f_{rep} + f_0 \tag{2.4}$$

where the large integer n is used for indexing the comb lines. The frequency combs that are generated by the Ti:Sapphire laser at its maximum efficiency at 800nm, provide the input signal to be modulated.

2.2 Modulation Methods

Modulation is the process of superimposing information on a carrier wave. Optical modulation, which uses an optical beam as a carrier, is accomplished by varying the properties of the incoming signal, namely the amplitude, phase, frequency or polarization of the light. The amplitude of an optical signal traveling through a medium is altered by a change in the material's intensity absorption coefficient, α, while the phase, frequency and polarization are related to the refractive index of the material within the modulator. The refractive index of a material describes the phase velocity decrease in relation to the velocity of light in vacuum. The absorption coefficient and refractive index, n, are related through the Kramers-Kronig relation written in Equation 2.5 as

$$n(\omega) = \frac{c}{\pi} \int_0^\infty \frac{\alpha(\omega')}{\omega'^2 - \omega^2} d\omega' \tag{2.5}$$

where c is the speed of light, ω' represents the varying frequencies over which integration is performed and ω the frequency of interest. The equation suggests that in order to modulate a signal by varying its amplitude or phase, a change in either the α or n of the medium must be induced. Changes in either the absorption or index of refraction of a material (or in some cases, both) are achieved by four different effects:

Franz-Keldysh, Stark, Quantum-confined Stark and the electro-optic effect.

2.2.1 Franz-Keldysh Effect

Every semiconductor material has a unique energy band profile. The energy levels are separated into two ranges. The lower energy range within the structure is the valence band, shown schematically in Figure 2-2 as the lower line with energy $\mathcal{E}_v$. This line corresponds to the highest of the possible energy states within the valence band. The higher energy range is the conduction band, depicted as the upper line with energy $\mathcal{E}_c$, which corresponds to the lowest of all possible energy states in this band.

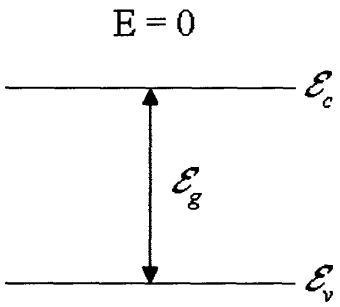

Figure 2-2: A simple energy band diagram of a generic crystal with no applied electric field. The valence band, depicted by the lower line, represents the highest energy level of the lower energy range. The conduction band, depicted by the upper line, represents the lowest energy level of the higher energy range. The gap between them is the bandgap, which has energy of $\mathcal{E}_g$.

The gap between the valence and conduction bands is known as the energy bandgap. The bandgap, $\mathcal{E}_g$, represents the amount of energy required to break a bond in the crystal. When an electric field is applied, the band structure undergoes band bending, as portrayed in Figure 2-3, creating a tunneling barrier for the valence electrons. The barrier is an area of height, h, and width, x, where

$$h = \mathcal{E}_g \tag{2.6}$$

$$x = \frac{\mathcal{E}_g}{qE} \tag{2.7}$$

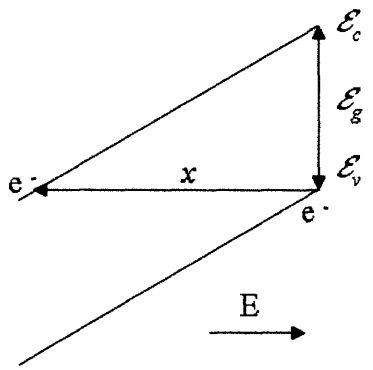

Figure 2-3: Energy band diagram of a generic crystal with an applied electric field of strength E. The field induces band bending, creating an area of height, h, and width, x, through which a valence electron can tunnel.

and E is the applied electric field. The electric field not only changes the band diagram, but induces an increase in absorption below the band edge, allowing electrons to be excited into the higher energy conduction band from the lower energy valence band by the absorption of a photon with an energy of $\hbar\omega < \mathcal{E}_g$.

The absorption of a photon reduces the height and width of the tunneling area to

$$h' = \mathcal{E}_g - \frac{\hbar c}{\lambda} = \mathcal{E}_g - \hbar\omega \tag{2.8}$$

$$x' = \frac{\mathcal{E}_g - \hbar\omega}{qE} \tag{2.9}$$

so that an electron may now tunnel through a smaller area, as shown in Figure 2-4.

The electric-field induced change in a medium's optical absorption of photons that satisfy $\hbar\omega < \mathcal{E}_g$ is known as the Franz-Keldysh effect. An electroabsorption modulator that operates on this principle is able to alter the amplitude or the intensity of an incoming signal in relation to $\Delta\alpha$. However, modulation demands a significant increase in α that may only occur under very strong electric fields ($\alpha \approx 0$ at fields on the order of 10^6 V/m for photon energies far below the bandgap, but increases to $\Delta\alpha = 2000$ cm^{-1} for fields on the order of $2.5 \cdot 10^7$ V/m [10]). Modulators based on the Franz-Keldysh effect exhibit fast switching capability and insensitivity to temperature variations as a result of the large spectral width of $\Delta\alpha$ [11].

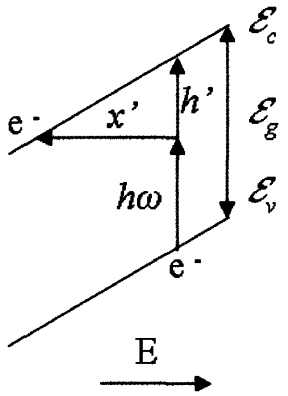

Figure 2-4: Tunneling of an electron by the absorption of a photon. The applied electric field, E, increases the absorption coefficient, α, which in turn allows the absorption of a photon.

In addition to changing the absorption coefficient, the Franz-Keldysh effect also alters the refractive index of a semiconductor material. Similar to $\Delta\alpha$, the index change, or Δn, also has a strong dependence upon the difference between $\hbar\omega$ and $\mathcal{E}_g$ as well as the electric field strength, E. Variations in the refractive index, generated by electrorefraction, can be used to modulate the phase of an incoming signal. Though electrorefraction is quite stable within the bandgap, electroabsorption becomes more prominent at the band edge and reduces the efficiency of the modulation [12]. In order to determine the utility of electrorefraction, the figure of merit $\frac{\Delta n}{\Delta k}$ is used, where Δn and Δk are the real and imaginary parts of the change in refractive index respectively. k is known as the extinction coefficient and is linked to α through

$$\alpha = \frac{4\pi k}{\lambda} \tag{2.10}$$

In designing an amplitude modulator, a figure of merit of $\frac{\Delta n}{\Delta k} \approx 1$ is desired in order to maximize absorption, while a figure of merit of $\frac{\Delta n}{\Delta k} > 1$ is desired for phase modulators. The former is obtained by applying higher electric fields and choosing an operational wavelength range that is farther from the absorption edge [13], while the latter is achieved by choosing a wavelength range that is closer to the absorption edge.

2.2.2 Stark Effect

Electron orbitals within the same atom will exhibit different orientations in the presence of an electric field of strength E. The inconsistency in orientation across the orbitals prompts energy level splitting, referred to as the Stark effect, that typically affects the outer electron orbitals. The energy shift experienced by the orbitals is expressed by

$$\Delta\mathcal{E} = qdE \tag{2.11}$$

where d is the orbit eccentricity.

2.2.3 Quantum-Confined Stark Effect

Quantum well (QW) structures, often incorporated in the realization of lasers and modulators, consist of a thin semiconductor layer situated between two wider bandgap semiconductor materials. The wide bandgap material confines the carrier motion and leads to a potential well in the direction perpendicular to the plane of the semiconductor. Figure 2-5 demonstrates the energy band structure of a QW without an applied electric field. $\mathcal{E}_e$ and $\mathcal{E}_h$ represent the electron and hole subband energy levels respectively (as well as the conduction and valence band offsets), $\mathcal{E}_{gw}$ is the well bandgap energy and L_w is the well width. Exciton effects that occur due to a Coulombic interaction between an electron in the conduction band and a hole in the valence band are negligible in bulk semiconductors but affect the quantum well structure, where carrier confinement by the wider bandgap material increases the electron and hole wave function overlap. As a result, the structure experiences far stronger exitonic resonances below the bandgap due to enhanced electron-hole binding energy and increased absorption above the well bandgap.

The effects of an electric field on the exciton behavior is dependent upon the direction in which the field is applied. If the field is applied parallel to the layers, the direction in which the carriers are not confined, the electron and hole will easily separate, leading to the ionization of the exciton. However, a field applied perpendicular to the layers, the dimension in which the wave functions are contained, would not

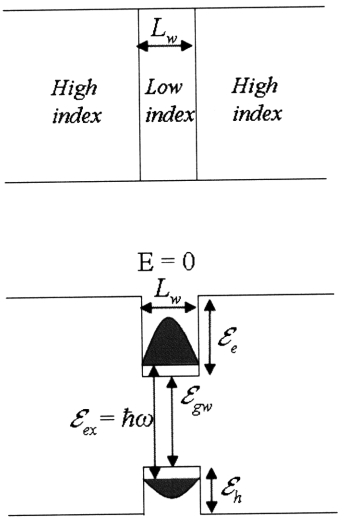

Figure 2-5: Layer structure and corresponding energy band diagram of a quantum well at ground state. The top and bottom grey-filled areas represent the electron and hole wave functions respectively.

elicit the ionization of an exciton. In this case, the structure behaves according to the Stark effect mentioned previously.

The effects of a perpendicularly applied electric field of strength E upon a quantum well energy band structure are shown in Figure 2-6. In addition to the band bending, both the electron and hole wave functions are separated and pulled to opposite walls in the well, as displayed in Figure 2-7 [2]. The heavy holes exhibit a stronger reaction than electrons to an applied electric field due to their heavier mass and lower energy barrier [14]. Though the electron-hole Coulombic attraction is maintained, their binding energy is reduced by the wave function separation. A change in the intersubband separation (effectively, the energy of the bandgap of the quantum well, $\mathcal{E}_{gw}$), however, counters the binding energy reduction. The shifting of the wave functions creates a smaller overlap between them, which in turn reduces the absorption in relation to the band edge. At this point, the Stark effect, enhanced by the presence of bound excitons, dominates over the slight changes in intersubband energy, resulting in a small change in the quantum well bandgap energy, $\mathcal{E}_{gw}$. In the quantum-confined Stark effect, named after the specific case for which the Stark

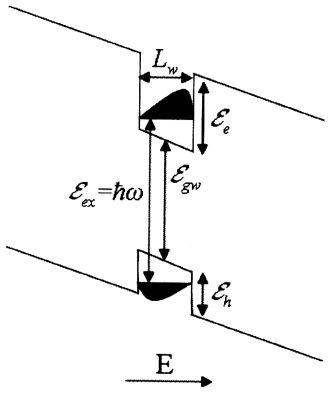

Figure 2-6: Energy band diagram of a quantum well in the presence of an applied electric field of strength E. The field induces band bending as well as shifting of the electron and hole wave functions.

effect occurs in quantum wells, an increase in electric field strength results in 1) a decrease of $\mathcal{E}_{gw}$, 2) a shifting of the absorption spectrum to longer wavelengths (lower energy) as shown in Figure 2-8 [2] and 3) an induced change in the refractive index, n, close to the absorption edge. To produce a sufficiently large Δn, as required for phase modulation, the absorption spectrum should be moved further into the band edge where absorption is reduced.

Changes in n, as a result of $\Delta\alpha$, are determined through the Kramer-Kronig relation that was previously discussed in Section 2.5. In Figure 2-9, Thistrup [3] identifies three types of shifts in α, induced by an electric field, and the corresponding change in n that occurs as a result. In the first case, the introduction of an electric field causes a shift in the absorption edge from a shorter (λ_2) to a longer wavelength (λ_3), presented in the top plot of Figure 2-9 (a). The change in the refractive index corresponding to this specific situation is expressed by

$$\Delta n_I(\lambda) = \frac{\lambda}{4\pi^2}\alpha_1 \ln\frac{(\lambda+\lambda_3)(\lambda-\lambda_2)}{(\lambda-\lambda_3)(\lambda+\lambda_2)} \tag{2.12}$$

The resulting transformation in Δn (as shown in the bottom plot of the same figure)

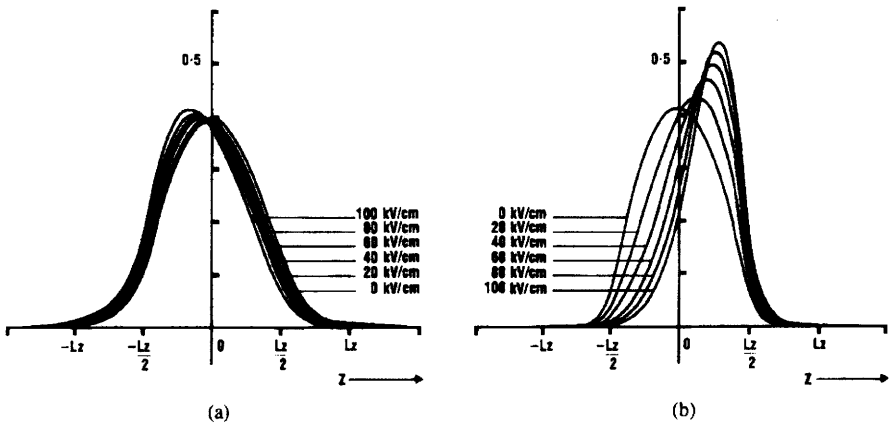

Figure 2-7: Plot of normalized wave functions in the presence of varying electric fields of a L_z=10.5 nm well, obtained by G. Lengyel et al [2]. The electron wave function in (a) and the heavy hole wave function in (b) can be seen shifting with increasing electric field strength.

is a positive one. In the second case, the change in refractive index is described by

$$\Delta n_{II}(\lambda) = -\frac{\lambda}{4\pi^2}(\alpha_1 - \alpha_2) \ln \frac{(\lambda + \lambda_2)(\lambda - \lambda_1)}{(\lambda - \lambda_2)(\lambda + \lambda_1)} \tag{2.13}$$

The reduction in α is induced by an electric field within the wavelength range of λ_1 to the longer wavelength λ_2. The subsequent change in n [presented in the bottom plot of Figure 2-9 (b)] is negative according to Equation 2.13.

The final case, presented in Figure 2-9 (c), of absorption change is a combination of the first two cases. The absorption edge undergoes both a shift from λ_2 to λ_3 as well as a reduction in α in the wavelength range between λ_1 and λ_2. The combined effects of the the two scenarios yields an expression for the change in the index of refraction given by

$$\Delta n_{III}(\lambda) = \Delta n_I(\lambda) + \Delta n_{II}(\lambda) \tag{2.14}$$

where $\Delta n_I(\lambda)$ and $\Delta n_{II}(\lambda)$ represent the changes in the index of refraction as a result of a shift in the absorption spectrum in case I and reduced absorption in case II respectively.

The quantum well width of quantum-confined Stark effect-based modulators must

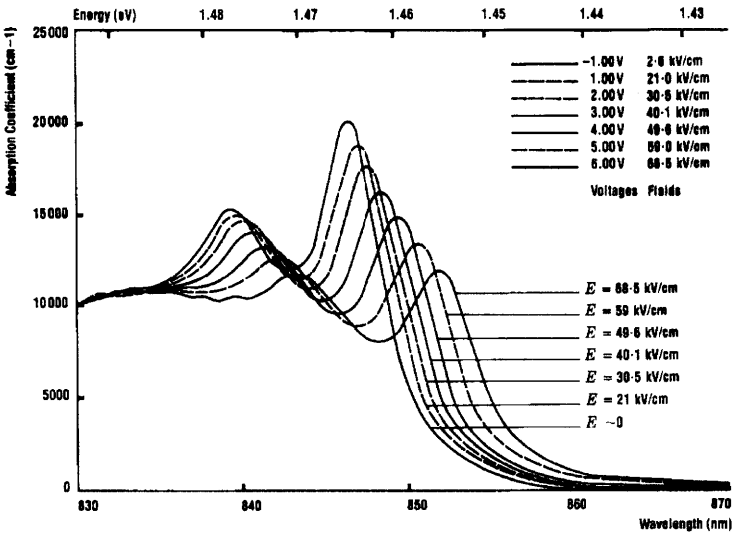

Figure 2-8: Absorption spectra measurements of a L_z=10.5 nm well, obtained by G. Lengyel et al [2] as a function of applied electric field.

be chosen wisely. A smaller width, L_w, will yield a larger α which is beneficial for an amplitude modulator. However, if the well is too thin, both the electron and hole wave functions will spread beyond the low index layer, reducing their overlap and consequently reducing α as well. On the other hand, a wide quantum well would improve the Stark shifting, but would weaken the electron-hole interaction and exciton binding energy [15]. With these considerations in mind, Tobin and Bruno [16] adopted two approaches in designing a modulator operating at 810nm. The first technique involves embedding low Al content $Al_xGa_{1-x}As$ layers between $Al_{0.3}Ga_{0.7}As$ layers, and preserving the Stark shift by designing wide quantum wells. An appropriate choice for Al content x in the quantum layers will move the photon transition energy to the desired 810nm. The transition energy, $\mathcal{E}_{ph}$, is given by

$$\mathcal{E}_{ph} = \mathcal{E}_e + \mathcal{E}_h + \mathcal{E}_{gw} - \mathcal{E}_{ex} \tag{2.15}$$

The second method taken to design such a modulator uses several GaAs quantum wells separated by thin $Al_{0.3}Ga_{0.7}As$ layers in order to create one effective quantum well that is sufficiently large for Stark shifting. The coupling between GaAs quantum

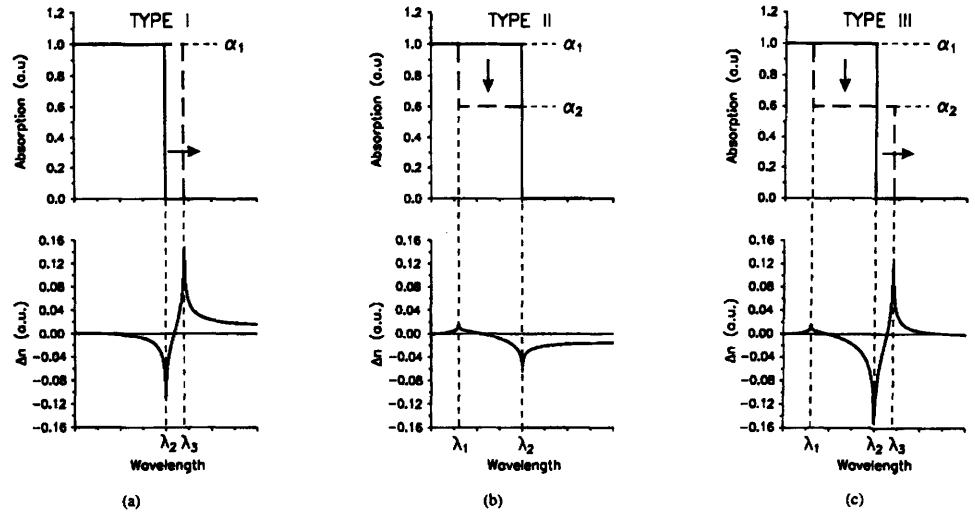

Figure 2-9: Comparison of the absorption coefficient by Thirstup [3] (top images) during material excitation (dashed line) and no excitation (solid), and corresponding effects on the index of refraction (bottom images) in three different cases. In (a), the absorption edge is shifted from a shorter λ_2 to a longer wavelength λ_3. In (b), a change in α is induced by an electric field specifically within the wavelength range of λ_1 to the longer wavelength λ_2. In (c), absorption change is a combination of the first two.

wells can then be modified to alter the photon transition energy in the modulator heterostructure until 810nm is achieved.

2.2.4 Electro-optic Effect

Within a medium, the constitutive relation

$$\vec{D} = \epsilon_0 \vec{E} + \vec{P} \tag{2.16}$$

describes the dependence of the electric displacement vector, $\vec{D}$, on the electric field vector, $\vec{E}$, and polarization vector, $\vec{P}$. The permittivity of free space, ϵ_0 is related to the dielectric tensor through

$$\epsilon_{ij} = \epsilon_0(1 + \chi^e_{ij}) \tag{2.17}$$

where χ_{ij}^{e} is the susceptibility tensor which is dependent upon crystal structure. When no electric field is applied, ϵ_0 is linked to the n of an anisotropic crystal by

$$n = \sqrt{\frac{\epsilon\mu}{\epsilon_0\mu_0}} \tag{2.18}$$

for permeability μ and free-space permeability μ_0. In non-magnetic materials as in the case of most compounds, $\mu = \mu_0$.

In an isotropic medium, $\overrightarrow{D}$ and $\overrightarrow{E}$ are parallel and the refractive index value is the same in all axes. In an anisotropic medium, an incoming beam breaks down into two components - the ordinary and extraordinary waves - by double refraction. The two wave types travel with differing speeds on different paths with distinct indices of refraction. Consequently, $\overrightarrow{D}$ and $\overrightarrow{E}$ are not parallel, and the refractive index is not equal in all axes. An example of double refraction is depicted in Figure 2-10 for the case of a uniaxial material, where $n_x = n_z$ while n along the y axis differs. The

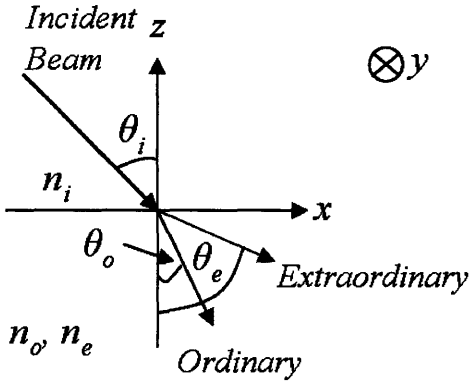

Figure 2-10: Split of an incident beam into ordinary and extraordinary rays in a uniaxial crystal.

ordinary component of the incoming beam is polarized in the y direction and the extraordinary wave is polarized in the xz plane. In a uniaxial crystal, two of the axes have identical indices of refraction called the ordinary index, n_o, and obey Snell's law

$$n_o \sin\theta_o = n_i \sin\theta_i \tag{2.19}$$

for the angle of refraction of the ordinary wave (θ_o), the angle of the incoming beam (θ_i) and the refractive index (n_i) of the medium through which the incoming beam travels. The index of refraction of the third axis is the extraordinary index, n_e, calculated by

$$\frac{1}{n_e^2} = \frac{\cos^2\theta_e}{n_x^2} + \frac{\sin^2\theta_e}{n_z^2} \tag{2.20}$$

with θ_e representing the angle of refraction of the extraordinary wave. The general case of a biaxial crystal (for which all axes have different indices) is expressed as an index ellipsoid of the form

$$\frac{x^2}{n_x^2} + \frac{y^2}{n_y^2} + \frac{z^2}{n_z^2} = 1 \tag{2.21}$$

describing the birefringence within such a medium.

As in the Franz-Keldysh effect, the introduction of an electric field modifies a material's n. However, since there are no carriers, and therefore, no absorption that was present in the Franz-Keldysh effect, both phase and amplitude modulation rely upon an induced Δn. This type of modulation is known as transverse electro-optic modulation, as the applied electric field is perpendicular to an incoming light beam, and is accomplished through the use of the electro-optic effect.

With the application of an electric field of strength E, the index ellipsoid takes on the altered form of

$$(\frac{1}{n_x^2}+\Delta\frac{1}{n_x^2})x^2+(\frac{1}{n_y^2}+\Delta\frac{1}{n_y^2})y^2+(\frac{1}{n_z^2}+\Delta\frac{1}{n_z^2})z^2+\Delta\frac{1}{n_{yz}^2}2yz+\Delta\frac{1}{n_{xz}^2}2xz+\Delta\frac{1}{n_{xy}^2}2xy = 1 \tag{2.22}$$

where n_i is the induced index of refraction in a distinct axis or plane i. With no applied electric field, all $\Delta\frac{1}{n_i^2} = 0$ and the equation is reduced to Equation 2.21. The change in n with respect to the applied electric field is defined by the Kerr effect as follows:

$$\Delta\frac{1}{n_i^2} = r^l E + s^q E^2 \tag{2.23}$$

When r^l, the linear electro-optic coefficient, is much larger than s^q, the quadratic electro-optic coefficient, the first term dominates and the relationship between the

applied electric field along each axis and material impermittivity becomes

$$\Delta\frac{1}{n_i^2} = \sum_{j=1}^{3} r_{ij}E_j \tag{2.24}$$

where r_{ij} is the electro-optic tensor matrix. This is the linear case of the electro-optic effect known as the Pockels effect, and may also be written in matrix-form:

$$\begin{pmatrix} \Delta\frac{1}{n_x^2} \\ \Delta\frac{1}{n_y^2} \\ \Delta\frac{1}{n_z^2} \\ \Delta\frac{1}{n_{yz}^2} \\ \Delta\frac{1}{n_{xz}^2} \\ \Delta\frac{1}{n_{xy}^2} \end{pmatrix} = \begin{pmatrix} r_{11} & r_{12} & r_{13} \\ r_{21} & r_{22} & r_{23} \\ r_{31} & r_{32} & r_{33} \\ r_{41} & r_{42} & r_{43} \\ r_{51} & r_{52} & r_{53} \\ r_{61} & r_{62} & r_{63} \end{pmatrix} \begin{pmatrix} E_1 \\ E_2 \\ E_3 \end{pmatrix}$$

For GaAs, an isotropic cubic crystal with four-fold symmetry of group $\bar{4}3$ that lacks inversion symmetry, r_{ij} is reduced to

$$\begin{pmatrix} 0 & 0 & 0 \\ 0 & 0 & 0 \\ 0 & 0 & 0 \\ r_{41} & 0 & 0 \\ 0 & r_{52} & 0 \\ 0 & 0 & r_{63} \end{pmatrix}$$

where $r_{41} = r_{52} = r_{63}$ for isotropic materials. In a uniaxial material, $r_{41} = r_{63}$ but the y axis coefficient remains as r_{52}. For a y-directed electric field in a uniaxial system, Δn is

$$\Delta\frac{1}{n_{xz}^2} = r_{52}E_y \tag{2.25}$$

and Equation 2.22 reduces to

$$\frac{x^2}{n_o^2} + \frac{y^2}{n_e^2} + \frac{z^2}{n_o^2} + 2r_{52}E_y xz = 1 \tag{2.26}$$

A comparison between Equation 2.21 and Equation 2.26 reveals a mixed term, $2r_{52}E_y xz$. The applied electric field E_y distorts and rotates the ellipsoid from a circle

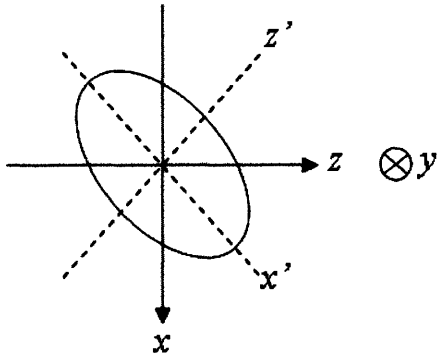

Figure 2-11: Index ellipsoid under an applied electric field in the y-direction.

in the xz plane to the ellipsoid rotated by an angle θ off the xz plane (shown in Figure 2-11). When $n_x = n_z$ and $\Delta\frac{1}{n_x^2} = \Delta\frac{1}{n_z^2} = 0$, then $\theta = 45°$ [17]. A new coordinate system is developed using new principle axes x', y' and z' defined by

$$x = x' \cos\frac{\pi}{4} - z' \sin\frac{\pi}{4} = \frac{x'}{\sqrt{2}} - \frac{z'}{\sqrt{2}} \tag{2.27}$$

$$z = x' \sin\frac{\pi}{4} + z' \cos\frac{\pi}{4} = \frac{x'}{\sqrt{2}} + \frac{z'}{\sqrt{2}} \tag{2.28}$$

$$y = y' \tag{2.29}$$

Using Equations 2.27 and 2.28,

$$xz = \frac{x'^2}{2} - \frac{z'^2}{2} \tag{2.30}$$

and the mixed term due to the electric field is transformed into the expression

$$2r_{52}E_y xz = r_{52}E_y(x'^2 - z'^2) \tag{2.31}$$

The former x and z axis terms in Equation 2.21 are also transformed into

$$\frac{x'^2}{n_o^2} + \frac{z'^2}{n_o^2} \tag{2.32}$$

The combination of Equations 2.26, 2.31 and 2.32 yields a new expression for the index ellipsoid associated with the new principal axes:

$$(\frac{1}{n_o^2} + r_{41}E_y)x'^2 + \frac{y^2}{n_y^2} + (\frac{1}{n_o^2} - r_{52}E_y)z'^2 = 1 \tag{2.33}$$

Equation 2.33 has the same form seen previously in Equation 2.22, so it may be inferred that

$$\Delta\frac{1}{n^2} = r_{52}E_y \tag{2.34}$$

and therefore n'_x and n'_z may be written as

$$n'_x = n_0 + \Delta n \tag{2.35}$$

and

$$n'_z = n_0 - \Delta n \tag{2.36}$$

By linearization, the following expression for the field-induced change in the index of refraction is derived:

$$\Delta n = -\frac{1}{2}n^3\Delta\frac{1}{n^2} = -\frac{1}{2}n^3 r_{52}E_y \tag{2.37}$$

Finally, Equation 2.37 is applied to the former expressions for n'_x and n'_z to obtain

$$n'_x = n_0 - \frac{1}{2}n^3 r_{52}E_y \tag{2.38}$$

and

$$n'_z = n_0 + \frac{1}{2}n^3 r_{52}E_y \tag{2.39}$$

Now that the electric field effect on the refractive indices of different axes is known,

the electric field and voltage required to achieve a desired phase modulation can also be calculated. Figure 2-12 shows a basic waveguide with top and bottom electrodes to which a voltage V is applied, creating an electric field, E_y, oriented along the y axis. When an electric field is applied to a GaAs-based modulator along a distinct

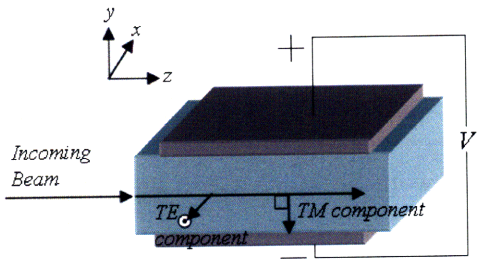

Figure 2-12: Basic waveguide modulator operating on the electro-optic effect. An applied voltage V creates an electric field, E_y, that induces a Δn in the x and z axes.

axis, the other two axes will show a change in refraction. In this case, the applied electric field E_y results in induced n'_x and n'_z.

An incoming beam directed along the z axis has a TE component along the x axis and a TM component along the y axis. Hence, the TE mode will be affected by the modified n'_x, while the TM mode lying on the same axis as the electric field, will not feel the effects of a Δn. As a result, only the TE mode of the beam will undergo modulation, reducing the device efficiency [18].

In general, the expression for the total phase shift of a beam traveling along the z axis, associated with a normal electric field in the y axis, is

$$\Delta\phi = k_0 L \Delta n = \frac{2\pi}{\lambda} \frac{L n^3 r_{52} E_y}{2} \tag{2.40}$$

where k_0 is a wavevector equal to $\frac{2\pi}{\lambda}$, L is the modulator length and λ is the wavelength of operation. The voltage applied yielding E_y is given by

$$V = E_y \cdot t_g \tag{2.41}$$

where t_g is the height or thickness of the active region of the modulator. Therefore,

the phase shift achieved by a certain applied voltage V is obtained through

$$\Delta\phi = \frac{\pi}{\lambda}\frac{Ln^3 r_{52} V}{t_g} \tag{2.42}$$

Consequently, a phase shift of $\phi = \frac{\pi}{2}$ for example, requires a voltage of

$$V_{\frac{\pi}{2}} = \frac{\lambda}{2}\frac{t_g}{Ln^3 r_{52}} \tag{2.43}$$

and a phase shift of $\phi = \pi$ would require a voltage of

$$V_{\pi} = \lambda\frac{t_g}{Ln^3 r_{52}} \tag{2.44}$$

The TE and TM components of an incoming optical beam travel along the x and z axes respectively. If $n_x \neq n_z$ in the modulator structure, the TE and TM components will acquire different phase velocities due to the differing indices of refraction along each axis of polarization, a phenomenon known as birefringence. Modulators have a natural birefringence by virtue of their structural design computed by

$$n_{birefringence} = n_{TE} - n_{TM} \tag{2.45}$$

where n_{TE} and n_{TM} are the TE and TM mode indices respectively. In bulk modulators of isotropic materials such as GaAs, $n_e = n_o$ and there is no natural birefringence. However, in heterostructures and uniaxial crystals where $n_e \neq n_o$, $n_{birefringence}$ does exist and often dominates over the induced index change. Though this effect is useful in polarization modulation, $n_{birefringence}$ should be minimized for both phase and amplitude modulation so that TE and TM modes are similarly modulated. Minimization of birefringence is accomplished by designing a structure with a near-uniform material arrangement, so that the mode is surrounded by the same layer configuration along its extraordinary and ordinary axes.

Efficient modulator design is associated with lower operating voltages and minimal device dimensions. Consideration of the wafer crystal orientation is critical in

determining the placement of devices on the sample. Correct alignment of devices with the x' and z' axes will allow maximal modulation of the TE component of an entering optical beam. Device alignment with crystal orientation also controls the quality of the cleave. Consequently, devices aligned to the x' and z' axes will result in cleaner and easier cleaving of the wafer.

2.3 Modulation Structures

In addition to several modulation methods, there are also structures that may be employed to produce phase changes. Fabry-Perot interferometers and coupled-waveguide devices both offer techniques for phase modulation, that in-turn can result in intensity modulation. This work focuses on the use of Mach-Zehnder interferometers that translate phase modulation to changes in signal amplitude by light wave interference.

2.3.1 Mach-Zehnder Interferometers (MZIs)

In a Mach-Zehnder interferometer, a light beam entering from a passive waveguide is split into two components which then travel along two optical paths and recombine at the output as depicted in Figure 2-13. If the path lengths are identical, the beams will be in phase at the output and interfere constructively. However, when the path lengths vary, a phase difference between the two beams will be introduced and affect the total power at the output. The path length can be changed by applying a voltage across

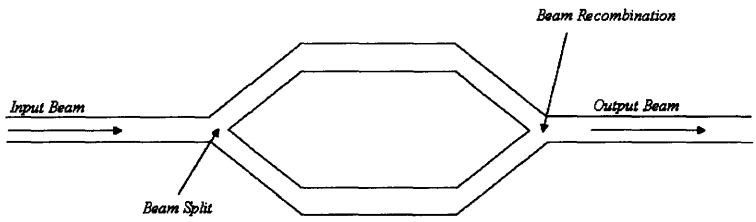

Figure 2-13: Mach-Zehnder interferometer that uses the interference of split beam components to produce a change in total beam intensity. The beam splitter in this particular case is a Y-splitter.

one or both of the arms (as shown in Figure 2-14), thereby creating active waveguide regions. The electric field causes a relative phase change between the two arms that results in intensity modulation at the output. If, for instance, a voltage is applied to one arm corresponding to $\Delta\phi = \pi$, the relative phase difference between the two beams will also be π. In this case, a single-mode output waveguide that supports only first-order modes will exhibit a resulting intensity of zero for that mode. All light corresponding to unsupported modes will dissipate by radiating into the substrate [19, 20]. The interferometer may also be used with a push-pull drive by powering one

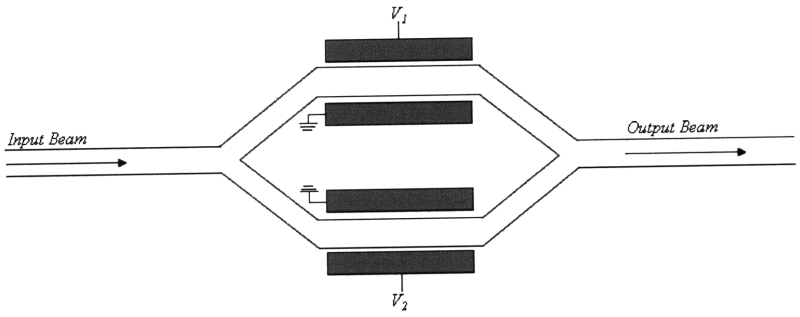

Figure 2-14: Mach-Zehnder interferometer with electrodes over both arms. The path length will vary with applied voltage and affect the total output power.

arm with positive voltage and the other with negative voltage. This technique has the added benefits of doubling device efficiency and reducing the required active arm length by two [21].

Chapter 3

Design

The ultra broadband modulators developed in this work operate according to the electro-optic effect described in Section 2.2.4. The electro-optic effect has been chosen due to the large optical bandwidth requirement of the structure (approximately 650nm - 950nm) for which an electroabsorption-based effect would not have been sufficient. Furthermore, the effect relies upon changes in the index of refraction, n, as opposed to the absorption, α, which involves carriers. Therefore, no loss due to free carrier absorption is expected (carriers present in the contact layers are optically negligible).

The design of such modulators combines multiple aspects, from considerations of mode confinement and TE/TM mode properties to material choices and device voltage requirements. Calculations of mode propagation and behavior are essential in order to determine specific waveguide lengths and radius of curvature as well as potential losses involved, and to proceed to the next step of designing a mask, and ultimately, fabricating the device.

3.1 Optical Simulation

Commercial simulation software was used to model the mode properties and to determine the mode confinement capability of a specific layered structure. Optical simulations allow the user to vary materials and thicknesses and resolve their effects on mode behavior. In addition, mode propagation through waveguide bends was

simulated for different bend radii. The information provided by simulation software is critical in device and material design, and requires a discussion of the calculation methods employed in the programs.

3.1.1 3-D Mode Solver

The computation of mode properties is an imperative first step in the process of modulator design. Simulations provide information regarding a heterostructure's effective index of refraction and waveguide capabilities in supporting first-order modes only. The Optiwave software programs, OptiBPM 5.2 and OptiBPM 6.0, were employed in modeling a modulator layer structure, Y-splitters and multimode interferometers (MMIs). The simulations are based upon the beam propagation method (BPM) with alternating direction implicit (ADI) method that solve the semivectorial Helmholtz equation. The software provides mode eigenfunctions and propagation constants, and outputs numerical modal effective indices and fields as well as their graphical representations. This section provides an overview of the methods used in OptiBPM 6.0 to calculate modal indices. The reader is referred to references [22, 23] for a more detailed explanation.

A scalar electric field is separated into its space and time components through $E(x,y,z,t) = \phi(x,y,z)e^{-j\omega t}$. The Helmholtz equation for steady state (and inclusive only of the spatial component ϕ of the electric field) is given by

$$\frac{\partial^2\phi}{\partial x^2} + \frac{\partial^2\phi}{\partial y^2} + \frac{\partial^2\phi}{\partial z^2} + k(x,y,z)^2\phi = 0 \tag{3.1}$$

where the wavenumber $k(x,y,z) = k_0 n(x,y,z) = \frac{2\pi}{\lambda}[n(x,y,z)]$, related the refractive index distribution $n(x,y,z)$ with applied electric field. Phase variation caused by propagation along the z-axis accounts for the fast variation in ϕ. As a result, the field may be depicted as a slow-varying envelope field $u(x,y,z)$ by separating the field from phase variation through the approximation

$$\phi(x,y,z) = u(x,y,z)e^{j\bar{k}z} \tag{3.2}$$

with the reference wavenumber $\bar{k}$ representing average variation in the phase of the field ϕ. Similar to k, $\overline{k}$ is related to the reference refractive index $\overline{n}$ through $\overline{k} = k_0\overline{n}$. The Helmholtz equation in combination with Equation 3.2 for a slow-varying field u yields the form

$$\frac{\partial^2 u}{\partial x^2} + \frac{\partial^2 u}{\partial y^2} + \frac{\partial^2 u}{\partial z^2} + 2j\overline{k}\frac{\partial u}{\partial z} + (k^2 - \overline{k}^2)u = 0 \tag{3.3}$$

If field variation along the z axis is assumed to be sufficiently slow, so that $\frac{\partial^2 u}{\partial z^2}$ is negligible in comparison to the first partial term $2\overline{k}\frac{\partial u}{\partial z}$, Equation 3.3 is transformed into the standard beam propagation equation:

$$\frac{\partial u}{\partial z} = \frac{j}{2\overline{k}}\left(\frac{\partial^2 u}{\partial x^2} + \frac{\partial^2 u}{\partial y^2} + (k^2 - \overline{k}^2)u)\right) \tag{3.4}$$

In solving this basic type of three-dimensional beam propagation problem, transparent boundary conditions are assumed with no reflections (they would impede steady-state calculations). Transparent boundary conditions provide a better option than the method of inserting artificial absorption regions, where the region's varying α, thickness and shape are all problem-specific and not useful for general case calculations. Furthermore, if the gradient in α over the region is too large, reflections may occur. For more details on these approaches, please consult [24].

Equation 3.4 may also be represented in matrix form as

$$\frac{\partial}{\partial z}\begin{pmatrix} u_x \\ u_y \end{pmatrix} = \frac{j}{2\overline{k}}\begin{pmatrix} P_{xx} & P_{xy} \\ P_{yx} & P_{yy} \end{pmatrix}\begin{pmatrix} u_x \\ u_y \end{pmatrix} \tag{3.5}$$

for differential operators P_{ij}, where P_{xy} and P_{yx} explain cross-coupling effects between the normal fields. The P_{ij} matrix is written as a function of its x- and y-dependent components as follows:

$$\begin{pmatrix} P_{xx} & P_{xy} \\ P_{yx} & P_{yy} \end{pmatrix} = \begin{pmatrix} A_{xx} + A_{yx} & B \\ C & A_{yy} + A_{xy} \end{pmatrix} \tag{3.6}$$

In this form, A_{xx} and A_{xy} represent the x- and y-dependent parts of P_{xx}. The

constants A_{xx} and A_{yy} represent the TE and TM mode propagations and field shapes respectively, while A_{xy} and A_{yx} are related to geometry-induced polarization coupling.

The semi-vectorial form of the BPM equation seen earlier assumes that the diagonal coupled terms, B and C, are negligible. This assumption leads to the following set of equations:

$$\frac{\partial u}{\partial x} = A_{xx}u_x + A_{xy}u_y \tag{3.7}$$

$$\frac{\partial u}{\partial y} = A_{yy}u_y + A_{yx}u_x \tag{3.8}$$

The A_{ij} terms representing propagation constants defined in conjunction with the u_x and u_y slowly varying field terms provide the full expressions for the semi-vectorial equations:

$$A_{xx}u_x = \frac{j}{2\overline{k}}\left(\frac{\partial}{\partial x}\left[\frac{1}{n^2}\frac{\partial}{\partial x}(n^2u_x)\right] + \frac{\partial^2 u_x}{\partial y^2} + (k^2 - \overline{k}^2)u_x\right) \tag{3.9}$$

$$A_{xy}u_y = \frac{j}{2\overline{k}}\left(\frac{\partial}{\partial x}\left[\frac{1}{n^2}\frac{\partial}{\partial y}(n^2u_y)\right] - \frac{\partial^2 u_y}{\partial x \partial y}\right) \tag{3.10}$$

$$A_{yy}u_y = \frac{j}{2\overline{k}}\left(\frac{\partial^2 u_y}{\partial x^2} + \frac{\partial}{\partial y}\left[\frac{1}{n^2}\frac{\partial}{\partial y}(n^2u_y)\right] + (k^2 - \overline{k}^2)u_y\right) \tag{3.11}$$

$$A_{yx}u_x = \frac{j}{2\overline{k}}\left(\frac{\partial}{\partial y}\left[\frac{1}{n^2}\frac{\partial}{\partial x}(n^2u_x)\right] - \frac{\partial^2 u_x}{\partial x \partial y}\right) \tag{3.12}$$

The technique used to solve the semi-vectorial equations is explained for an x-polarized mode propagating in the z direction with the understanding that the same method may be applied to a y-polarized mode. In order to solve the expression for semi-vectorial beam propagation, the form undergoes discretization by the Implicit Crank-Nicholson scheme. The discretization rewrites the problem as a finite difference equation in a mesh with grid points equally spaced along the x axis and for planes equally spaced along the z-axis. At a given grid point i, the slow-varying electric fields are evaluated at a longitudinal midplane situated between plane n for which the field is known, and the following plane $n+1$ in which the field is not known. This method has proven unconditionally stable for all Δz and is accurate to the second order in

Δx, Δy and Δz [25].

The alternating direction implicit method for evaluating semi-vectorial problems separates the propagation along the x and y axes, and involves the addition of a second-order error term [26] to the Crank-Nicholson discretized expressions (the two methods are used in conjunction), transforming Equation 3.7 into

$$\frac{u_i^{n+1} - u_i^n}{\Delta z} = \frac{j}{2\bar{k}} \left(\frac{\delta^2}{\Delta x^2} + [k(x_i, Z_n + \Delta z/2)^2 - \bar{k}^2] \right) \frac{u_i^{n+1} + u_i^n}{2} \tag{3.13}$$

Equation 3.13 evaluates the problem at the midpoint $z = z_n + \Delta z/2$. The second-order difference operator in Equation 3.13 is defined through $\delta^2 u_i = (u_{i+1} + u_{i-1} - 2u_i)$. The equation is rearranged in a tridiagonal manner from which it is easier to isolate the unknown variable u_i^{n+1}:

$$a_i u_{i-1}^{n+1} + b_i u_i^{n+1} + c_i u_{i+1}^{n+1} = d_i \tag{3.14}$$

Please see [27] for details on the coefficients a_i, b_i, c_i, d_i, and the possible boundary conditions with which this equation may be solved. Equations 3.13 and 3.14 are solved with every propagation step, providing the index of refraction at each transverse grid point i. The OptiBPM 5.2 and 6.0 softwares employ the Neumann boundary conditions, which require that normal derivatives of the dependent variable vanish at the boundary.

Just as N number of points are used to discretize the x component of the mode, the y component requires M grid points. With NM unknowns to solve for in the coefficient matrix created by the tridiagonal equations, the number of required operations is on the order of $O(NM)$.

3.1.2 Bending Loss

In designing Y-splitters and waveguide inputs and outputs where bends are employed, bending losses associated with the radius of curvature of a waveguide is an important consideration. The combination of the cylindrical perfectly-matched layer method

(CPML) and a finite-difference scheme imitates an infinite absorbing domain (no reflections). The cylindrical perfectly-matched layer technique also provides a full-vector approach for simulating leaky modes in bending waveguides, which require more efficient boundary conditions than those provided by the transparent boundary conditions method [28]. This section provides an overview of the method used in a Matlab program developed by Milos Popovic employed in calculating bending losses; for more details, please consult [28, 29, 30].

Within the CPML method, only the two-dimensional case is considered as the perfectly-matched layer (PML) model in the z direction is invariant. Based on the separation of the field components, Berenger's original PML formula is not applicable in this case. To derive the wave equation, the PML complex coordinate-stretching approach is used [28]. A change of variables is applied, yielding

$$\widetilde{\zeta} = \int_0^{\zeta} s_\zeta(\zeta')d\zeta' \tag{3.15}$$

where ζ represents ρ, ϕ, and z in the cylindrical coordinate system, and $s_\zeta(\zeta)$ are the complex stretching variables defined as

$$s_\zeta(\zeta) = \begin{cases} 1 & \text{non-PML region} \\ \kappa_\zeta(\zeta) - \frac{j\sigma_\zeta(\zeta)}{\omega\varepsilon_0} & \text{PML region} \end{cases} \tag{3.16}$$

If $\kappa_\zeta(\zeta)$, which absorbs evanescent waves, is set equal to zero, then

$$s_\zeta(\zeta) = \begin{cases} 1 & \text{non-PML region} \\ -\frac{j\sigma_\zeta(\zeta)}{\omega\varepsilon_0} & \text{PML region} \end{cases} \tag{3.17}$$

where

$$\sigma_\zeta(\zeta) = \sigma_{\zeta max}\frac{|\zeta - \zeta_0|^m}{d^m} \tag{3.18}$$

for the PML interface ζ_0, depth d and a typical m of 2 (which provides a parabolic profile).

For the cylindrical coordinate stretching approach of PML in the frequency do-

main, the full vectorial wave equation solved by the program is of the form

$$\widetilde{\nabla}^2\vec{E} + \widetilde{\nabla}(\vec{E}\cdot\widetilde{\nabla}\ln(n^2)) + n^2k_0^2\vec{E} = 0 \tag{3.19}$$

for the operators

$$\widetilde{\nabla} = \tilde{\rho}\frac{\partial}{\partial\tilde{\rho}} + \tilde{\phi}\frac{1}{\tilde{\rho}}\frac{\partial}{\partial\tilde{\phi}} + \tilde{z}\frac{\partial}{\partial\tilde{z}} \tag{3.20}$$

and

$$\widetilde{\nabla}^2 = \frac{1}{\tilde{\rho}}\frac{\partial}{\partial\tilde{\rho}}\left(\tilde{\rho}\frac{\partial}{\partial\tilde{\rho}}\right) + \frac{1}{\tilde{\rho}^2}\frac{\partial^2}{\partial\tilde{\phi}^2} + \frac{\partial^2}{\partial\tilde{z}^2} \tag{3.21}$$

3.2 Modulator Design

The simulation methods and programs described in the previous section aid in calculating the expected performance of the layered structures that support and sufficiently confine only the first-order optical mode. With these tools, heterostructures can be accurately designed with specific layer thicknesses and ordering, and determination of the structure's effective index of refraction and drive voltage required to operate the modulator. The simulations included in this section and the next were executed and contributed by Dr. Gale Petrich of the Integrated Photonic Devices and Materials Group at MIT.

3.2.1 Epitaxial Heterostructures

In that past, modulators have been fabricated on Silicon, Lithium Niobate, Potassium Dihydrogen Phosphate (KDP) and various arsenide and phosphide-based substrates. Though all are viable material options, the operating wavelength and the ultra-broadband requirements of this work make the latter two substrates most attractive to pursue. Consequently, the design, growth and behavior of such materials, known as III- compound semiconductors, is of much interest and warrants a discussion.

Properties of Crystalline Solids

Crystals are distinguished by their distinct atomic arrangement which determines the crystal's bandstructure, optical and electronic behavior. All crystals consist of a lattice composed of a periodically repeating geometric array of points. These form unit cells that fill gaps in the lattice. Single crystals, for example, have an ordered structure in which the atom arrangement within the lattice repeats along all dimensions, while poly-crystalline materials exhibit short-range order only.

The distinct lattice forms are known as Bravais lattices. Each point in the lattice is described by a vector $\vec{r}$ given by

$$\vec{r} = h\vec{a} + k\vec{b} + l\vec{c} \tag{3.22}$$

where basis vectors $\vec{a}$, $\vec{b}$, $\vec{c}$ define the unit cell and h, k and l are integers. The basis vectors also have angles α, β and γ associated with the angles between them; lattice constants a, b, c represent distances between unit cells.

The 14 types of Bravais lattices are categorized into 7 different groups according to their lattice parameters (angles and lattice constants). The group relevant to this work is the cubic lattice group, which covers many of the semiconductor crystals including compound semiconductors. The lattice may be classified as face-centered cubic (FCC), body-centered cubic (BCC) or primitive cubic, and is distinguished by equal lattice parameters, such that $\alpha = \beta = \gamma$ and $a = b = c$.

Many III-V materials, including GaAs and InP, have slightly ionic bonds due to Coulombic interactions. In GaAs, for example, the bonds are expressed by [31]

$$Ga(4s^2 4p^1) + As(4s^2 4p^3) \rightarrow Ga(4s^0 4p^0)^{+3} + As(4s^2 4p^6)^{-3} \tag{3.23}$$

Covalent bonds are also formed between the tetrahedral orbitals in these semiconductors. An atom of the group V elements donates an electron to an atom of the group

III elements, such that in GaAs [31]

$$Ga(4s^2 4p^1) + As(4s^2 4p^3) \rightarrow Ga(4s^1 4p^3)^- + As(4s^1 4p^3)^+ \tag{3.24}$$

The chemical bonds result in ZnS crystallization very similar to a that of a diamond lattice structure. A diamond structure consists of two inter-penetrating FCC sublattices where the elements occupy alternate positions [32]. During growth, deposited materials develop a molecular arrangement that is defined by the underlying substrate, so that materials deposited on the GaAs zincblende-structured wafers used in this work also exhibit a zincblende structure. The specific wafers utilized lack inversion symmetry, and have a top surface corresponding to the $< 100 >$ plane; the wafers may be cleaved along the $< 011 >$ plane where there are is no electrostatic attraction (there is an equal number of group III and group V atoms).

III-V Materials

The modulator's operational frequencies determine the device bandwidth through the following expression:

$$B = f_H - f_L \tag{3.25}$$

For a bandwidth B, and highest and lowest achievable frequencies, f_H and f_L, respectively, the equation suggests that a higher operational frequency implies larger information carrying capacity. The relationship between wave frequency f and wavelength λ is defined as

$$c = f * \lambda \tag{3.26}$$

A larger bandwidth may be acquired through the use of shorter wavelength materials. It is the object of this work to design an ultra broadband modulator that handles signals centered at 800 nm. Consequently, material choices, which would support such a structure by being transparent to light at these wavelengths, are required. Crystals belonging to the III-V group are transparent for short wavelength in the visible and infrared light spectrum ranges, and can be engineered to produce a desired bandgap.

Figure 3-1 [4] displays the various bandgap energies, lattice constants and emission wavelengths of popular and heavily-used III-V binary materials such as GaAs and InP. The dashed lines represent indirect bandgap materials, while the black lines that connect the binary crystals are associated with ternary compounds ($Al_xGa_{1-x}As$ for example) and enclose areas associated with quaternary compounds (for instance, $In_xGa_{1-x}Al_yAs_{1-y}$). These compounds are formed by combining binary materials, and engineered with desired properties in mind, such as operating wavelength and bandstructure. As a result, III-V compound semiconductors are very attractive for use in optoelectronic devices.

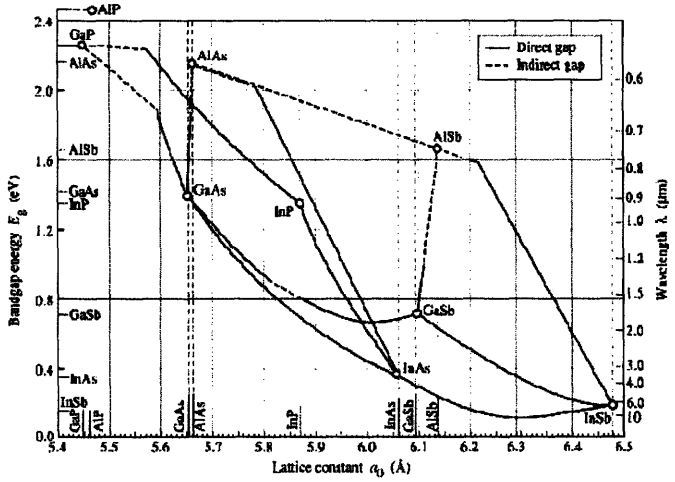

Figure 3-1: Diagram providing the bandgap energy, lattice constant and emission wavelengths of common semiconductor materials in the III-V group [4].

Misfit dislocations arise when a material is deposited on top of another with a different lattice constant, and can lead to a deterioration of the material structurally and electrically. Hence, the growth of heterostructures demands near-perfect lattice matching. GaAs and AlAs, for example, are quite popular in such structures as they have a minimal lattice mismatch and may be combined into ternary compounds with close to ideal lattice matching.

The Matthews-Blakeslee condition provides a method of calculating the thickness limit at which dislocations can form. Epitaxial constraints during growth create elastic strains, dependent upon the film thickness, that may be used to tailor device

performance [33]. The critical layer thickness h_c (derived for a force balance model) at which misfit dislocations begin to form is given by

$$h_c = \frac{b}{2\pi f} \frac{1 - \nu \cos^2 \alpha}{(1 + \nu) \cos \lambda} \left(\ln \frac{h_c}{b} + 1 \right) \tag{3.27}$$

where b is the dislocation strength, ν is the Poisson ratio, α describes the angle between the dislocation line and its Burgers vector, and λ represents the angle between the slip direction and the film plane direction normal to the line of intersection of the slip plane and the layer interface [34]. Therefore, by limiting film thickness, epitaxial growths of lattice mismatched materials can be achieved with minimal strain and resulting dislocations.

Molecular Beam Epitaxy

Thin film deposition and heterostructure formation is achieved by one of three methods: Molecular Beam Epitaxy (MBE), Chemical Vapor Deposition (CVD) and Liquid Phase Epitaxy (LPE). Though all three approaches deserve a discussion of their various capabilities and purposes, the analysis will remain focused on the course pursued in this work - namely, growth by MBE. For more information on this topic, please see the works of Chang [35] and Ryan Williams [5].

In an MBE system, upward-facing effusion cells containing elements from both groups III and V on the periodic table. Individual cells are heated to temperatures in the range of 600°C to 1200°C at which the solid source elements evaporate into atoms or molecules. Ergo, the specific operating temperature of an effusion cell depends upon the material within the cell. The atoms form molecular beams, whose flux is determined by the temperature of the effusion cell, that spread as atoms migrate in the chamber. The molecular fluxes ultimately react with a heated substrate hanging upside-down in the chamber, constructing thin films. The substrate must be heated to a specifically determined temperature at which the incoming adatoms, adsorbed atoms that reside on the surface, can migrate on the substrate to find an energetically favorable site where they may be incorporated into the lattice.

Effusion cells are typically placed in an arrangement that focuses the beams onto the heated substrate and are designed to produce a stable flux, even as sources are depleting over time. The crucibles containing the material being evaporated within an effusion cell can withstand high temperatures for long periods of time, and must be non-reactive in order to ensure material purity and uniformity; for this reason, the crucibles are usually made of pyrolytic boron nitride (PBN). The cells are equipped with shutters that are controlled by a computer that enable shutters to quickly open and close by any amount. The use of shutters provides excellent control over growth thickness and allows accurate transitions between materials. For instance, if an $Al_xGa_{1-x}As$ layer is desired, the shutters of the Al, Ga and As will open, and fluxes of all three vaporized elements will combine by overlapping at the substrate to deposit the layer.

The environment in which the deposition takes place is an Ultra-High-Vacuum (UHV), and is achieved and maintained through austere cleaning and pumping in order to avoid contamination and introduction of impurities into the system under atmospheric conditions. A fresh substrate first enters a load-locked chamber that is pumped down to 10^{-2} Torr by a mechanical pump, and then down to around 10^{-8} Torr by a cryo pump. At this point, the substrate enters a transfer chamber under UHV conditions (at 10^{-10} Torr) and is baked at in a prep-area to dispel moisture. Now the wafer is ready to enter the UHV reactor chamber with a base pressure of 10^{-11} Torr where the wafer is first heated to aid in the desorption of the substrate's native oxide. As this takes place, the effusion cells begin to heat up as well, commencing film growth once all shutters are opened. Within a UHV environment, the mean free path is given by

$$\Lambda = \frac{kT}{\pi D_{atom}^2 P\sqrt{2}} \tag{3.28}$$

and is dependent upon temperature T, atom diameter D, and pressure P. A long mean free path assures that the molecules that make up the incoming beam do not interact with their surroundings or each other, ensuring the material purity of the deposited layer. The MBE system that was used in the growth of the modulator heterostructure

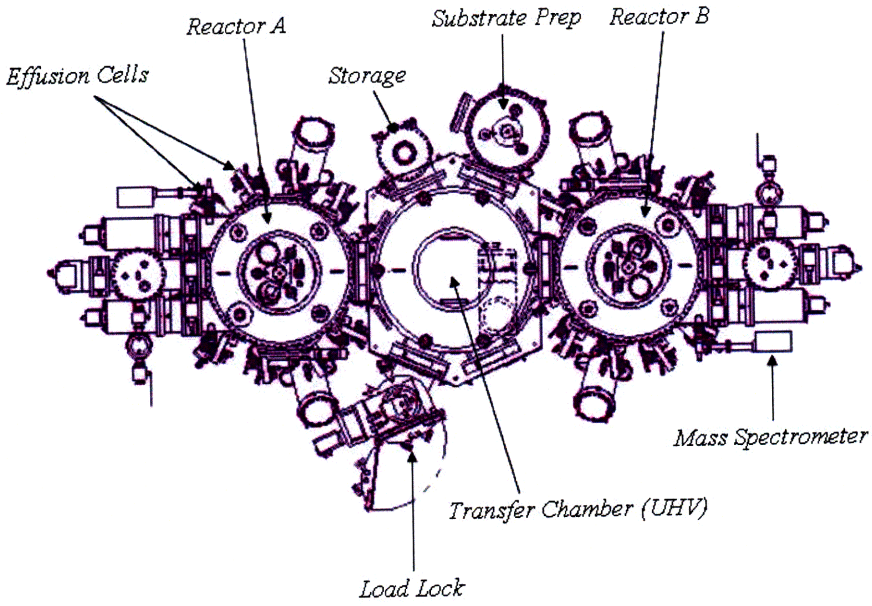

Figure 3-2: Schematic of the Veeco Gen200 dual-reactor MBE system that was used to grow the modulator heterostructure.

is the Veeco Gen200 solid source MBE system shown in Figure 3-2. The sample is monitored during the growth process by measuring sample transparency and following the deposition, when photoluminescence and x-ray measurements of the layers are taken to verify the accuracy of the growth. Crystal layers may also be tracked by reflection high-energy electron diffraction (RHEED) during deposition. In this technique, an electron gun directs a high-energy electron beam at a shallow angle to the sample surface. The crystal structure causes the high-energy electrons to diffract, and a resulting pattern, in the form of streaks, is displayed on a phosphor screen placed opposite to the gun. The pattern formed is significant, as it expresses information regarding growth rates, surface lattice arrangement, uniformity and quality. During depositions, RHEED oscillations are displayed with each period corresponding to monolayer growths, and can be used to calibrate growth rates and fluxes.

3.2.2 Ultra Broadband Modulator Epitaxial Structure

The requirement of broadband modulators centered at an operating wavelength of 800 nm places several restrictions upon the final epitaxial design, seen in Figure 3-3. The GaAs substrate absorbs all wavelengths shorter than 870 nm as shown in Figure 3-1. If the incoming mode couples into the substrate, the light will certainly be absorbed into the substrate and all power will be lost. Therefore, a thick lower cladding layer, transparent to the wavelengths in the desired optical bandwidth, is imperative for mode isolation. Furthermore, the index of refraction of the device active region and surrounding cladding layers should be as similar as possible in order to minimize coupling loss and maximize mode size. This is achieved by constructing the active region of the device as a dilute waveguide. Such a structure involves embedding thin layers of high index material within a material of lower refractive index. The result is an active region with an overall slightly higher effective index (determined by the spacing between high index layers) than that of the cladding layers. The effective index of the structure is close enough to that of the cladding layers so that low coupling loss is maintained, but high enough to keep the mode centered in the active region. The indices and wavelengths associated with the materials employed in the structure are provided in Table 3.1.

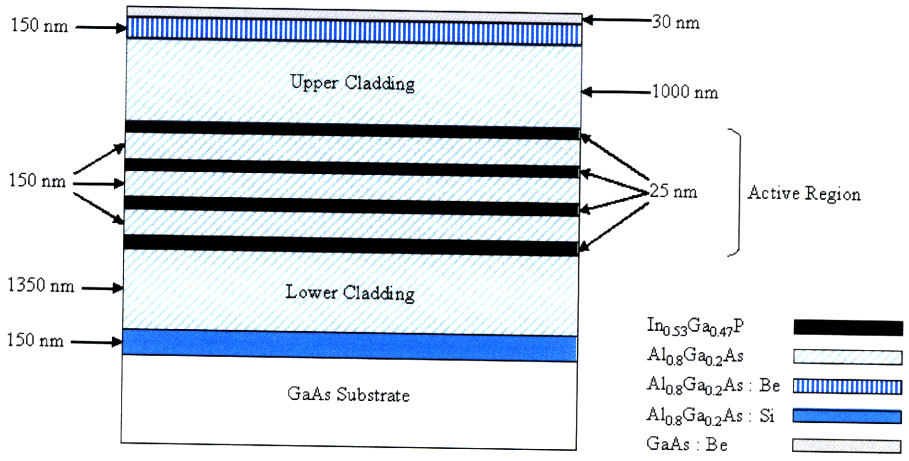

Figure 3-3: Epitaxial heterostructure of the ultra broadband modulators.

Table 3.1: Refractive indices at 800nm of materials composing the arsenide-based modulator heterostructure.

Material	Index at 800nm
GaAs	3.64
$Al_{0.8}Ga_{0.2}As$	3.14
$In_{0.53}Ga_{0.47}P$	3.32

The operational wavelength specification of the modulators also limits the material choices. The layers must be lattice-matched to the GaAs substrate and as mentioned previously, also transparent to the wavelengths in the desired optical bandwidth. High Al content $Al_{0.8}Ga_{0.2}As$ and $In_{0.53}Ga_{0.47}P$ follow these restrictions, and are hence chosen as the low and high index materials respectively. Although the use of AlGaAs as a cladding material minimizes the issue of lattice-matching, the high Al content presents a growth difficulty due to the low Al adatom mobility on the surface during deposition. Grown epitaxial heterostructures have shown weak photoluminescence (PL) emission at 650 nm due to the $In_{0.53}Ga_{0.47}P$ layers, as the $Al_{0.8}Ga_{0.2}As$ is an indirect bandgap material and therefore, does not emit. Thus, this structure has a very large optical bandwidth ranging from 650nm and onward.

The epitaxial structure is designed in a P-I-N configuration, with an N^+, 10^{18} silicon-doped substrate and beryllium-doped top contacts. The doping level of the p-doped GaAs and $Al_{0.8}Ga_{0.2}As$ layers is on the order of 10^{17}. The doped contact layers are essential, as a higher carrier concentration leads to reduced contact resistance, and consequently aid in making good ohmic contact to the metal that is to be evaporated on top of the heterostructure. However, these layers must also be sufficiently isolated by cladding layers from the undoped active region, which would suffer from losses due to free carriers. Additionally, the P-I-N structure may operate under reverse bias, eliminating the concern of carrier injection and optical loss associated with absorption that can occur under forward bias.

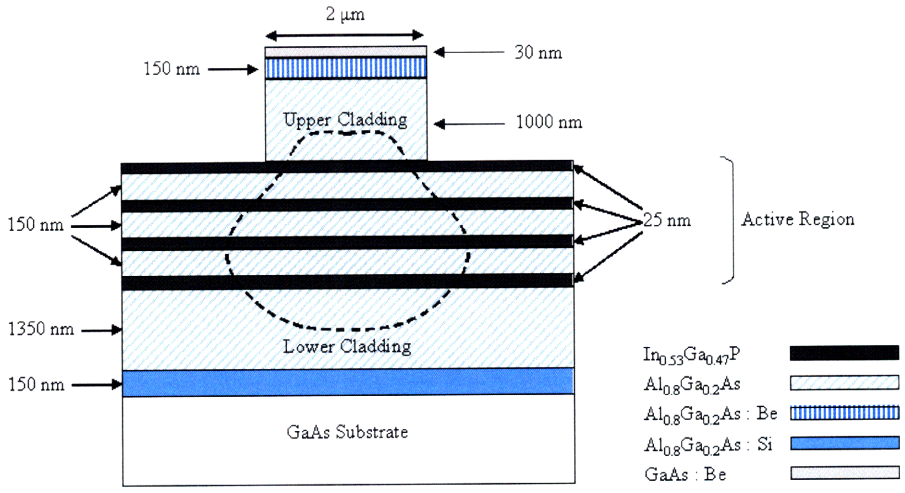

Figure 3-4: Epitaxial heterostructure of the shallow etched, 2 μm ridge waveguide. The dashed figure represents the location of the propagating TE mode within the structure.

Shallow-Etched Arsenide-Based Structure

The first arsenide-based structure, shown in Figure 3-4, that can be fabricated using the epitaxial heterostructure previously discussed is a shallow-etched device. In this structure, a 2 μm wide ridge waveguide is created by etching through the top doped GaAs and $Al_{0.8}Ga_{0.2}As$ layers as well as the thick upper cladding layer. The top doped contact layers must be etched away completely around the ridge to prevent the electrical shorting of all devices on the wafer (due to electrical connectivity). A ridge of maximal width is desired in order to avoid loss by minimizing the interaction of the mode with the etched sidewalls. However, a ridge too wide will introduce unwanted higher modes. Based upon OptiBPM 5.2 simulations, the 2μm ridge was chosen as the largest width that solely supports first-order modes.

Figure 3-5 presents the simulated TE and TM mode profiles and associated indices for the shallow-etched structure. The differing mode indices correspond to a natural birefringence of $n_{TE} - n_{TM} = 1.9 \cdot 10^{-3}$ at 800 nm. However, as the device only deals with modulation of the TE component, the birefringence is irrelevant to its operation. Both modes are approximately 3 μm x 2.5 μm (WxH) due to the lateral confinement from the shallow-etched ridge and positioning of the high-index layers.

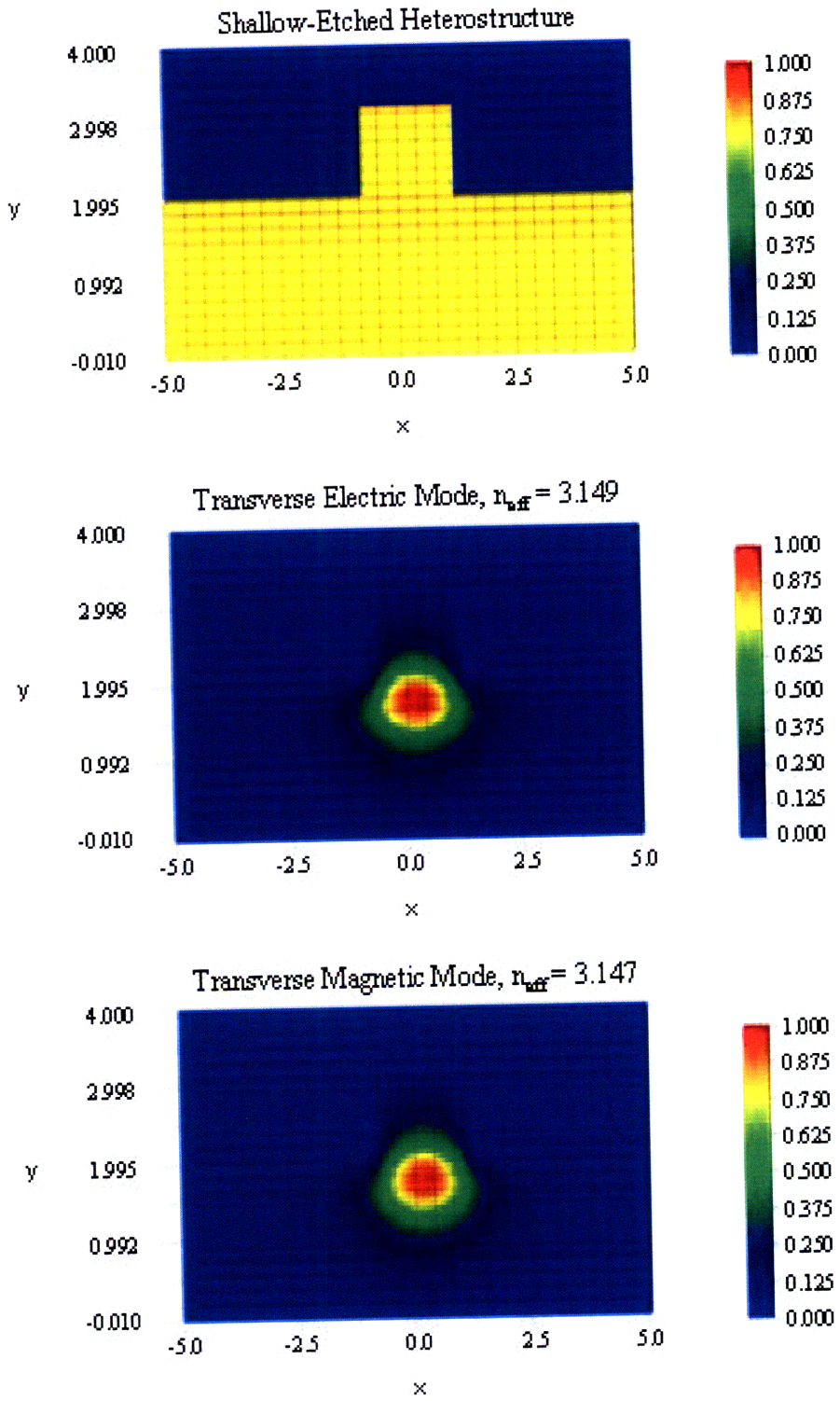

Figure 3-5: Mode simulations for the shallow-etched ridge waveguides using OptiBPM 5.2. The simulated epitaxial structure is shown (top) as well as the computed TE mode profile (center) and TM mode profile (bottom). Calculated indices associated with the profiles are also included.

Due to the shallow-etched ridge waveguide, the optical mode is not strongly confined laterally in the structure, as indicated in Figure 3-4, which can lead to loss as the mode propagates around bends.

Deep-Etched Arsenide-Based Structure

To better confine the optical mode within a waveguide with bends, a deep-etched device based upon the same epitaxial heterostructure was developed. The 2 μm ridge

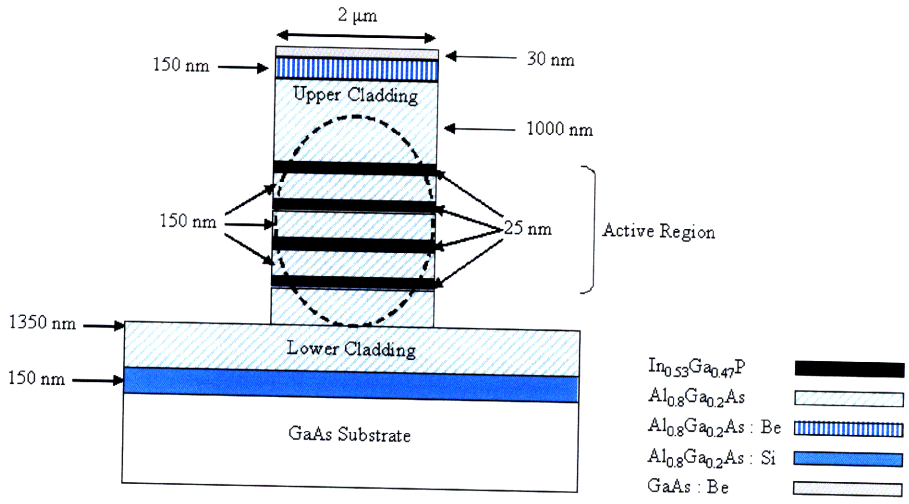

Figure 3-6: Epitaxial heterostructure of the deep-etched, 2 μm ridge waveguide. The dashed figure represents the location of the propagating TE mode within the structure.

now extends part-way down into the lower cladding layer, thereby restricting the mode laterally as well as vertically. Lateral movement within the active region is thus minimized, as is apparent in the device schematic shown in Figure 3-6. The simulated mode profiles are provided in Figure 3-7. The modes are approximately 1.8 μm x 2.4 μm (WxH), almost half as wide as the modes of the shallow-etched structure and nearly as tall, exhibiting the improved confinement that is desired. As a result of etching through all four high-index layers, the lateral index contrast is increased, reducing the need for the gradual bends that were required for the shallow-etched device. The etching chemistry used to develop this structure may differ from that employed with the shallow-etched device due to the combination of $Al_{0.8}Ga_{0.2}As$ and

$In_{0.53}Ga_{0.47}P$ layers that must now be removed sequentially.

The natural birefringence in this structure is estimated to be $1.4 \cdot 10^{-3}$ at 800 nm, roughly identical to that of the shallow-etched heterostructure. The numbers are similar as the epitaxial structures are identical, but the differences arising from fabrication do cause slight changes in the effective index of refraction.

3.2.3 Voltage Requirement of the Heterostructures

Calculation of the required applied electric field, or equivalently, the applied voltage that can achieve a particular phase and amplitude modulation verifies design quality and provides an estimate of the operational specifications of the device. The equations that compute Δn, $\Delta\phi$, $V_{\frac{\pi}{2}}$ and V_π were derived in subsection 2.2.4 for bulk semiconductors, but are not directly applicable to heterostructures. Appendix A contains a full analysis of the electro-optic effect in heterostructures, and the equations found there are used to calculate pertinent design parameters.

The TE mode of a waveguide oriented along the $< 011 >$ direction will experience a phase shift due to E_y given by

$$\Delta\phi_{x'} = \frac{2\pi}{\lambda}\frac{Ln^3 E_y(r_{52} + r_{12} + r_{32})}{2} \tag{3.29}$$

If a phase shift of $\frac{\pi}{2}$ or π is desired, the voltage required is described by

$$V_{\frac{\pi}{2}} = \frac{\lambda}{2}\frac{t_g}{Ln^3[r_{52} + r_{12} + r_{32}]} \tag{3.30}$$

and

$$V_\pi = \lambda\frac{t_g}{Ln^3[r_{52} + r_{12} + r_{32}]} \tag{3.31}$$

respectively, where n is the heterostructure's overall index of refraction, L is the modulator length (varying from 3 to 10.5 mm), λ is the operational wavelength (800 nm in this work) and t_g is the height or thickness of the active region of the modulator (taken as the mode height - 2.5 μm for the shallow-etched device, 2.4 μm for the deep-etched device).

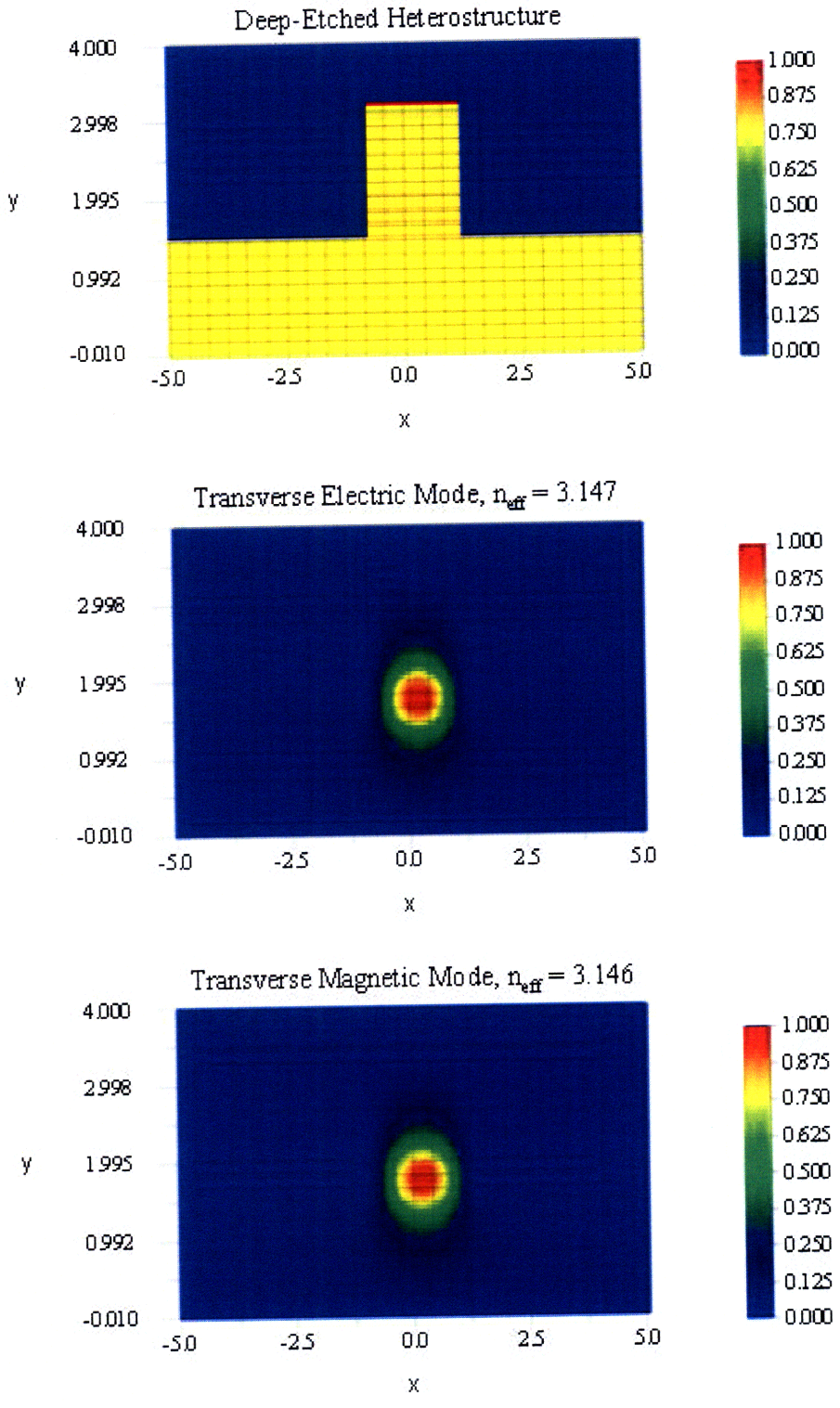

Figure 3-7: Mode simulations for the deep-etched ridge waveguides using OptiBPM 5.2. The simulated epitaxial structure is shown (top) as well as the computed TE mode profile (center) and TM mode profile (bottom) with associated indices.

During computation, several assumptions are made. First of all, the electro-optic coefficients r_{12} and r_{32} are not known as they are equal to zero in bulk semiconductors of group $\bar{4}3$ (see the electro-optic coefficient matrix in 2.2.4). For the purpose of this calculation, r_{12} and r_{32} are assumed to be similar to the value of r_{52}. Secondly, r_{52} is taken to be approximately equal to values of the more well-known r_{41} (in bulk semiconductors, $r_{41} = r_{52} = r_{63}$). Furthermore, the values of r_{41} for the materials used, namely $Al_{0.8}Ga_{0.2}As$ and $In_{0.53}Ga_{0.47}P$, are unknown at 800nm, and are also unknown at other wavelengths for these specific Al and In concentrations. As a result, the values of r_{12}, r_{32} and r_{52} used in the calculations are estimates based upon values of r_{41} of similar materials at certain wavelengths found in literature. Finally, the values of r_{12}, r_{32} and r_{52} are given for the heterostructure, not just a single layer. Therefore, the contribution from the far thicker $Al_{0.8}Ga_{0.2}As$ layers is much higher than that of the thin $In_{0.53}Ga_{0.47}P$ layers, and is reflected in the chosen electro-optic coefficients.

The calculated values of V_π for both the shallow and deep-etched devices are given in Table 3.2 (values of $V_{\frac{\pi}{2}}$ are half the value of V_π). The values are computed for all devices lengths, and for the distinct case of $r_{12} = r_{32} = r_{52} = 1.0 \cdot 10^{-12}$ m/V (Table 3.2). Additional voltage calculations based upon other electro-optic coefficient possibilities are available in Appendix A: $r_{12} = r_{32} = r_{52} = 1.4 \cdot 10^{-12}$ m/V (Table A.1), $r_{12} = r_{32} = r_{52} = 0.7 \cdot 10^{-12}$ m/V (Table A.2) and finally, the case of behavior of bulk semiconductor modulators, $r_{12} = r_{32} = 0$ m/V and $r_{52} = 1.0 \cdot 10^{-12}$ m/V (Table A.3). These values were chosen based upon literature findings, and are meant to convey the degree of sensitivity of the calculation with regard to changing the electro-optic coefficient values.

The results presented in Table 3.2 suggest that a longer device requires less voltage to achieve the same phase shift. Overall, the voltage requirement expected of the devices for a π phase shift is between $2 - 20$V depending upon device length and heterostructure electro-optic coefficients. These numbers are on par with values found in literature [36].

Table 3.2: Calculated values of V_π for both shallow and deep-etched devices of various lengths oriented in the $< 011 >$ direction. This calculation assumes $r_{12} = r_{32} = r_{52} = 1.0 \cdot 10^{-12}$ m/V.

Device Length (mm)	3.0	4.5	6.0	7.5	9.0	10.5
Shallow Device Voltage (V)	7.11	4.74	3.56	2.85	2.37	2.03
Deep Device Voltage (V)	6.84	4.56	3.42	2.74	2.28	1.96

3.3 Mask Set Design

The final step in the design of the ultra broadband modulators requires the creation of the masks that are to be used in the photolithography steps of the fabrication process. Mode calculations, propagation simulations, material, optical and electrical characteristics are all essential in developing a mask set. All tools and structural considerations described thus far have been used in the conception and realization of an etch-depth-independent, image-reversal mask set. The first mask of the four-layer set defines the 2 μm ridge waveguides, while the second layer creates passive waveguides of the same width, the 26 μm trenches that surround all waveguides and power splitters in order to minimize material etching. The trenches provide an alternative option to etching the whole surface of the wafer, which would reduces anisotropy and increases micromasking during the process. The third mask creates openings called vias that aid in the placement of metal contact pads using the fourth mask. The eight dies on the mask account for every combination of crystal orientation, power splitting method and straight or angled input/output waveguides.

The modulator devices, displayed in the mask layout in Figure 3-8, are designed as passive waveguides, shown in green, that lead to power splitters - multimode interferometers (MMIs) or Y-splitters, shown in dark blue next to the red metal contact pads. The power splitters divide the incoming signal power evenly across the two powered arms of a Mach Zehnder interferometer, over which the contact pads are evaporated. The signal is then recombined using an inverted power splitter and is transferred by another passive waveguide to the output. A closer view of two of the eight device dies on the mask is provided in Figure 3-9. The modulators vary

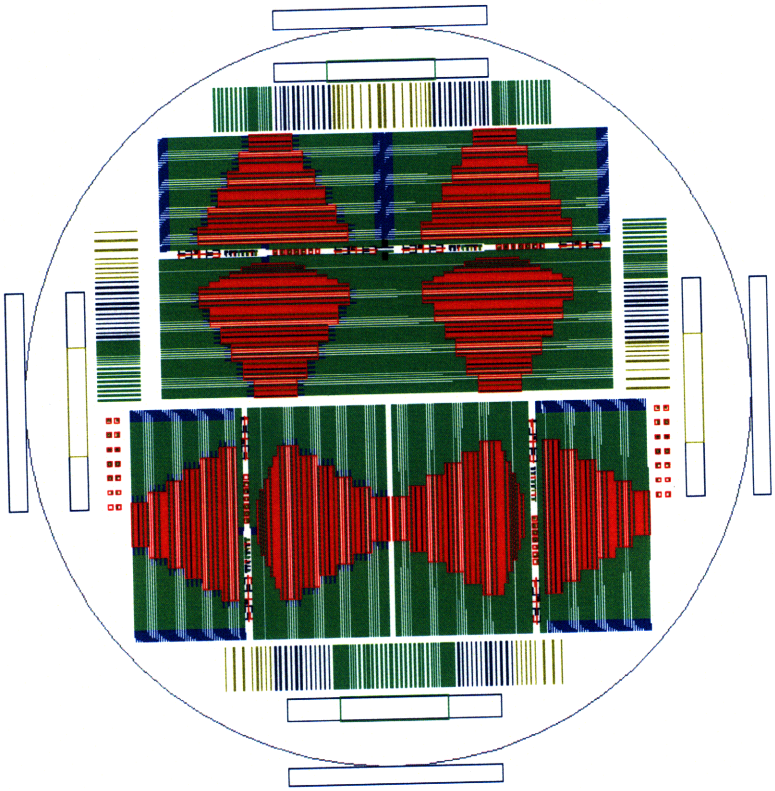

Figure 3-8: Four-layer mask set used in the fabrication of shallow and deep-etched ultra broadband modulators.

in length from 3mm to 10.5mm, as the structure's effective index of refraction is not precisely known. The lengths were determined based upon assumed values of r_{41} for $Al_{0.8}Ga_{0.2}As$ and $In_{0.53}Ga_{0.47}P$, which are unknown at 800nm.

3.3.1 Device and Crystal Orientation

Modulator performance is highly dependent upon orientation relative to the crystal structure. In the discussion of the electro-optic effect in Subsection 2.2.4 and Appendix A, a change in the modulator coordinate system is addressed. An electric field applied in the y direction along the $< 001 >$ growth plane will result in a change in the index of refraction in the x' and z' axes oriented 45° from the x and z axes. Efficient modulators are therefore oriented at a 45° offset from the top surface $< 100 >$ direction, and are oriented along the $< 011 >$ and $< 01\bar{1} >$ cleave directions as seen

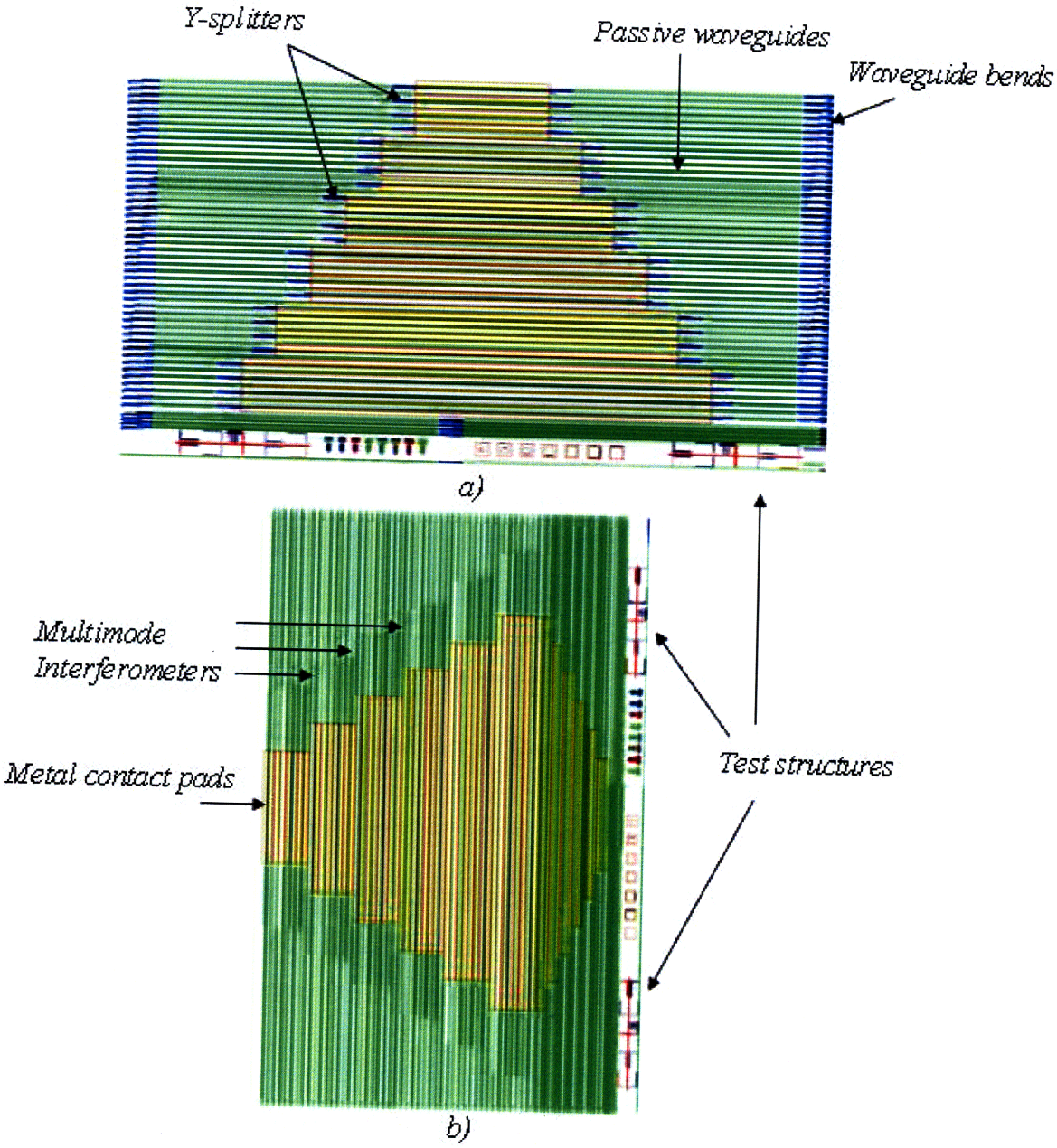

Figure 3-9: Sample dies from the mask set displaying various features of the mask. Passive waveguides, shown in green, lead to powered Mach Zehnder interferometer arms covered by metal contact pads (visible in red). a) Die with $< 011 >$ oriented waveguides equipped with bends in the input and output waveguides (defined in blue on edges of the die). Power division and recombination is achieved by Y-splitters (denoted in blue next to the red contact pads). b) Die with $< 01\bar{1} >$ oriented waveguides with straight input and output waveguides. Multimode interferometers (MMIs) are used to split and recombine incoming power. Both dies have test structures to aid in fabrication.

in Figure 3-9.

In order to isolate the heterostructure's electro-optic coefficient r_{52}, corresponding to the $x'z'$ plane, both $n_{x'}$ and $n_{z'}$ defined in Appendix A must be experimentally extracted. For a waveguide oriented in the z axis, the TE mode will experience a phase shift due to $n_{x'}$. To obtain the TE phase shift due to $n_{z'}$, the waveguide must be oriented in the x direction. For this reason, the mask contains both waveguide orientations which will allow the measurement of both $\Delta\phi_{x'}$ and $\Delta\phi_{z'}$ from each waveguide orientation, and enable the derivation of r_{52}.

3.3.2 Power Splitters

Signal modulation using an MZI is carried out by applying an electric field across one arm of the MZI, and introducing a phase shift relative to the second arm. Without electric field applied, the arms are identical and the signal power carried in each arm is equal. The power of an incoming optical beam is divided using either a multimode interferometer or a Y-splitter, and simulations of both types of power splitters were carried out using the beam propagation method to determine their ideal physical design and performance. Though both the multimode interferometer and the y-splitter execute the same task, their methods are quite different and have distinct design advantages and disadvantages.

Multimode Interferometers (MMIs)

A multimode interferometer, or MMI, operates based on self-imaging to successfully split and combine waveguides. Within its wide cavity, multiple modes are excited by an incoming light beam and interfere constructively or destructively. These interferences form images of maxima and minima at nodes that correspond to cavity lengths, and can result in couplers, splitters or combiners [37]. Consequently, these devices are highly dependent upon physical dimensions to achieve the desired interference, and are, therefore, wavelength dependent.

MMIs are generally said to be of an NxM form, with N inputs and M outputs. In

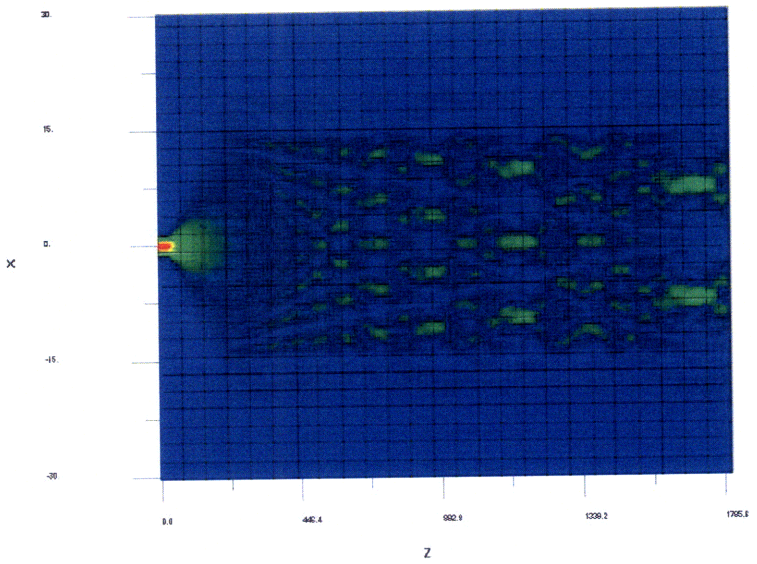

Figure 3-10: BPM simulation of the 28μm wide, 1.75mm long 1x2 multimode interferometer adopted in the modulator mask set. The number of outputs are determined by the cavity length of the MMI.

this work, 1x2 and 2x1 MMIs are adopted as passive waveguide splitters and combiners respectively, and are used in conjunction with MZIs. As MMIs involve no bends, and thus no loss due to bending, their physical size depends upon the distance between the two MZI arms. A 14 μm distance between the centers of both powered arms facilitates fabrication while maintaining a reasonable MMI length. Beam propagation simulations at 800 nm using OptiBPM 6.0 were used to determine the optimal structure of the MMIs. Figure 3-10 displays the simulation results of the 3dB, 1.75 mm long and 28 μm wide 1x2 MMIs integrated into the mask set.

Y-Splitters

The other type of power splitter included on the mask is a wavelength independent Y-splitter. Figure 3-11 shows a simulation result of a Y-splitter using Optiwave 6.0. As the splitting ratio relies on device symmetry, a 3dB ratio is achieved simply by designing symmetric branches. Y-splitters, unlike MMIs, use bends to split and recombine optical signals, and for that reason, involve a degree of bending loss. In

designing the Y-splitters, a Matlab program developed by Milos Popovic (see Section 3.1.2) was employed in computing bending radii that would result in minimal loss during power splitting in the shallow-etched structure (which has weak confinement capability). Though a 250 μm radius was calculated to be sufficient, a 8.93 mm radius of curvature was ultimately used to produce an extremely gradual bend. Given this radius and the set distance between the modulator arms, the length of the Y-splitters was determined to be 500 μm.

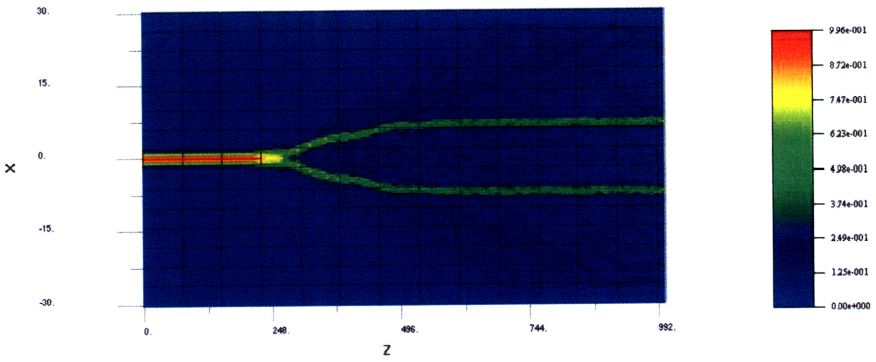

Figure 3-11: BPM simulations of a 500μm Y-splitter with an 8.93mm radius of curvature. The device exhibits even splitting and low loss due to bending in simulations.

3.3.3 Inputs and Outputs

Two varieties of inputs and outputs were pursued in the mask design - straight and angled. The straight passive input and output waveguides are shown in Figure 3-8 as part of the green passive waveguides. These basic input/output waveguides are affected by facet reflections, but enable easier coupling. Alternately, input/output waveguides angled off of the $< 011 >$ and $< 01\bar{1} >$ directions, shown in dark blue on the mask set, were also designed. Though coupling may be more difficult due to the angle, the slant prevents the light that reflects off of cleaved facets from coupling into the passive waveguide [38]. Due to the concern of bending loss, the same radius of curvature applied to the Y-splitters was employed in the curved input and output waveguides.

3.3.4 Test Structures

The final patterns on the mask set are test structures used in the optimization of the fabrication process. The test structures include straight waveguides of varying widths and squares that aid in determining the success of a photolithography or etch step without damaging the actual devices. These test structures allow real-time assessment of resist exposure and development, etch depths and profiles, etc. Additionally, comb-like designs and crosses as seen in Figure 3-12 are employed in the alignment of power splitters and passive waveguides to the powered Mach Zehnder

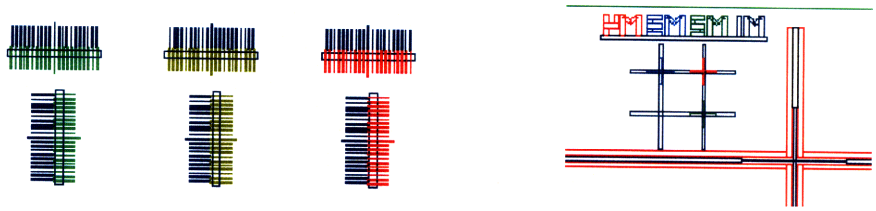

Figure 3-12: Structures included in the mask set to aid in alignment of the passive waveguides and power splitters with the Mach Zehnder arms. The different colors of the comb-like patterns (left) and the crosses (right) correspond to distinct mask layers.

modulator arms. The cross structure allows simple evaluation of the alignment in the x, y and θ orientations. Smaller crosses corresponding to different mask layers are positioned within a larger cross that is defined in the first photolithography step. The alignment marks are especially valuable as placement of the passive waveguides in relation to the Mach Zehnder arms must be extremely accurate to ensure minimal power loss as the optical mode propagates through the structures.

Chapter 4

Experimental Methodology

Device fabrication requires the design of an efficient process flow and the optimization of each and every step in coordination with previous and consequent processing conditions. Critical alignments over distances on the order of millimeters (which control coupling loss between passive and active waveguides), uneven surface topology as a result of entrenched ridges and concern of sidewall roughness place further restrictions upon fabrication and necessitate the development of accommodating approaches.

4.1 Process Flow

The fabrication process commences with the cornerstone of microtechnology - photolithography. The wafer (Figure 4-1a) is first thoroughly rinsed by acetone, methanol, and isopropanol to remove organic residue, microparticles and debris. When the surface is clean, the wafer is coated with AZ5214 photoresist, a light-sensitive material, using a spin coater. Solvents in the resist are removed via an oven bake, and then the coated wafer is brought into contact with the first of four patterned masks by the Electronic Visions 620 aligner. The wafer is briefly exposed to UV light (areas shielded by mask patterns do not receive light) and transferred to a hotplate for a reversal bake to crosslink the exposed areas. After a 60 second flood exposure and development in AZ422 to remove the initially exposed areas of resist, a pattern in the resist layer equivalent to an inverted mask image emerges (Figure 4-1b). The

lithography technique is known as image reversal photolithography, and is described in great detail in Section 4.1.1. To smooth photoresist sidewalls, the wafer is etched in a He/O_2 plasma (5/10 sccm, 20 mTorr, 150 Watt) for 10 seconds prior to subsequent processing.

The modulator Mach Zehnder arms are defined by a 100 nm thick layer of nickel evaporated on top of the resist pattern (Figure 4-1c). The metal layer protects the underlying semiconductor layers in subsequent processing steps, and shields the doped semiconductor surface, critical for good metal contacts, from the damaging effects of ion bombardment during reactive ion etches. After evaporation, the resist and metal in the outlying areas are removed by a lift off process (Figure 4-1d) using either acetone or heated N-Methylpyrrolidone. The exposed semiconductor surface is etched in a reactive ion etcher (Figure 4-1e) using BCl_3 plasma (13 sccm, 5 mTorr, 392 Volts). The first of two III-V etches removes the doped GaAs and $Al_{0.8}Ga_{0.2}As$ and prevents the MZIs from being interconnected.

In preparation for the next semiconductor etch, a 250 nm film of SiO_x is deposited (Figure 4-1f) by PECVD, or plasma-enhanced chemical vapor deposition. Unlike evaporation, which is directional, PECVD is conformal and successfully covers all forms of topography (sidewalls, trenches, etc). Prior to resist coating, HMDS is applied to the wafer surface to promote adhesion between the resist and oxide. Following photoresist spinning and baking, the wafer is patterned by image reversal lithography using the second mask (Figure 4-2g). The second photolithography step is particularly difficult, requiring feature alignment with a large aspect ratio (2 μm wide passive and active waveguides aligned over mm distances); accuracy is essential in preventing power loss between passive and active areas. After a short ash step consisting of a He/O_2 reactive ion etch (RIE) to smooth the resist sidewalls, the resist pattern is transferred to the deposited SiO_x film using a CF_4 (15 sccm, 15 mTorr, 50 Volts) RIE process developed by Ryan Williams, a former member of the Integrated Photonic Devices and Materials Group at MIT [5]. With an etch rate of 30 nm/min, the underlying $Al_{0.8}Ga_{0.2}As$ layer is exposed at the surface after 9 minutes (Figure 4-2h).

The second BCl_3 reactive ion etch establishes the ridge height and mode confinement (depending upon the number of $In_{0.53}Ga_{0.47}P$ layers are removed) and defines the power splitters and passive waveguides (Figure 4-2i). If no high index layers are etched and only the upper cladding layer is affected, the device is referred to as a shallow-etched structure. If the entire stack is etched, the modulator will be referred to as a deep-etched structure. The patterned SiO_x layer serves as a hard mask and protects the passive waveguides, power splitters and areas between trenches while the powered Mach Zehnder arms remain protected under the evaporated nickel. SiO_x etches at a rate of 4 nm/min in BCl_3, so the 250 nm thick SiO_x layer is more than sufficient for a 20 minute etch.

Evaporation of top-side metal contacts requires a flat surface. A spin-on dielectric and insulator, Benzocyclobutene (BCB) coats the sample, filling in the trenches and burying the ridges to create a uniform topography (Figure 4-2j). The BCB is etched back to expose the nickel-covered Mach Zehnder arms (Figure 4-2k) to which the top-side metal must make contact. The third mask may be used to protect areas during the etchback, but etching without a photoresist mask is also possible.

A third image reversal step, using the fourth and final mask, patterns a pre-baked resist layer on the wafer (Figure 4-3l). Ti/Pt/Au films (300 Å, 200 Å, 2000 Å) are sequentially evaporated onto the sample and define large contact pads that power the modulators and form ohmic p-type contacts. Following metal deposition, resist and excess metal are again lifted off using a solvent (Figures 4-3m,n), completing the top-side processing. The back-end processing involves a wafer lapping procedure developed by Sheila Nabanja of the Integrated Photonic Devices and Materials Group. Lapping the wafer thins the substrate from a thickness of 350 μm to approximately 175 μm, improving the final cleave. During lapping and subsequent backside metal evaporation, the top surface is protected by a resist layer (Figure 4-3o) to minimize damage to fabricated devices. The top and backside metal - [n-type Ni/Au/Ge/Au (300 Å, 600 Å, 300 Å, 2000 Å)] - are annealed at a temperature no higher than 400°C. Between 400°C and 475°C, the BCB undergoes molecular changes and begins to contract [39], creating breaks in the planarization and top-side metal. Though

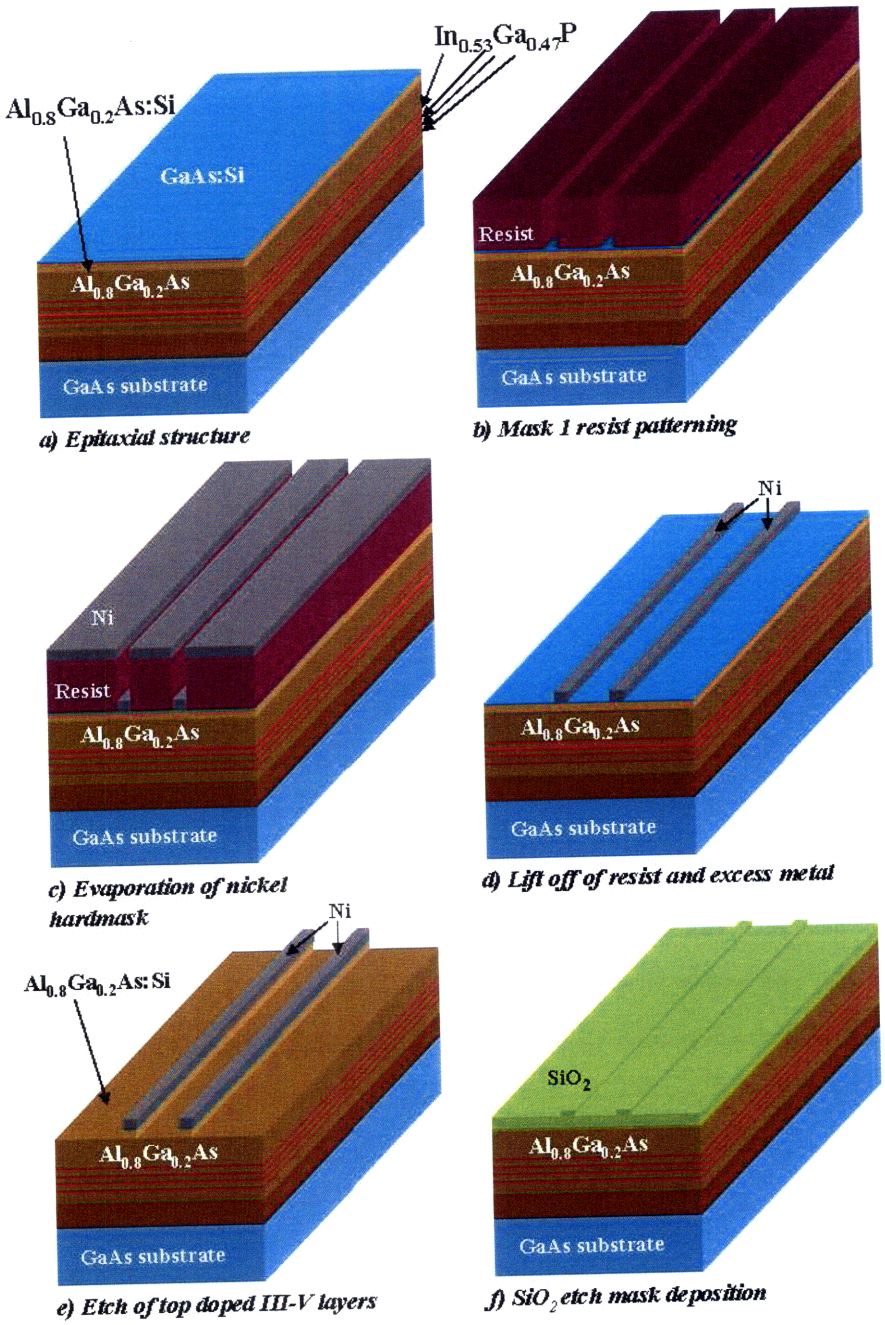

Figure 4-1: Process flow of the ultra broadband modulators. The epitaxial wafer (a) is coated with photoresist which is in turn patterned by image reversal photolithography (b). A 100nm nickel hard mask layer is evaporated (c) onto the wafer surface and lifted off (d). The nickel defines the Mach Zehnder modulator arms and protects the metal contact-semiconductor interface during the III-V material etch of the doped semiconductor layers (e). Following the BCl_3 etch, an oxide layer is deposited by PECVD (f).

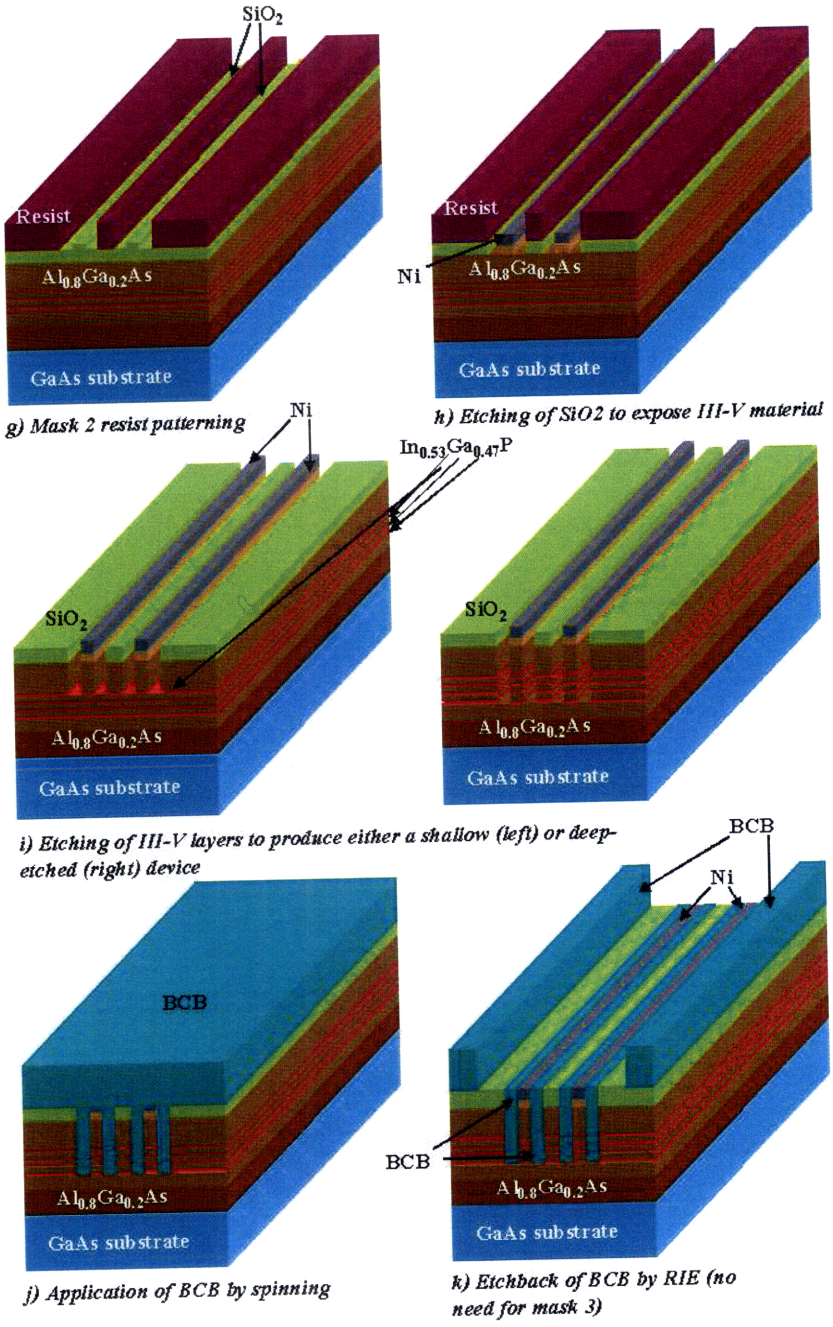

Figure 4-2: Process flow of the ultra broadband modulators (continued). Photoresist is spun onto the wafer and patterned by image reversal photoresist to define passive devices (g). The resist pattern is transferred to the SiO_2 layer through a CF_4 RIE step (h) to expose the semiconductor surface. A second BCl_3 etch is carried out to produce a shallow-etched or deep-etched device (i). Following the RIE, BCB planarizes the sample surface (j) and is etched back to expose the nickel-covered Mach Zehnder arms (k).

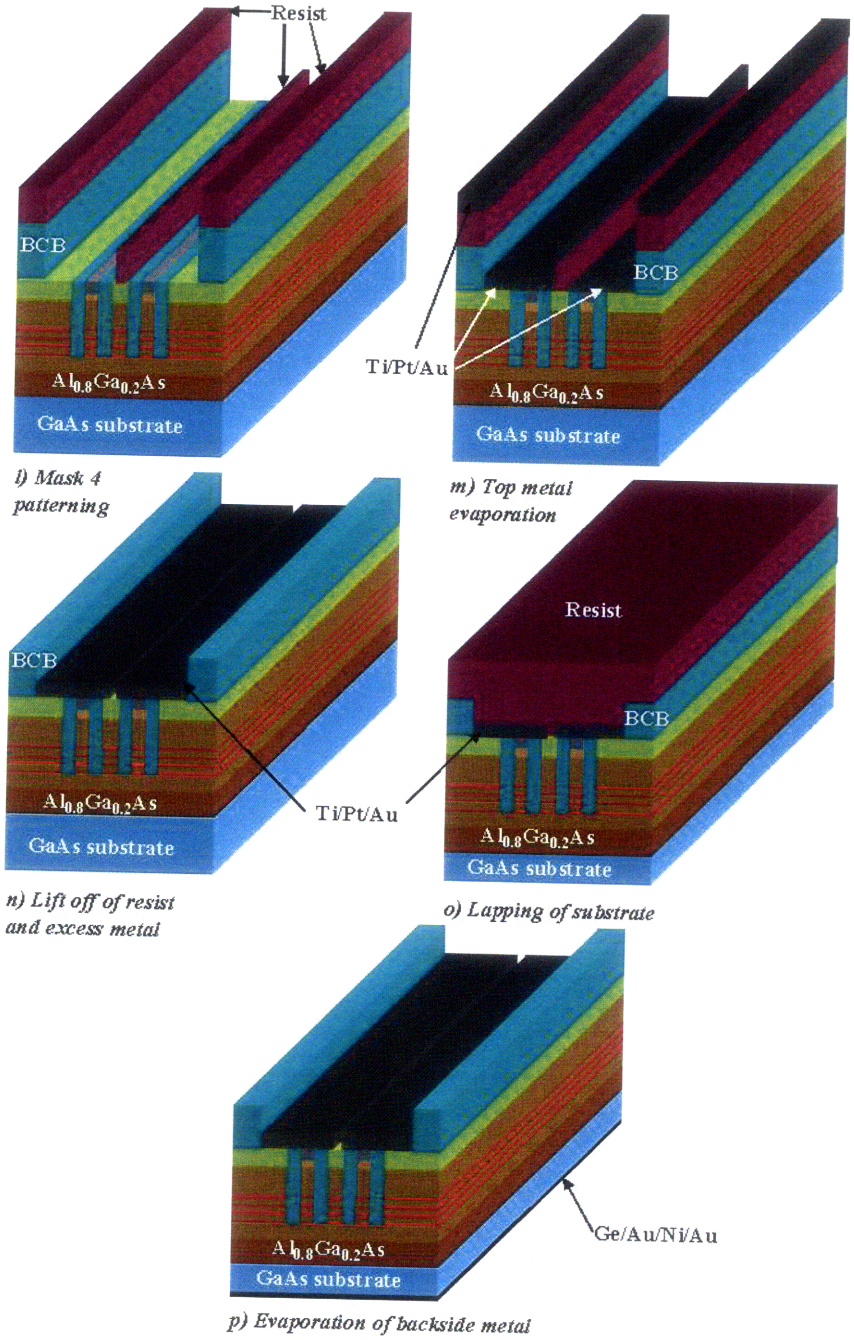

Figure 4-3: Process flow of the ultra broadband modulators (continued). A photoresist layer undergoes image reversal using the fourth mask to prepare for top contacts (l). The metal, Ti/Pt/Au, is evaporated (m) by electron beam evaporation and lifted off (n). The wafer surface is protected by a resist layer during lapping (o) and evaporation of backside metal, Ge/Au/Ni/Au (p-type). Both bottom and top metal contacts are annealed at a temperature lower than 400°.

higher temperature anneals reduce contact resistance, the advantage is outweighed by the deterioration of the BCB. The final device is presented in Figure 4-3p. For all details and parameters of the process, please consult Appendix B.

4.1.1 Image Reversal Photolithography

Photolithography, as explained in the previous section, patterns a layer of photosensitive photoresist. There are two types of lithography - positive and negative. Positive photolithography uses positive resist, in which exposed areas develop away following a bake and short exposure in ultraviolet light. Negative photolithography, or image reversal depending upon the photoresist used, transfers the negative image of the mask. The mask itself is made of quartz and has chrome-coated patterns that are transfered by photolithography to the resist and ultimately the structure. Hence, the mask design determines whether positive or image reversal photolithography is pursued; only image reversal using the AZ5214 photoresist is used with the ultra broadband modulator mask set.

The process flow of the image reversal procedure is illustrated in Figure 4-4. Initially, AZ5214 resist coats the substrate. The resist thickness is dependent upon the spin speed and the specific formulation of the resist. A desired 1.4 μm thick layer is obtained at a spin speed of 4k rpm and a duration of 30 sec. The wafer is then baked in an oven for approximately 35 minutes at 95°C. The objective of the pre-bake is to sufficiently drive out solvent in the resist as well as prevent adhesion to the mask during exposure, which could result in unbalanced contact with the mask and the breaking of the wafer. As a result, the baking temperature, time and uniformity are not critical and a convection oven may be used.

After the pre-bake, pattern transfer from the mask to the photoresist is accomplished by exposure to ultraviolet light. The wafer and mask are brought into contact by an aligner, and a shutter opens to expose the resist. Regions of photoresist that are covered by chrome-coated areas of the mask are shielded and receive no light, but

areas beneath the uncovered quartz are exposed to a light dosage given by

$$Dosage = I \cdot t \tag{4.1}$$

where I is the exposure intensity in units of mW/cm^2 and t is the exposure time. The dosage is constant for the process, and any change in bulb intensity may be accounted for by extending or decreasing the exposure time. The first exposure defines the resist profile; therefore, determining and maintaining accurate dosage with good uniformity across the wafer is very important. An exposure that is too short will fail to activate the photoactive compound (PAC) throughout the full depth of the resist layer and will result in undercutting of the profile. A long exposure, on the other hand, will activate the PAC even in shielded areas, rendering them insoluble as well. The dosage decided upon through experimentation is 13.95 mJ/cm^2, with the intensity varying between 9.0-9.5 mW/cm^2 and exposure lengths of approximately 1.4-1.6 seconds.

The post-bake of the resist is often referred to as the image reversal bake. Exposed areas with active PAC become thermally cross-linked at sufficiently high temperatures, transforming them into insoluble and light-insensitive materials after another long exposure to UV light. The bake temperature, usually between 90°C and 130°C, is especially critical and distinct to the heating element employed - in this case, a hotplate. Unlike a convection oven, a hotplate bakes the resist from the bottom up, effectively and thoroughly dispelling solvents in a much shorter amount of time. Heating variance is unfortunately an issue with hotplates, as hotplates become warped by heat over time and hotplate-to-wafer contact deteriorates. To ensure contact over the full 2" wafer, the sample is placed on a flat aluminum plate that can evenly distribute heat from the hotplate.

The ideal temperature of the bake is found through a series of trials that involve the process of coating and pre-baking wafers, post-baking them at various temperatures and then exposing them to UV light at high dosage before development. If the post-bake temperature is too high, the resist layer will be thermally crosslinked and will remain in its entirety after development. If the temperature is too low, the resist

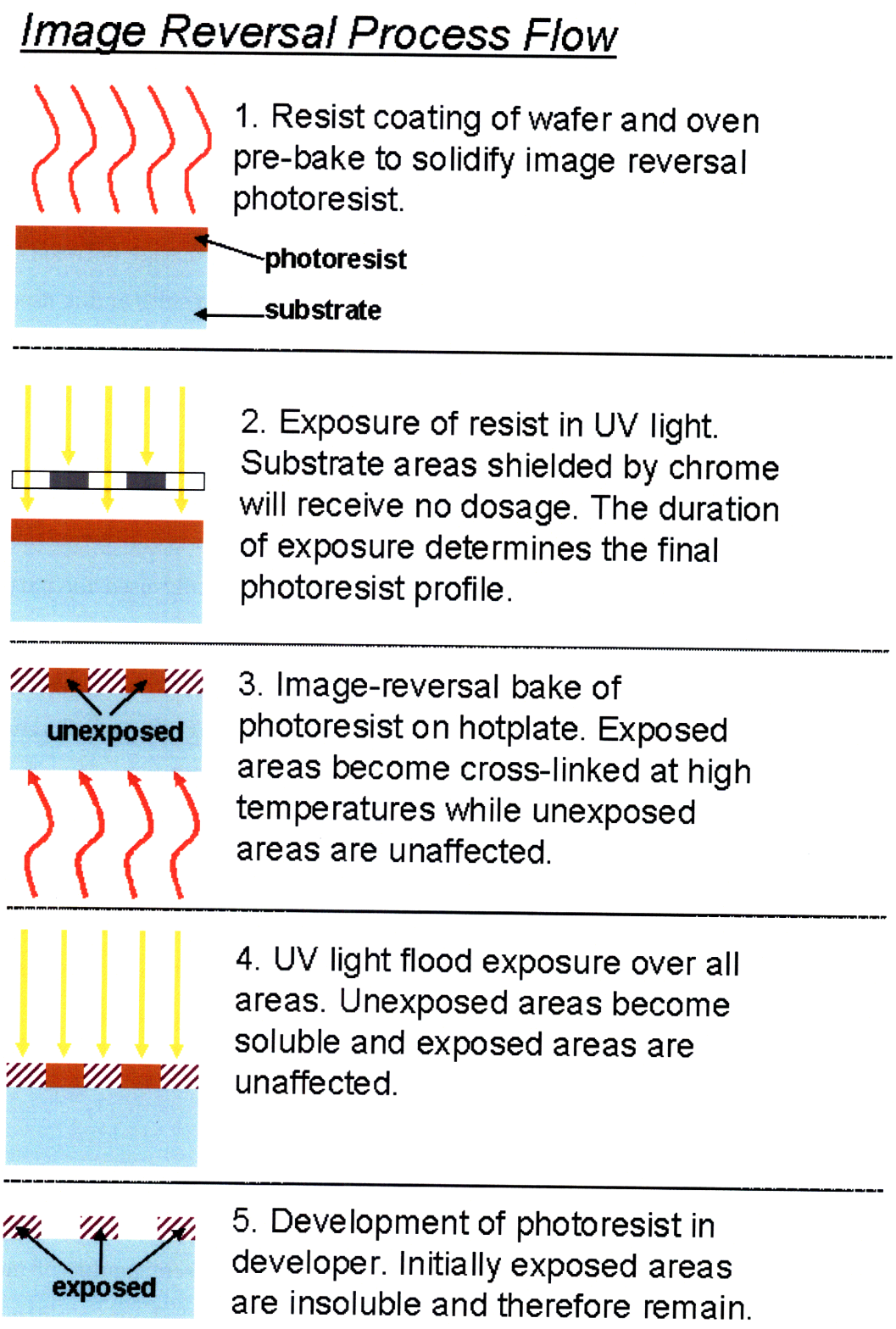

Figure 4-4: Image reversal photolithography process flow.

will be completely removed upon development. The tests enable the user to focus on a smaller temperature range that can deliver the desired photoresist patterns. A hotplate bake at 106°C for 1 minute was found to be optimal. The sensitivity of the resist's cross-linking agent requires that the bake temperature be kept within 1°C of this number for good image reversal photolithography.

The following long exposure, or flood exposure, is kept at a dosage between 200-600 mJ/cm^2. Overall, the flood exposure has little effect upon results and is used to loosen non-cross-linked areas of the resist; a dosage of approximately 560 mJ/cm^2 was therefore chosen. After exposure, the wafer is submerged in AZ422, a developer that is associated with the resist. The development, about 1 minute in length, is tracked in real-time to ensure that the devices are not under or over-developed, scenarios that result in resist not clearing thoroughly in unexposed areas or severe undercutting of the sidewalls respectively. The resulting resist pattern is typically used for pattern transfer through etching, or for a lift off process of evaporated metal layers.

The lift off is carried out by placing the substrate in acetone or more aggressive 80°C-heated N-Methylpyrrolidine (NMP) to dissolve remaining resist and remove metal in unwanted areas. Successful image reversal processes exhibit slightly slanted sidewall angles that bring about clean and quick lift off of excess metal in the less aggressive acetone. A comparison of lift off results from a previously used image reversal procedure using a convection oven for the post-bake and results from the optimized procedure described in this section is provided in Figure 4-5. A summary of the photolithography procedures and experiments is given in Appendix C.

4.1.2 Nickel Hard Mask

High-energy ion bombardment associated with reactive ion etching causes damage to the epitaxial structure that extends far below the surface. A hard mask is used to protect areas that are not to be etched, such as the doped semiconductor-metal contact interface. During the first process steps, metal is evaporated onto a patterned sample and lifted off to define the Mach Zehnder waveguide arms. This first metal must:

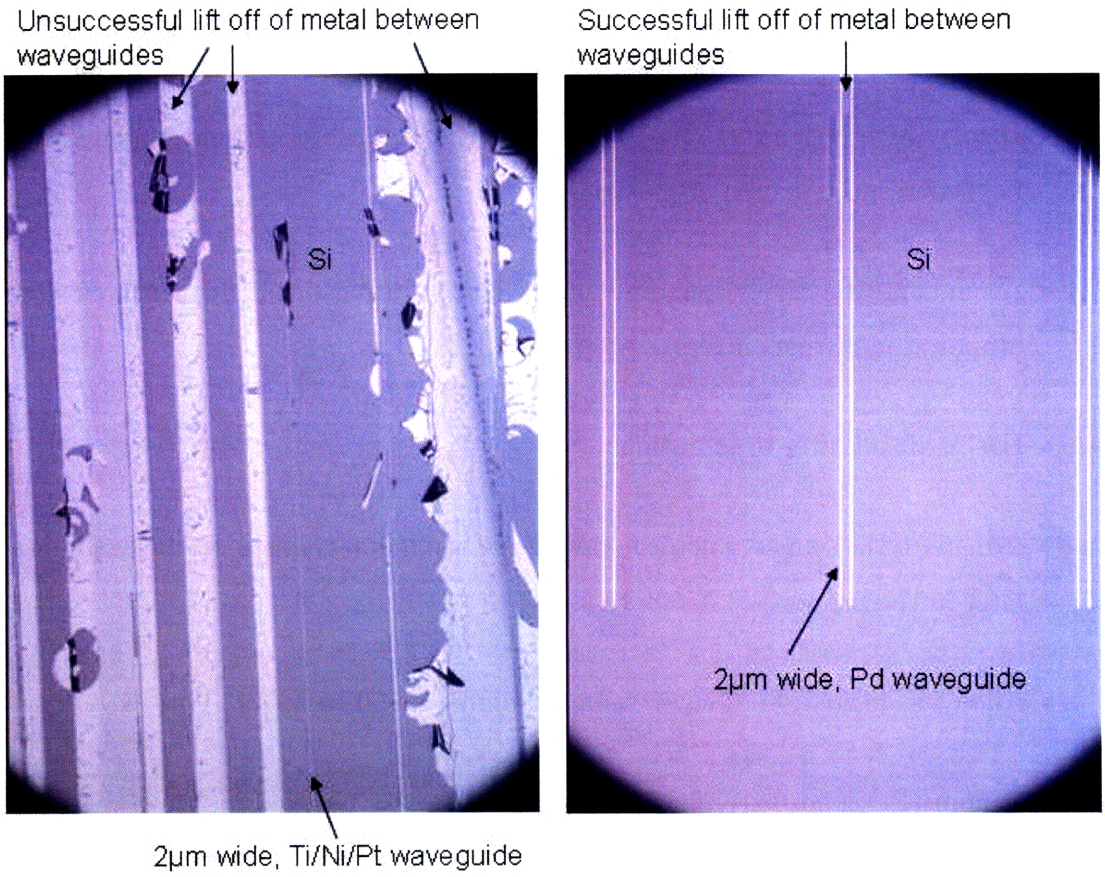

Figure 4-5: Nomarski micrographs of lift off using different image reversal procedures. An evaporated Ti/Ni/Pt (500 Å, 1500 Å, 50 Å) metal stack on a Si substrate (left) using the previous image reversal procedure provided in Appendix C with a convection oven post-bake is shown. The lift off, over 20 minutes in acetone, is clearly unsuccessful. Metal residing over areas with resist fails to detach from the metal waveguides deposited in open areas. An evaporated layer of Pd (1200 Å) on a Si wafer (right) illustrates successful lift off using the optimized image reversal procedure with a hotplate post-bake. The resist between the metal waveguides dissolved within 40 sec in acetone, leaving the region between metal lines clear. The successful lift off is attributed to the photoresist profile formed using this procedure.

- Withstand reactive ion etching in chlorine-based gas chemistries (used to remove the semiconductor material)

- Withstand reactive ion etching in fluorine-based gas chemistries (used to remove the silicon dioxide)

- Display high etch selectivity to the semiconductor materials and silicon dioxide in their respective etch chemistries

- Accumulate relatively low amounts of stress during deposition and allow the evaporation of thick layers

- Easily lift off after evaporation

- Adhere to the semiconductor material and top metal contacts (to be evaporated later in the process)

- Allow the formation of low-resistance, ohmic metal contacts

Platinum (Pt) is an extremely hard metal that was pursued in trials. However, its high evaporation temperature (around 1600°C) and configuration create sufficient stress within the layer, causing the Pt to completely "peel off" the substrate. Instead, a Titanium/Nickel/Platinum (Ti/Ni/Pt) metal tri-layer of various thicknesses as detailed in Table C.4 was experimented with in an attempt to reduce the built-in stress while maintaining the desired and necessary characteristics. The nickel layer, which is also known to be a good etch mask, was chosen as it is a relatively low-stress material. The titanium in the metal stack was added as an adhesion layer. However, the high evaporation temperature combined with the duration of the deposition required to achieve a relatively thick metal stack (over 200 nm thick) resulted in high-stress and poor adhesion due to peeling. Ultimately, a single 100 nm thick nickel layer proved to be adequate, with the thickness limited by the increasing difficulty of metal lift off as the underlying resist hardens during the Ni evaporation process step.

4.1.3 Reactive Ion Etching of III-V Materials

Patterns developed through photolithography are transferred to the epitaxial structure by means of reactive ion etching (RIE), a method of removing materials by sputtering and reactive plasma etching. RIE technology achieves anisotropic etches with directional ion bombardment, and allows flexibility in material selectivity dependent upon the chosen etch chemistry. Though reactive ion etching is also employed in the removal of SiO_2 and BCB, this section focuses on the etching of III-V materials, and $Al_xGa_{1-x}As$ and $In_yGa_{1-y}P$ in particular.

The etch tool used is a parallel plate (two electrode) system comprising of a chamber equipped with inlets allowing for gas introduction, an electrically powered stage on which the substrate is mounted and a grounded electrode. After entering the chamber, gases exit through a vacuum pump that also establishes and maintains low pressure within the system. During etching, a radio frequency (RF) field is applied through the powered electrode, ionizing molecules within the chamber and producing a plasma. Ionized molecular species from the plasma react chemically with substrate surface atoms to form volatile molecules or byproducts that must then be removed from the system by positive ions accelerating toward the substrate. The ion bombardment occurs as a result of a DC voltage, formed between the non-driven electrode and the plasma. Consequently, the physical etching enhances the removal of the byproducts created by chemical etching.

There are a few variables that are considered during reactive ion etching, namely chamber pressure, DC voltage (or RF power), gas flow, material selectivity and time. A longer mean free path translates into fewer inter-ion collisions which result in increased ion energy. Decreasing the chamber pressure increases ion energy, encourages directionality and improves anisotropy, but reduces the etch rate as atom concentration drops. Chamber pressure is typically in the mTorr range or lower. Greater RF power increases ionization through increased electron energy. A higher DC bias fuels the physical aspect of the etch, improving anisotropy, and simultaneously increases the etch rate and mask sputtering (etch selectivity becomes an issue) [40]. A higher

flow rate can have also affect selectivity and anisotropy to a certain extent, but is less critical than the previous variables discussed.

Chamber Cross-contamination

Reactive ion etch chambers are said to have a memory of previous processing steps [40]. Etch masks and substrate materials, sputtered by ion bombardment, remain in the chamber long after the etch process by adhering to chamber walls and electrodes. In subsequent etches, the sputtered residual materials remains combine with gaseous byproducts and redeposit on the samples in the form of large particles, leading to an etched surface with 'grass' which can negatively affect entire devices and lower yields. In addition, material debris and gas residue in the chamber occasionally act as ions and become part of the etching process, emerging from the walls and bombarding the substrate without directionality. The etching becomes isotropic, and a large amount of feature undercut is expected.

Several techniques may be taken to combat the negative situations described above. Firstly, etching tools can be dedicated for a specific process - involving similar materials and gases - repressing the introduction of new byproducts into the system and preventing cross-contamination between different substrates and etch residue. Secondly, the chamber can undergo cleaning procedures designed to remove byproduct formations. A careful chamber clean dramatically improves the performance (of even non-dedicated machines) as well as etch consistency by bringing the chamber back to a clean status rather than etching in a questionable environment. Finally, a conditioning process conducted immediately before an important etch, and involving the same gas chemistry, readies the chamber, mimicking the exact environment in which the etch is performed. The conditioning run provides a transition between the cleaning step and the final etch of the device.

Cleaning and Conditioning Procedures

The reactive ion etching tool employed for the etching of the $Al_{0.8}Ga_{0.2}As/In_{0.53}Ga_{0.47}P$ stack is not a dedicated tool for these materials or the BCl_3 chemistry used. Hence,

the development of a cleaning regimen that can effectively remove BCl_3 and Cl_2 (another heavily used gas in the tool employed here) etch residue is critical to the success of the reactive ion etching. Cl_2 etching remains are especially harmful - its by-products are difficult to remove from the chamber and induce undercutting and high etch rates [41] in consequent etches. The effects of Cl_2 in the chamber during a BCl_3 etch of a 2 μm wide GaAs ridge are visible in the left image of Figure 4-6. The Cl_2 gas chemistry causes deterioration of the Ni etch mask, and the gas byproducts in the chamber lead to isotropic etching of the GaAs ridge. Additionally, the Cl_2 residue results in 'grass' due to an increased etch rate which promotes a more physical etch rather than an etch that relies on chemical removal of the GaAs.

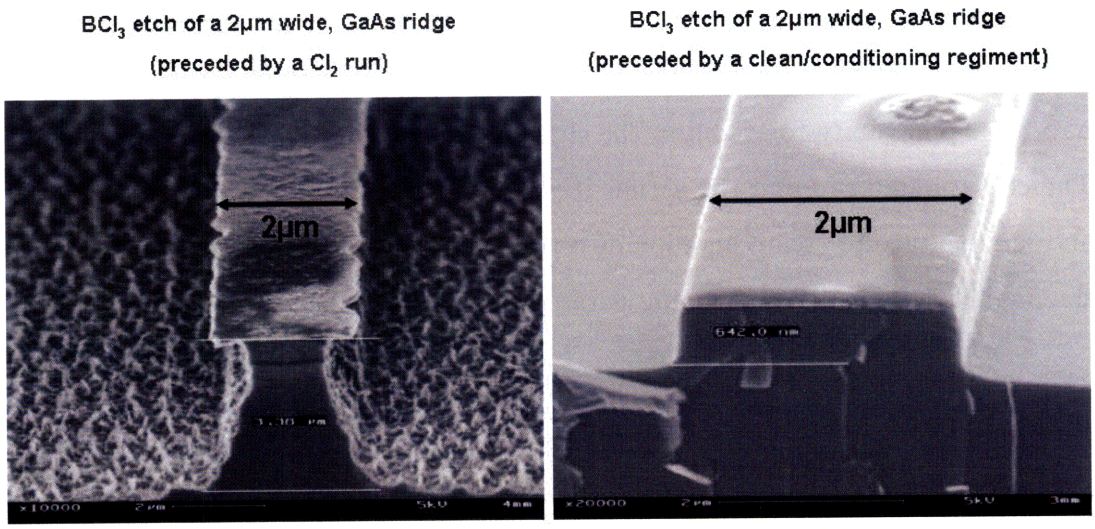

Figure 4-6: Scanning Electron Micrograph (SEM) images of GaAs ridges etched using identical BCl_3 conditions for 8 minutes with (right) and without (left) a prior chamber cleaning regiment. An etch preceded by a Cl_2 run (left) exhibits considerable undercutting of the structure, increased etch rate (422nm/min) and 'grass'. A similarly conducted BCl_3 etch preceded by a cleaning (CF_4/O_2) plasma and conditioning (CHF_3/O_2, BCl_3) regimen (right) illustrates smooth topography, straight sidewalls with no undercut and a slower, controlled etch rate (78nm/min).

RIE chamber preparation consists of three steps. The first is a CF_4/O_2 plasma clean that removes debris from the chamber walls. To track the cleaning, the RF power is set and the DC bias is monitored. As the byproducts are removed, the RF

power remains the same while the corresponding voltage drops. The chemistry of the clean follows typical cleaning processes, but the 1:2 CF_4:O_2 ratio is higher due to the aggressiveness required to remove remnants of BCl_3 and Cl_2. The clean is carried out at a relatively high pressure of 36 mTorr, resulting in isotropic etching, in order to successfully reach all areas of the chamber.

The second step is a coating process that employs CHF_3/O_2 gas flow in a 4:1 ratio. The chemistry forms a teflon-like coating over the chamber walls that restrains any remaining particles, and hence thwarting redeposition. The coating also prevents new particles from adhering to the chamber. The second step is performed at 11 mTorr to sufficiently coat the entire chamber. The third step is a very short conditioning run that mimics the actual etch to be used to process the device. The BCl_3 procedure prepares the chamber environment, but is kept short to ensure that few molecules have the opportunity to attach to the chamber and react with the nickel hard mask. The conditioning run and the actual III-V etch are performed at very low pressure and high voltage to create high ion directionality and anisotropic etching. Details of the final cleaning and conditioning parameters can be found in Appendix B.

4.1.4 Planarization Techniques

Metal evaporation using an electron beam evaporation is directional and does not cover sidewalls. Consequently, the topography on which the evaporation is performed must be as flat as possible (ensuring a uniform deposition). Furthermore, the material used to planarize the surface for top-side metal contacts must also be electrically insulating to ensure electrical isolation of the powered devices, and be able to withstand heat and agitation during measurements. To fill in the >1 μm deep trenches and planarize areas between ridges, two spin-on dielectrics - Hydrogensilsequioxane and Benzocyclobutene - were explored.

Hydrogensilsequioxane (HSQ)

HSQ is an easily applied, flowable dielectric polymer. Though the material appears to diffuse into and react with III-V semiconductor material [5], HSQ is still a successful planarization technique. To overcome the absorption of HSQ in the III-V semiconductor, a 70 nm thick layer of SiO_x is first deposited by chemical vapor deposition (CVD). Dow Corning Fox 25 HSQ selected for experimentation is dispensed statically and spun at 3000 rpm for 1 minute. Fox 25 HSQ spins to a thickness of 580-810 nm for spin speeds ranging between 2000-4000 rpm and is considered to be on the thicker end of HSQ layers. At 3000 rpm, the HSQ layers spins uniformly, a concern as spin uniformity tends to deteriorate with a reduction in spin speed. After coating with HSQ, the sample is baked on a hotplate at 120°C for 1 minute, immediately followed by a 180°C bake for 1 minute and a 5 minute, 350°C bake. Ideally, the layer is annealed at 400°C in nitrogen ambient, but as facilities at MIT are lacking for this step, the final hotplate bake was extended from 3 minutes to 5 minutes.

Results of initial trials involving HSQ planarization of GaAs etched trenches, approximately 1.3 μm in depth, are shown in Figure 4-7. The transition areas between

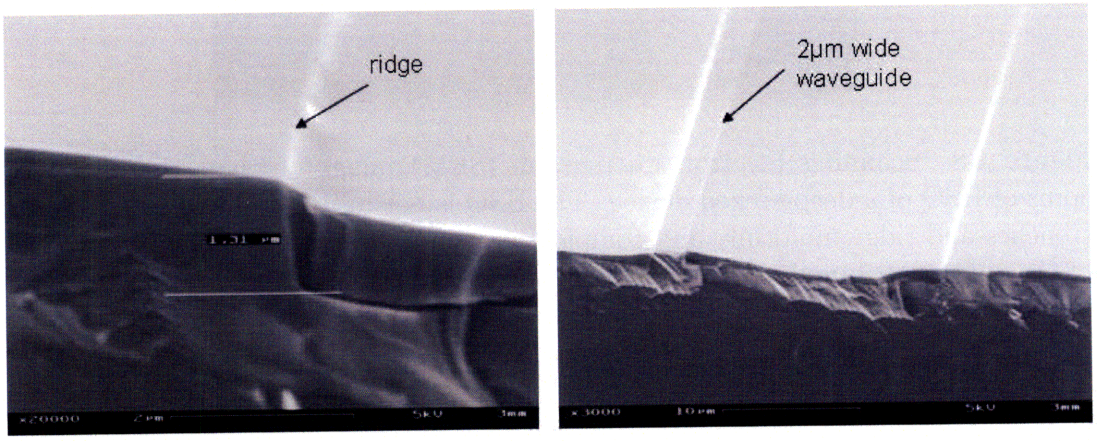

Figure 4-7: Scanning Electron Micrograph (SEM) images of HSQ-planarized GaAs trenches. A close view of a 2 μm ridge sidewall (left) reveals non-uniformity across the ridge and trench. The waveguide outline is easily visible (right), indicating that the ridge and the filled trench are not conformally coated and one HSQ spin is insufficient for planarization.

the ridges and the trenches reveal non-uniformity in spinning due to insufficient HSQ layer thickness. The HSQ itself, however, appears well-cured and smooth, and so two HSQ spins were thought to be sufficiently thick to bury the devices. When applied to an actual deep-etched device, the results, given in Figure 4-8, were poor. Due to a combination of thermal shock and stress, the HSQ cracked and delaminated following a second spin. Additionally, the HSQ was too viscous, creating non-uniformity in trench filling on either side of the waveguide. Though a new recipe for HSQ curing (involving a gradual increase in temperature from 210°C to 350°C as well as a gradual cool-down) was developed to reduce stress in the layer, the results were not satisfactory and another method of planarization was sought.

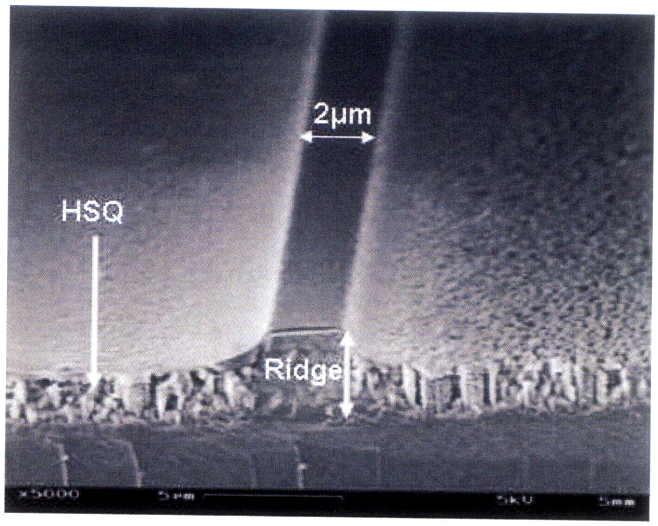

Figure 4-8: Scanning Electron Micrograph (SEM) image of planarization by two spins of HSQ of a deep-etched device. The HSQ is not fully cured and fails to fill the trenches and ridge uniformly and completely. Non-uniformity between the two sides of the ridge, attributed to HSQ viscosity and spin direction, is also visible.

Benzocyclobutene (BCB)

The Dow Corning 3000 Cyclotene series is a spin-on insulator with a low dielectric constant designed for dry etching purposes. The 3022-35 BCB product, composed of carbon and silicon, spins to a thickness range of 1.0-2.4 μm for spin speeds of 2000-4000 rpm, and is an especially attractive method of planarization as it can be cured

at a relatively low temperature and does not outgas in the process.

Before BCB application, the sample undergoes a standard solvent rinse and is baked in a 130°C oven for 20 minutes to dispel moisture. A Dow Corning adhesion promoter, AP3000, is statically dispensed and spun at 2500 rpm for 20 seconds and baked for 5 minutes on a 100°C hotplate to improve adhesion between the BCB and semiconductor. BCB is statically dispensed and spun at 2500 rpm for 25 seconds to form a layer approximately 1.3 μm thick after curing. The sample is soft cured for 1 minute on a 100°C hotplate to solidify the layer, and then transferred to an annealing tube where it is hard cured in a 250°C nitrogen ambient for 1 hour. Figure 4-9 of a device fabricated by Dr. Ryan Williams shows a BCB-planarized surface.

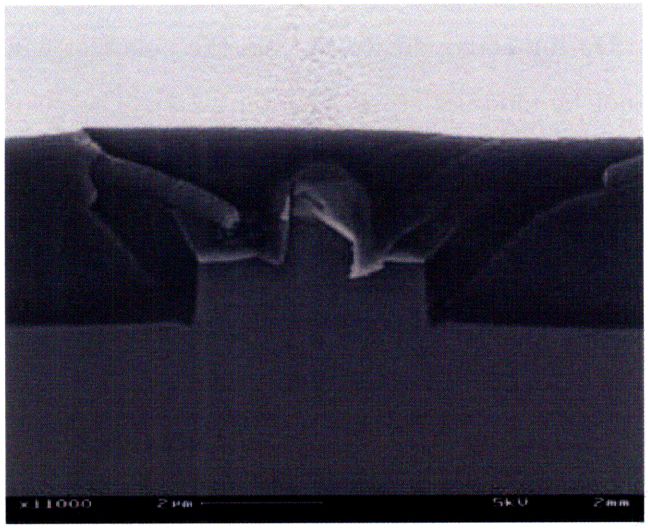

Figure 4-9: Scanning Electron Micrograph (SEM) image of planarization by BCB of an active device fabricated by Dr. Ryan Williams [5]. The BCB buries trenches and waveguides of over 2.5 μm in depth and creates a surface that is easily etched back.

The etching of BCB involves CF_4 and O_2 gases to remove the silicon and carbon components respectively. Oxygen plasma without fluorine creates a brittle amorphous silicon oxide layer on the etched surface, so the development of a ratio that successfully etches and removes all BCB components is important. Dr. Ryan Williams developed an etching process consisting of 60% CF_4 at a pressure of 15 mTorr and 100 Volts that removes BCB at a rate of 100 nm/minute. The sample is monitored throughout

the etch by microscope to determine the etch time required to reveal the metal on the Mach Zehnder arms without over-etching surrounding areas.

4.2 Device Characterization

Passive testing of fabricated modulators provides information about the device performance, namely power transmission and loss - critical knowledge in assessing the design and fabrication quality. For the purpose of measuring passive waveguides, the frequency combs that were described in Section 2.1 are unnecessary; a continuous beam of light in the modulator wavelength range and generated by a tunable laser source is sufficient. The laser beam is passed through a polarizer that removes undesired polarization. During active device testing, the polarizer will eliminate the TM mode (which can not be modulated, see Section 2.2.4). The beam is coupled in and

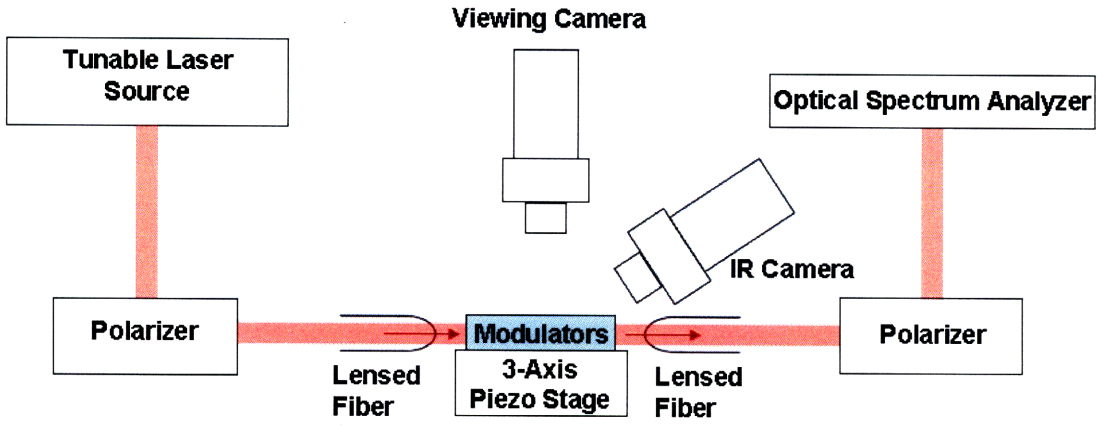

Figure 4-10: Apparatus setup for the testing of passive modulators. A polarizer absorbs the undesired beam polarization of a wavelength-tunable laser source-generated optical beam. The beam is coupled to the modulators through lensed fibers, and continues on to an optical spectrum analyzer through another polarizer. The analyzer and infrared camera situated at the modulator output provide information about the transmission, loss and dispersion of the measured device.

out of the device using a lensed fiber positioned on a 3-axis piezo stage. Alignment of the device, situated on a similar stage, and fiber is accomplished using images supplied by a top-view camera. Another camera capable of capturing infrared light is

placed at the waveguide output, generating images of light dispersion along the full length of the device. The beam is coupled out to a polarizer, and continues through to an optical spectrum analyzer (OSA) synchronized to the laser source. The OSA measures optical transmission as a function of wavelength; information that is used to measure the loss through the device via the ratio of output power to input power, $\frac{P_{output}}{P_{input}}$. Measurements, carried out by Marcus Dahlem and advised by Professors Erich Ippen and Franz Kaertner of the Optics and Quantum Electronics Group at MIT, are currently underway.

Chapter 5

Modulator Integration

The structures discussed thus far provide an excellent basis for more sophisticated devices. To successfully integrate modulators with other optical components such as arrayed waveguide gratings and electrical components, the modulators need to be low-loss, efficient and operate with low voltages. Novel heterostructures exhibiting better mode confinement (and associated advantages) and signal demultiplexers based on new material designs are presented in this chapter. When combined, the modulators and demultiplexer devices construct a system capable of generating ultra broadband arbitrary optical waveforms.

5.1 MOS-Based Structure

Low-loss devices demand a high degree of mode confinement. The deep-etched arsenide-based structure, an improvement over the shallow-etched device, limits the mode movement and expansion laterally but not the vertically. Uncontained, the mode can couple to the substrate or approach the metal contacts and suffer optical loss. A far more restricting epitaxial design, presented in Figure 5-1, has been developed to improve device performance.

Several aspects of the previous structure have been adopted and integrated into the new heterostructure. Thick lower and upper $Al_{0.8}Ga_{0.2}As$ cladding layers isolate the mode from the substrate and electrical contacts respectively. Like the original

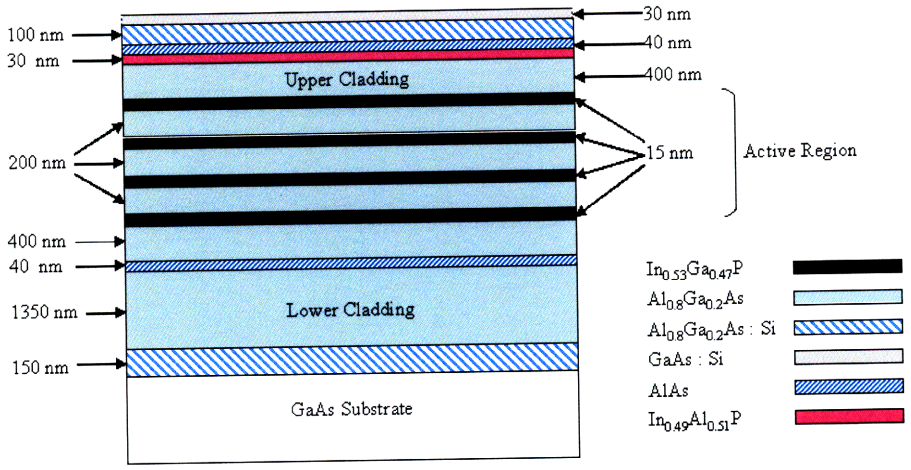

Figure 5-1: Epitaxial heterostructure of an MOS-based, $Al_{0.8}Ga_{0.2}As/In_{0.53}Ga_{0.47}P$ structure. The 40 nm AlAs layers can be oxidized to physically isolate the active region and contain the optical mode vertically. A thin, 30 nm $In_{0.49}Al_{0.51}P$ layer has been added as an etch-stop for the first III-V material, BCl_3 etch.

structure (see Section 3.2.2), the new design has a dilute core composed of repeating 200 nm thick, low-index $Al_{0.8}Ga_{0.2}As$ and 15 nm thick, high-index $In_{0.53}Ga_{0.47}P$ layers. The resultant active region has an index of refraction only slightly higher than its surroundings, leading to a reduction in coupling loss, but provides sufficient mode confinement. Additionally, the upper and lower Si-doped GaAs layers have a lower bandgap to aid in making contact to evaporated metal layers. The refractive indices of materials used in the heterostructure are provided in Table 5.1.

Two AlAs layers and a $In_{0.49}Al_{0.51}P$ layer have been added to the original heterostructure. The AlAs layers can be thermally oxidized to form Al_xO_y layers, as shown in Figure 5-2, to strongly confine the optical mode in the middle of the structure. The oxidized layers also enable the modulator to withstand higher operating voltages both in reverse and forward bias without concern of breakdown or carrier loss. Consequently, the device is essentially unipolar and can be powered in a push-pull manner (see 2.3.1), which reduces the required Mach Zehnder arm length. The $In_{0.49}Al_{0.51}P$ layer serves as an etch stop in fabrication. Selectivity between AlAs and $Al_{0.8}Ga_{0.2}As$ during RIE is poor, and an etch stop is necessary to prevent overetching. The mask set developed for the reverse-biased, shallow and deep-etched structures

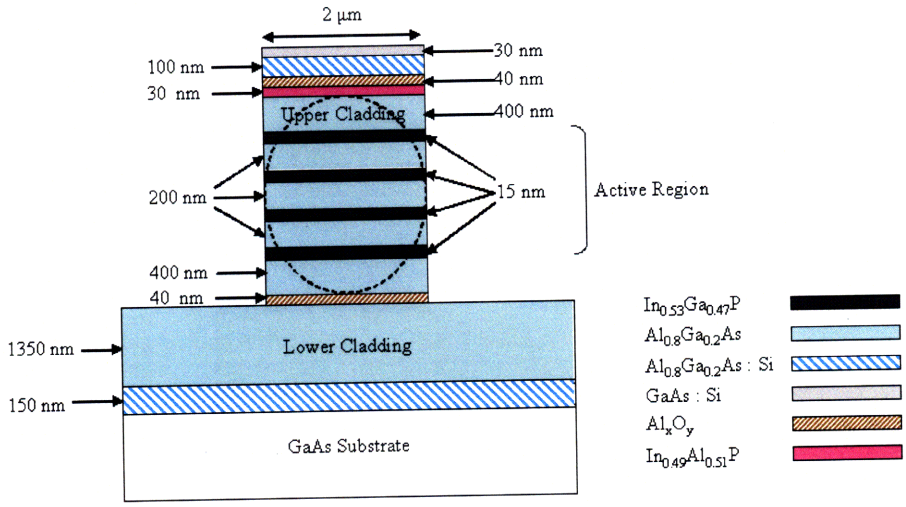

Figure 5-2: MOS-based, $Al_{0.8}Ga_{0.2}As/In_{0.53}Ga_{0.47}P$ modulator heterostructure with a 2 μm ridge. The epitaxial structure must be etched down to the lower AlAs layer to allow for oxidation. The 40 nm Al_xO_y (oxidized AlAs) layers confine the mode (displayed in dashes) and active region physically and electrically. Consequently, both forward and reverse bias can be applied across the device.

accommodates this heterostructure design as well. The modulator fabrication process remains identical with the exception of an added oxidation step after the second semiconductor etch and prior to BCB planarization (the AlAs must be exposed by a semiconductor RIE step for oxidation to occur).

Table 5.1: Refractive indices at 800nm of materials composing the $Al_{0.8}Ga_{0.2}As$ / $In_{0.53}Ga_{0.47}P$ MOS-based modulator.

Material	**Index at 800nm**
GaAs	3.64
$Al_{0.8}Ga_{0.2}As$	3.14
$In_{0.53}Ga_{0.47}P$	3.32
InAlP	2.99
AlAs	2.96
Al_xO_y	1.60

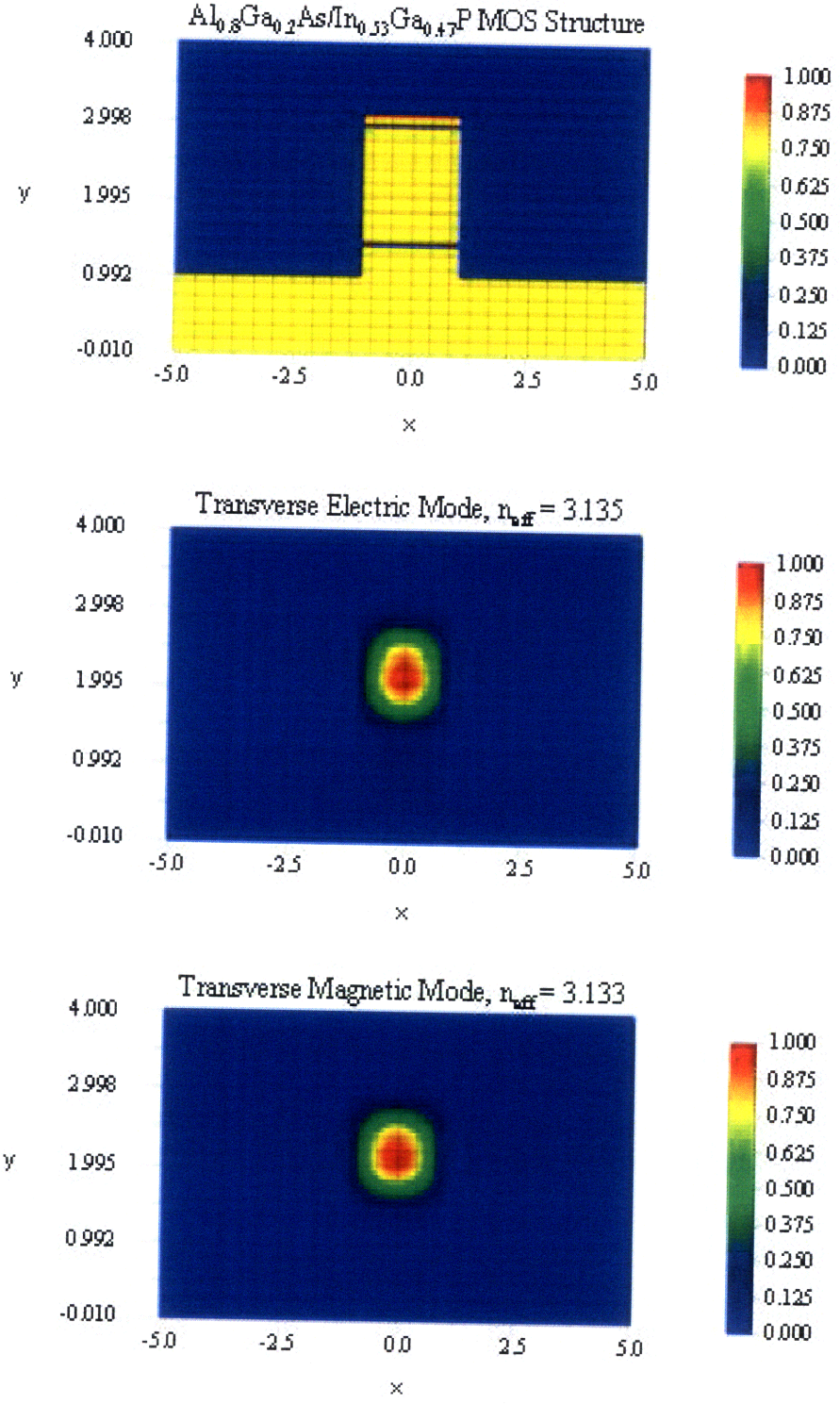

Figure 5-3: Mode simulations for the $Al_{0.8}Ga_{0.2}As/In_{0.53}Ga_{0.47}P$ MOS-based ridge waveguides using OptiBPM 5.2. The simulated epitaxial structure is shown (top) as well as the computed TE mode profile (center) and TM mode profile (bottom). Calculated indices associated with the profiles are also included.

5.1.1 Comparison to Previous Designs

Figure 5-3 displays the TE and TM mode profiles and associated indices for the MOS-based structure. Both modes are approximately 1.75 μm x 1.3 μm (WxH) in size. Though the new heterostructure does not offer increased lateral confinement of the mode over the reverse-biased deep-etched device (the 2 μm ridge width is identical), it provides superior vertical confinement by comparison to the 1.78 μm x 2.4 μm (WxH) mode dimensions of the deep-etched structure.

The natural birefringence in this structure is estimated to be $1.65 \cdot 10^{-3}$ at 800 nm, approximately equal to the birefringence of previously discussed structures. The values are similar as the overall layer configuration and material choices are nearly identical.

The voltage required to achieve a phase shift of π was calculated in the manner described by Appendix A and used in Section 3.2.3. r_{52} is again taken to be approximately equal to value of the more well-known r_{41} (in bulk semiconductors, $r_{41} = r_{52} = r_{63}$). The unknown tensors, r_{12} and r_{32}, are assumed to be the same as r_{52} (or equal to zero as in a bulk modulator), and the electro-optic tensors represent the overall contributions of all the layers combined. The calculated V_π values presented in Table 5.2 are computed for the TE mode with an effective refractive index of 3.13, modulator lengths ranging from 3 mm to 10.5 mm, a ridge height of 1.3 μm, (equivalent to the mode height), and for the operational wavelength of 800 nm. The values of the corresponding deep-etched structure calculations are also provided for comparison. Additional voltage calculations based upon other electro-optic coefficient possibilities are available in Appendix A (see Tables A.4, A.5 and A.6). The MOS

Table 5.2: Calculated values of V_π for the $Al_{0.8}Ga_{0.2}As/In_{0.53}Ga_{0.47}P$ MOS and deep-etched devices of various lengths oriented in the $< 011 >$ direction. This calculation assumes $r_{12} = r_{32} = r_{52} = 1.0 \cdot 10^{-12}$ m/V.

Device Length (mm)	3.0	4.5	6.0	7.5	9.0	10.5
MOS Device Voltage (V)	3.75	2.50	1.88	1.50	1.25	1.07
Deep Device Voltage (V)	6.84	4.56	3.42	2.74	2.28	1.96

device requires approximately half the voltage of the deep-etched structure to achieve a phase shift of π. The noteworthy decrease in V_π is attributed mainly to better mode confinement, which reduces the value of t_g, the height of the modulator active region.

5.2 All AlGaAs MOS-Based Structure

An additional MOS-based modulator design, with an active region composed entirely of AlGaAs layers of various degrees of Al content, is illustrated in Figure 5-4. The dilute core of the heterostructure consists of repeating low index $Al_{0.26}Ga_{0.74}As$ layers and high index $Al_{0.18}Ga_{0.82}As$ layers (refractive indices are provided in Table 5.3). Though the modulation bandwidth is reduced from 650 nm$< \lambda <$ 950 nm to 750 nm$< \lambda <$ 850 nm, the bandwidth remains large and more than sufficient for the purpose of this work.

Table 5.3: Refractive indices at 800nm of materials composing the all AlGaAs MOS-based modulator.

Material	**Index at 800nm**
GaAs	3.64
$Al_{0.26}Ga_{0.74}As$	3.51
$Al_{0.18}Ga_{0.82}As$	3.58
AlAs	2.96
Al_xO_y	1.60

Growth of low Al content AlGaAs layers by MBE is easier than the deposition of a combination of high Al content AlGaAs and InGaP layers. Furthermore, the near-uniform material composition of the active region eases the RIE process, which etches $Al_{0.8}Ga_{0.2}As$ and $In_{0.53}Ga_{0.47}P$ at different rates. As with the previous MOS structure, oxidized AlAs layers confine the vertical movement of the optical mode. However, no InAlP etch stop layer is necessary as the top cladding layer was increased in thickness. The 2.175 μm lower cladding layer was made considerably thicker than in previous designs as an additional precaution, preventing the mode from coupling

to the substrate.

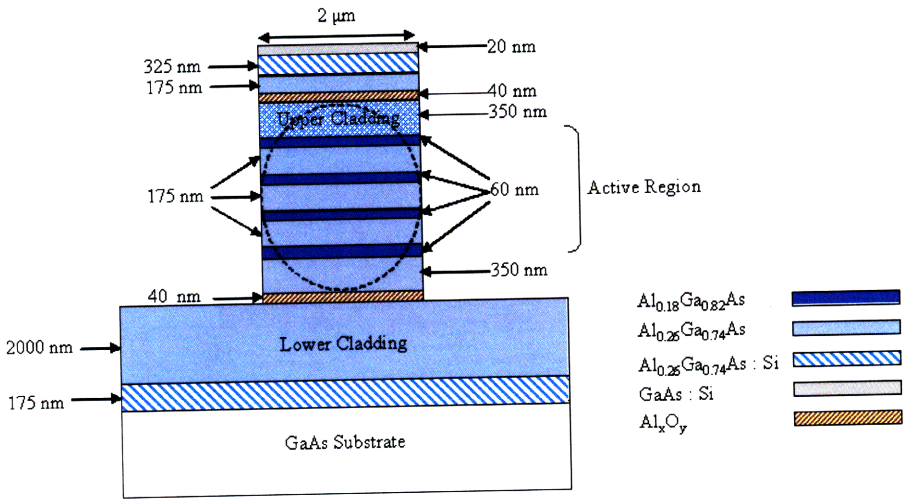

Figure 5-4: MOS-based, $Al_{0.26}Ga_{0.74}As/Al_{0.18}Ga_{0.82}As$ device heterostructure with a 2 μm ridge. The all AlGaAs active region simplifies the semiconductor RIE process required to expose the AlAs layers for oxidation. The 40 nm Al_xO_y (oxidized AlAs) layers confine the mode (displayed in dashes) and active region physically and electrically. Consequently, both forward and reverse bias can be applied across the device.

5.2.1 Comparison to Previous Designs

Figure 5-5 exhibits the TE and TM mode profiles and associated indices for the all AlGaAs MOS-based structure. Both modes are approximately 1.75 μm x 1.25 μm (WxH) in size. The mode confinement capability of the device is only a slight improvement over the previous MOS design (1.75 μm x 1.3 μm), but prevails over the reverse-biased shallow-etched and deep-etched structure.

The natural birefringence in this structure is estimated to be $7.9 \cdot 10^{-4}$ at 800 nm. The similar high and low index materials allow the mode to feel a near-uniform surrounding, reducing the birefringence.

The voltage required to achieve a phase shift of π was calculated using the techniques described in Appendix A and utilized in Sections 3.2.3 and 5.1.1. The calculated V_π values presented in Table 5.2 are computed for a TE mode with an effective index of 3.51, modulator lengths ranging from 3 mm to 10.5 mm, a ridge height of

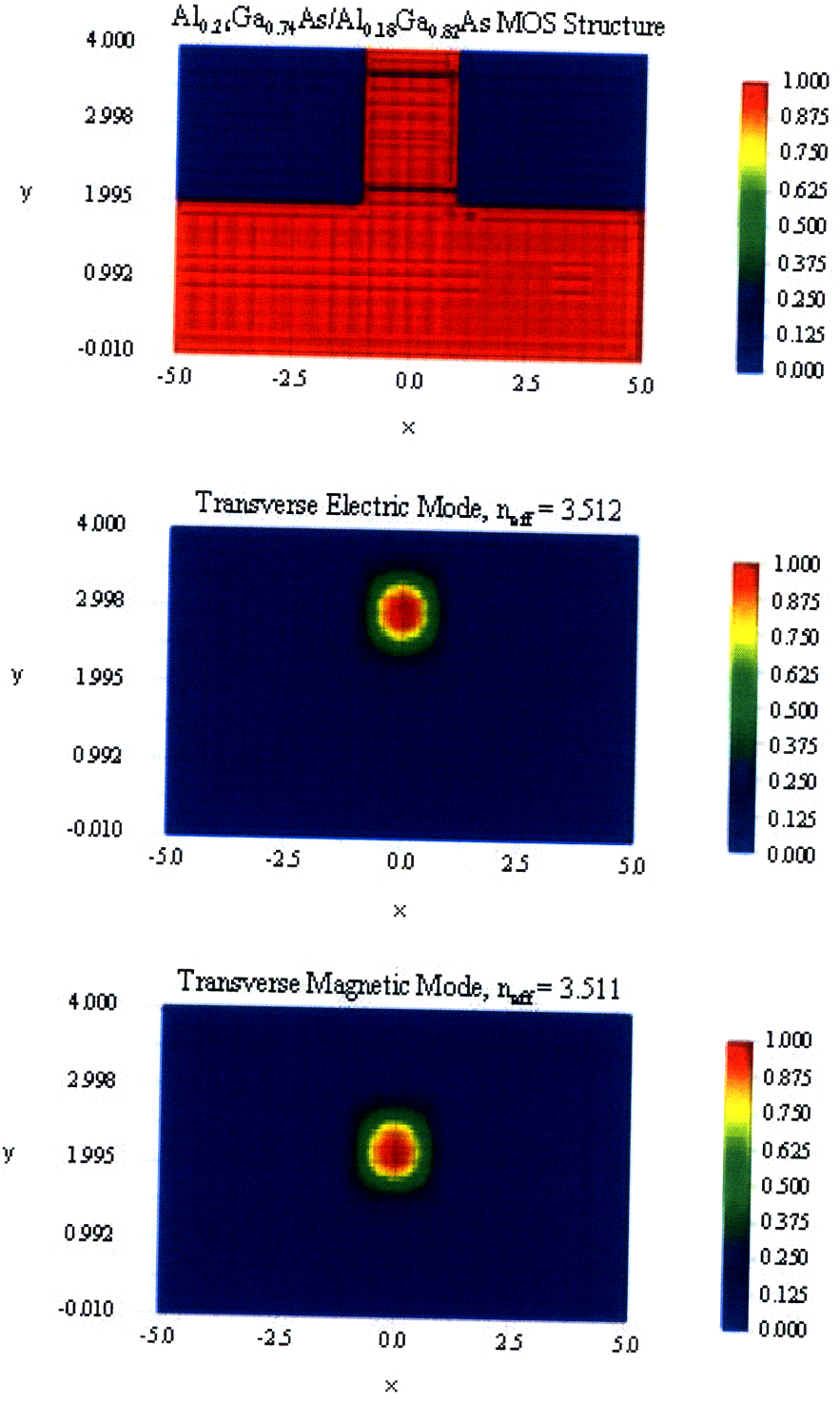

Figure 5-5: Mode simulations for the $Al_{0.26}Ga_{0.74}As/Al_{0.18}Ga_{0.82}As$ MOS-based ridge waveguides using OptiBPM 5.2. The simulated epitaxial structure is shown (top) as well as the computed TE mode profile (center) and TM mode profile (bottom). Calculated indices associated with the profiles are also included.

1.25 μm (equivalent to the mode height), and for the operational wavelength of 800 nm. More voltage calculations based upon other electro-optic coefficient possibilities are available in Appendix A (see Tables A.7, A.8 and A.9).

Table 5.4: Calculated values of V_π for $Al_{0.26}Ga_{0.74}As/Al_{0.18}Ga_{0.82}As$ MOS devices of various lengths oriented in the $< 011 >$ direction. This calculation assumes $r_{12} = r_{32} = r_{52} = 1.0 \cdot 10^{-12}$ m/V.

Device Length (mm)	3.0	4.5	6.0	7.5	9.0	10.5
All AlGaAs MOS Device Voltage (V)	2.57	1.71	1.28	1.03	0.86	0.73

The lower required voltage is attributed to increased mode confinement and the heterostructure's higher index of refraction (n^3 is inversely proportional to V_π).

5.3 Arrayed Waveguide Gratings (AWGs)

Arbitrary waveform generation is obtained by the phase and amplitude modulation of frequency comb components. Hence, optical wavelength demultiplexers and multiplexers are necessary for spatial separation and recombination of wavelength components prior to and following modulation. An NxN arrayed waveguide grating (AWG) with N input and output waveguides is bi-directional, and serves as both a demultiplexer and multiplexer.

A schematic of an AWG created by Smit et. al. [6] is presented in Figure 5-6. The device consists of a phased array of waveguides positioned between two free propagation regions, or FPRs. An incoming beam propagates through a single-mode input waveguide and enters the free propagation region where it is laterally unconfined. The beam is coupled into the single-mode waveguide array at the input aperture and travels through the waveguide until reaching the output aperture, where another FPR is situated. As the optical signal moves through the FPR, light that was diffracted from waveguides in the phased array section constructively interferes and focuses at the image plane where it is captured by strategically-placed output waveguides, each of which carries a distinct wavelength.

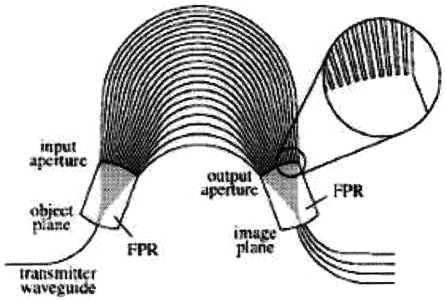

Figure 5-6: Schematic of a an arrayed waveguide grating illustrated by Smit et. al. [6].

A waveguide in the phased array section is longer than its neighbor by a length, ΔL, defined as

$$\Delta L = m\frac{\lambda_c}{n_{eff}} \tag{5.1}$$

where m is an integer representing the array order, λ_c is the central wavelength of the device and n_{eff} describes the effective index of refraction of the waveguide. Light at the central frequency displays unaltered phase and a consistent field distribution at the output aperture, and is focused at the center of the image plane. The length adjustment creates a phase distribution (that varies linearly at the output aperture) over other frequencies in the waveguide array, tilting the beam and moving the focal point along the image plane [6] to corresponding frequency channel output waveguides. As a result, the device output is extremely sensitive to phase variance, and miscalculation or fabrication errors can result in unsuccessful frequency channel separation.

The phase difference, $\Delta\Phi$, between neighboring waveguides is determined by

$$\Delta\Phi = \beta\Delta L \tag{5.2}$$

for β, the waveguide propagation constant. The movement of the focal point along the image plane is periodic and repeats for every phase shift of 2π. The frequency shift that accommodates $\Delta\Phi = 2\pi$ is referred to as the free spectral range, or Δf_{FSR},

computed by

$$\Delta f_{FSR} = \frac{c}{\widetilde{N}_g \Delta L} \tag{5.3}$$

where c is the speed of light. $\widetilde{N}_g$ is the group index of the waveguide mode and varies with frequency, f. $\widetilde{N}_g$ is calculated by

$$\widetilde{N}_g = N_g + f\frac{dN_g}{df} \tag{5.4}$$

5.3.1 Design and Simulation

An Optiwave WDM Phasar simulation program was employed in the design of an arrayed waveguide grating. The AWG, displayed in Figure 5-7a, employs the all AlGaAs MOS-based structure and makes use of the superior mode confinement capability of the heterostructure. The device has eight input and output waveguides that are 2 μm wide. As the input aperture of the free propagation region is approached, the waveguide width gradually increases to 3 μm over a length of 50 μm. The output waveguides taper in width at the output aperture, scaling back from 3 μm to 2μ over a similar length. The tapering, and inversely the increase in waveguide width, allows the optical mode to smoothly transition from the confined waveguides to the dispersive free propagation region. The thirty waveguides in the phased array section similarly taper from a width of 4 μm to 3 μ. At the first FPR output, where the waveguides are 4 μm wide, there is no space between the waveguides, encouraging full transmission of the diffracted power from the first FPR to the phased array waveguides and on to the second FPR. The specifications of the AWG are provided in Table 5.5.

The simulation results of the designed arrayed waveguide gratings device, provided in Figure 5-7b, display the AWG output power (dB) of each wavelength channel as seen from the 4th output port. The distinct wavelength channels, identified by different colors in the figure, are spatially separated and exhibit an output power of over 23 dB and channel crosstalk around 30-40 dB.

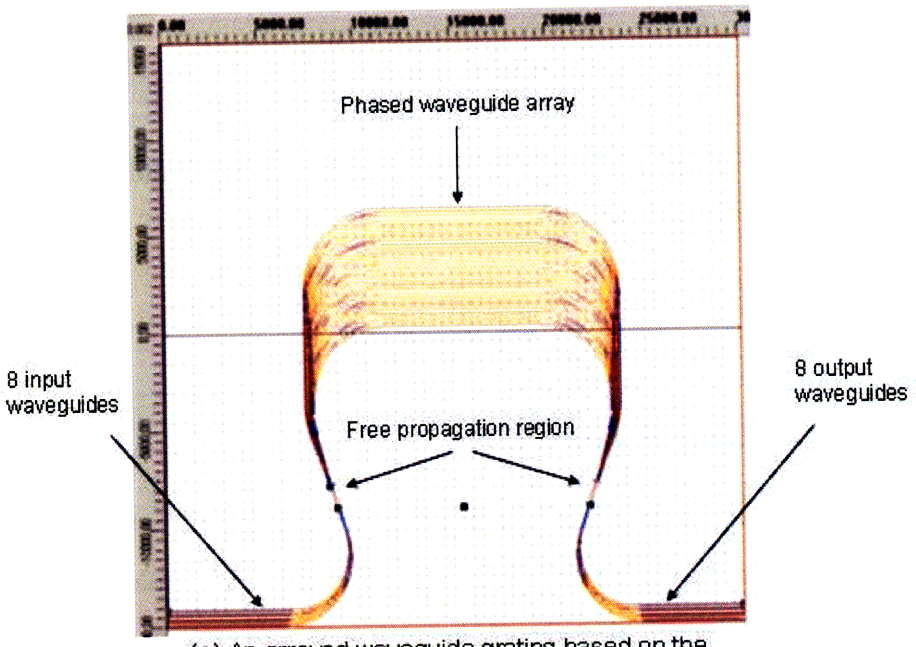

(a) An arrayed waveguide grating based on the $Al_{0.26}Ga_{0.74}As/Al_{0.18}Ga_{0.82}As$ MOS-based structure.

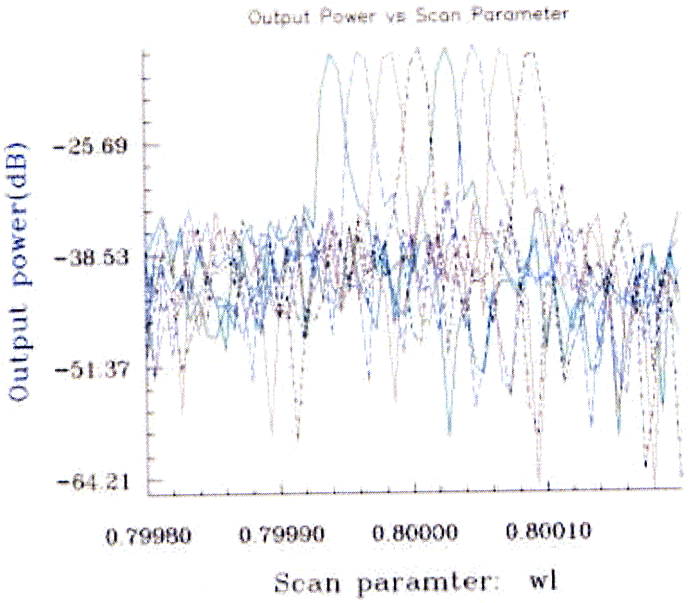

(b) WDM_Phasar simulation of spatial frequency separation of the AWG in (a).

Figure 5-7: Layout design and simulation of an arrayed waveguide grating by the Optiwave WDM Phasar software. The AWG (a) is based on an $Al_{0.26}Ga_{0.74}As/Al_{0.18}Ga_{0.82}As$ MOS-based structure, and has eight 2 μm wide input and output waveguides that expand to (or taper from, respectively) a width of 3 μm towards the FPR over a 50 μm length. The phased array section has 30 waveguides that taper from a 4 μm to 3 μm width over 50 μm, and then return to a 4 μm width at the second FPR. The simulated AWG (b) illustrates the AWG output and spatial frequency separation performance of the 4th output channel of the device.

Table 5.5: Specifications of the $Al_{0.26}Ga_{0.74}As/Al_{0.18}Ga_{0.82}As$ MOS-based arrayed waveguide grating

Central wavelength (nm)	799.8
Modal index (I/O waveguides)	3.507
Modal Index (array waveguides)	3.513
Phasar order	1979
Dispersion (μm/GHz)	0.40
Free spectral range (nm)	0.40
Channel spacing (GHz)	9.99
Channel spacing (nm)	0.021
Diffraction loss of central channel (dB)	2.20

Chapter 6

Future Work and Summary

6.1 Future Work

Beyond demonstrating successful operation of electro-optic modulators, the purpose of this work is to design highly efficient, fast and reliable integrated devices that can manipulate the individual frequencies within a frequency comb to produce arbitrary optical waveforms. Future devices will involve multiple modulators functioning in unison, which provokes concerns of excessive heating, low-speed execution, signal crosstalk and noise. Several modifications, presented in the following sections, to the current designs can be pursued to enhance performance and minimize sensitivity to fabrication.

6.1.1 Traveling Wave Modulator

The pursuit of high speed electro-optic modulators is largely limited by the electrical bandwidth that is determined by capacitance across the P-I-N junction and the device resistance-capacitance time constant as a result of the metal electrodes. There are two methods of reducing capacitance - 1) minimization of device dimensions, though this technique is known to adversely affect the optical behavior and capabilities [42], and 2) a traveling wave design in which the phase velocities of the modulated optical and modulating microwave signals are matched, overcoming the RC time constant

constraints and achieving high electrical bandwidths. The latter is mainly limited by microwave losses that may be alleviated by matching the electrode and microwave source impedances [43], which should be in the vicinity of 50 Ω.

There are several considerations in designing a traveling wave modulator. Although the optical mode is strictly confined to the semiconductor layers and therefore sees only the device's effective index of refraction, the microwave electric field generated by powered coplanar strips travels through an effective index that is a combination of the device and that of air (where the fringes are). As a result, the effective index of refraction felt by the microwave electric field is lower than that of the optical signal [44]. The index mismatch is remedied by the use of a slow wave transmission line in which the coplanar strips are capacitively loaded in order to reduce microwave signal velocity and to achieve velocity matching between the microwave and optical signals. In addition, any overlap between the doped semiconductor layers and the electric field should be minimized to prevent unwanted slow wave effects as explained by Walker [21].

The characteristic impedance, Z_u, and phase velocity, v_{pu}, of an unloaded transmission line are related to the transmission line inductance and capacitance through

$$Z_u = \sqrt{\frac{L}{C_u}} \tag{6.1}$$

and

$$v_{pu} = \frac{1}{\sqrt{LC_u}} = \frac{c_0}{n_u} \tag{6.2}$$

where c_0 is the speed of light in free space and n_u is the microwave index of refraction of the transmission line. With the addition of capacitors to load the transmission line, the impedance, Z_0, and phase velocity, v_p respectively become

$$Z_0 = \sqrt{\frac{L}{C}} \tag{6.3}$$

and

$$v_p = \frac{1}{\sqrt{LC}} = \frac{c_0}{n_m} \tag{6.4}$$

for $C = C_u + C_l$ (where C_l is the load capacitance per unit length) and n_m is the effective microwave index of refraction of the loaded transmission line. By setting $n_m = n_g$, where n_g is the optical waveguide group index of refraction, the condition for velocity matching is satisfied. The C_l required for velocity matching is provided by

$$C_l = \frac{n_g^2 - n_u^2}{c_0 Z_0 n_g} \tag{6.5}$$

6.1.2 Phase Tuning of Arrayed Waveguide Gratings

Arrayed waveguide gratings (AWG) are designed with a certain frequency and wavelength spacings in mind that are obtained through specially calculated waveguide lengths and bends. As the AWG pattern is transferred to the grown structure by photolithography and reactive ion etching steps, a less than ideal fabrication process may result in a wider or narrower bend angles or different spatial waveguide spacings than intended. Consequently, random phase errors in the form of frequency channel crosstalk during the frequency channel separation and combination are a concern. Phase tuning of each individual waveguide within the AWG can correct the effects of less than ideal fabrication, and can be implemented by 1) placing electrodes along the straight waveguides and tuning them electrically with voltage sources, or 2) engaging resistive heaters to change device temperature and induce a change in the effective index and wavelength of the waveguide. Both techniques are equally viable and carry challenges, especially the potential that the tuning of one waveguide by electrical or thermal sources may in turn affect nearby waveguides. However, the methods are extremely promising and will be further explored in the future.

6.1.3 Fabrication Tolerance by Redundancy

The fabrication process detailed in Chapter 4, from structure growth by MBE to the contact anneal, consists of many steps that may result in the formation of defects that ultimately hinder device operation. The large scale of the Mach-Zehnder interferometers and waveguides adds further challenges, and it is therefore essential to introduce

designs that improve yield under the same difficult conditions. By cascading modulators and y-splitters so that only two of four modulator arms must be operational for a successful device, the design becomes more tolerant of processing discrepancies that could otherwise result in a failed device.

6.2 Summary

The design and fabrication of ultra-broadband modulators operating at a wavelength of 800 nm has been presented. Four heterostructures were proposed and their operation simulated. A process flow was developed and experiments were carried out to optimize fabrication techniques. The layout and simulation of an arrayed waveguide grating in preparation for future device integration to generate arbitrary waveforms was also illustrated. Characterization of passive and active modulator performance is currently underway.

Appendix A

Electro-optic Effect in the Modulator Heterostructure

As discussed in Section 2.2.4, an electro-optic tensor matrix of the form

$$\begin{pmatrix} r_{11} & r_{12} & r_{13} \\ r_{21} & r_{22} & r_{23} \\ r_{31} & r_{32} & r_{33} \\ r_{41} & r_{42} & r_{43} \\ r_{51} & r_{52} & r_{53} \\ r_{61} & r_{62} & r_{63} \end{pmatrix}$$

describes the electro-optic coefficients for a general material. Crystals with inversion symmetry will have all $r_{ij} = 0$, but bulk GaAs, InP and any crystals based upon them lack inversion symmetry, and therefore have an electro-optic tensor matrix of the form

$$\begin{pmatrix} 0 & 0 & 0 \\ 0 & 0 & 0 \\ 0 & 0 & 0 \\ r_{41} & 0 & 0 \\ 0 & r_{52} & 0 \\ 0 & 0 & r_{63} \end{pmatrix}$$

As a result, the matrix form of equation 2.24 for a bulk GaAs layer is

$$\begin{pmatrix} \Delta\frac{1}{n_x^2} \\ \Delta\frac{1}{n_y^2} \\ \Delta\frac{1}{n_z^2} \\ \Delta\frac{1}{n_{yz}^2} \\ \Delta\frac{1}{n_{xz}^2} \\ \Delta\frac{1}{n_{xy}^2} \end{pmatrix} = \begin{pmatrix} 0 & 0 & 0 \\ 0 & 0 & 0 \\ 0 & 0 & 0 \\ r_{41} & 0 & 0 \\ 0 & r_{52} & 0 \\ 0 & 0 & r_{63} \end{pmatrix} \begin{pmatrix} E_1 \\ E_2 \\ E_3 \end{pmatrix}$$

where $r_{41} = r_{63}$, but the y axis coefficient remains r_{52} due to the uniaxial nature of the material. Though $\Delta\frac{1}{n_{xz}^2}$ exists due to r_{52}, $\Delta\frac{1}{n_x^2}$ and $\Delta\frac{1}{n_z^2}$ do not. In a bulk semiconductor, there are no contributions from individual axes and their corresponding electro-optic tensors, and the plane descriptors alone represent the changes in the layer.

In the case of heterostructures, the electro-optic tensor matrix is more complex. Instead of examining the effects of a y-directed electric field only on the index of refraction in the xz plane corresponding to r_{52}, there is now reason to look at the effects on the x and z axes as well. In a heterostructure, it is necessary to examine both the inter-layer and inter-axial dynamics closely.

The induced refractive index within a heterostructure is now considered. Though a heterostructure is composed of symmetric crystals, it does not exhibit the same symmetry due to its composition. As a result, new terms are introduced into its tensor matrix. Each r_{ij} represents an overall effective electro-optic coefficient composed of a combination of the electro-optic coefficients of the various layers in the structure.

Equation 2.24 is now configured as

$$\begin{pmatrix} \Delta\frac{1}{n_x^2} \\ \Delta\frac{1}{n_y^2} \\ \Delta\frac{1}{n_z^2} \\ \Delta\frac{1}{n_{yz}^2} \\ \Delta\frac{1}{n_{xz}^2} \\ \Delta\frac{1}{n_{xy}^2} \end{pmatrix} = \begin{pmatrix} 0 & r_{12} & r_{13} \\ r_{21} & 0 & r_{23} \\ r_{31} & r_{32} & 0 \\ r_{41} & 0 & 0 \\ 0 & r_{52} & 0 \\ 0 & 0 & r_{63} \end{pmatrix} \begin{pmatrix} E_1 \\ E_2 \\ E_3 \end{pmatrix}$$

With an electric field applied in the y-direction, the index ellipsoid Equation 2.26 becomes

$$x^2\left(\frac{1}{n^2}+r_{12}E_y\right)+\frac{y^2}{n_e^2}+z^2\left(\frac{1}{n^2}+r_{32}E_y\right)+2r_{52}E_yxz=1 \tag{A.1}$$

and may also be expressed in the recognizable index ellipsoid form as

$$\frac{x^2}{n^2}+\frac{y^2}{n_e^2}+\frac{z^2}{n^2}+r_{12}E_yx^2+r_{32}E_yz^2+2r_{52}E_yxz=1 \tag{A.2}$$

Individual contributions to the induced index of refraction in both the x and z axes are now visible. The expressions are translated into the new x' and z' using the coordinate system provided in Equations 2.27 and 2.28. The 45° rotation of the index ellipsoid is still valid for a heterostructure if $n_x = n_z$ and $r_{12} = r_{32}$. The heterostructures designed in this work exhibit $n_x \approx n_z$ (to the order of 10^{-3}), and it is assumed for the sake of calculations (as the true values are unknown) that $r_{12} = r_{32}$. After the rotation of the index ellipsoid, the mixed term due to the electric field remains the same as in Equation 2.31, but the x^2 and z^2 terms now appear as

$$x^2=\frac{x^2}{2}+\frac{z^2}{2}-x'z' \tag{A.3}$$

$$z^2=\frac{x^2}{2}+\frac{z^2}{2}+x'z' \tag{A.4}$$

The combination of Equations 2.32, A.2, A.3 and A.4 yields

$$\begin{aligned} 1 &= x'^2\left(\frac{1}{n_o^2}+r_{52}E_y+r_{12}E_y+r_{32}E_y\right)+\frac{y^2}{n_e^2} \\ &\quad +z'^2\left(\frac{1}{n_o^2}-r_{52}E_y+r_{12}E_y+r_{32}E_y\right) \\ &\quad -r_{12}E_yx'z'+r_{32}E_yx'z' \end{aligned}$$

As r_{12} and r_{32} are likely of the same order of magnitude, the sum of the $x'z'$ plane terms $-r_{12}E_y+r_{32}E_y \approx 0$, so that the former equation is written as

$$x'^2\left(\frac{1}{n_o^2}+r_{52}E_y+r_{12}E_y+r_{32}E_y\right)+\frac{y^2}{n_e^2}+z'^2\left(\frac{1}{n_o^2}-r_{52}E_y+r_{12}E_y+r_{32}E_y\right)=1 \tag{A.5}$$

If this form is compared to that of Equation 2.22, we arrive at the conclusion that

$$\Delta\frac{1}{n_{x'}^2}=r_{52}E_y+r_{12}E_y+r_{32}E_y \tag{A.6}$$

and

$$\Delta\frac{1}{n_{z'}^2}=-r_{52}E_y+r_{12}E_y+r_{32}E_y \tag{A.7}$$

The general expressions for the overall induced index of refraction in both the x' and z' directions is given by

$$n_{x'}=n_0+\Delta n_{x'}^{eff} \tag{A.8}$$

$$n_{z'}=n_0+\Delta n_{z'}^{eff} \tag{A.9}$$

In a bulk semiconductor, $|\Delta n_{x'}^{eff}|=|\Delta n_{z'}^{eff}|$. However, it is clear from Equations A.6 and A.7 that within a heterostructure, $|\Delta n_{x'}^{eff}| \neq |\Delta n_{z'}^{eff}|$ due to lack of symmetry.

By linearization, we arrive at the following expressions for the field-induced change in the index of refraction in the x' and z axes respectively:

$$\Delta n_{x'}^{eff}=-\frac{1}{2}n^3\Delta\frac{1}{n_{x'}^2}=-\frac{1}{2}n^3E_y(r_{52}+r_{12}+r_{32}) \tag{A.10}$$

$$\Delta n_{z'}^{eff} = -\frac{1}{2}n^3\Delta\frac{1}{n_{z'}^2} = -\frac{1}{2}n^3E_y(-r_{52}+r_{12}+r_{32}) \tag{A.11}$$

Finally, this equation may be applied to the former expressions for $n_{x'}$ and $n_{z'}$ to obtain the full expressions for the resulting indices of refraction in the x' and z' directions:

$$n_{x'} = n_0 - \frac{1}{2}n^3E_y(r_{52}+r_{12}+r_{32}) \tag{A.12}$$

$$n_{z'} = n_0 - \frac{1}{2}n^3E_y(-r_{52}+r_{12}+r_{32}) \tag{A.13}$$

As the contributions from the r_{12} and r_{32} electro-optic coefficients are equal in the x' and z' directions, it is possible to extract r_{52} by measuring the phase shift difference between the TE modes in the x' and z' directions. This is achieved by inducing a change in the refractive index in both directions to produce $n_{x'}$ and $n_{z'}$, and then subtracting Equation A.12 from Equation A.13, yielding

$$n_{z'} - n_{x'} = n^3E_yr_{52} \rightarrow r_{52} = \frac{n_{z'}-n_{x'}}{n^3E_y} \tag{A.14}$$

A TE mode in the x' direction will experience a phase shift due to $n_{x'}$ given by

$$\Delta\beta = |\Delta n_{x'}^{eff}|k_0 \tag{A.15}$$

The total phase shift due to an applied electric field E_y over a heterostructure waveguide of length L is defined by

$$\Delta\phi_{x'} = \Delta\beta L = |\Delta n_{x'}^{eff}|k_0L \tag{A.16}$$

By substituting the expression for $\Delta n_{x'}^{eff}$, the former equation takes the form

$$\Delta\phi_{x'} = \frac{2\pi}{\lambda}\frac{Ln^3E_y(r_{52}+r_{12}+r_{32})}{2} \tag{A.17}$$

The total phase shift due to $n_{z'}$ for a TE mode in the z' direction is similarly described

by

$$\Delta\phi_{z'} = \frac{2\pi}{\lambda}\frac{Ln^3E_y(-r_{52}+r_{12}+r_{32})}{2} \tag{A.18}$$

The TE mode of a waveguide oriented along the $< 011 >$ direction will experience a phase shift due to E_y given by $\Delta\phi_{x'}$. Therefore, the voltage required to produce a phase shift of π is provided by

$$V_\pi = \lambda\frac{t_g}{Ln^3[r_{52}+r_{12}+r_{32}]} \tag{A.19}$$

The following tables present computed values of V_π for the various modulators introduced in this work.

Table A.1: Calculated values of V_π for both shallow and deep-etched devices of various lengths oriented in the $< 011 >$ direction. This calculation assumes $r_{12} = r_{32} = r_{52} = 1.4 \cdot 10^{-12}$ m/V.

Device Length (mm)	3.0	4.5	6.0	7.5	9.0	10.5
Shallow Device Voltage (V)	5.08	3.39	2.54	2.03	1.69	1.45
Deep Device Voltage (V)	4.89	3.26	2.44	1.96	1.63	1.40

Table A.2: Calculated values of V_π for both shallow and deep-etched devices of various lengths oriented in the $< 011 >$ direction. This calculation assumes $r_{12} = r_{32} = r_{52} = 0.7 \cdot 10^{-12}$ m/V.

Device Length (mm)	3.0	4.5	6.0	7.5	9.0	10.5
Shallow Device Voltage (V)	10.16	6.78	5.08	4.07	3.39	2.90
Deep Device Voltage (V)	9.78	6.52	4.89	3.91	3.26	2.79

Table A.3: Calculated values of V_π for both shallow and deep-etched devices of various lengths oriented in the < 011 > direction. This calculation assumes $r_{12} = r_{32} = 0$ m/V and $r_{52} = 1.0 \cdot 10^{-12}$ m/V, corresponding to the behavior of a bulk semiconductor modulator.

Device Length (mm)	3.0	4.5	6.0	7.5	9.0	10.5
Shallow Device Voltage (V)	21.34	14.23	10.67	8.54	7.11	6.10
Deep Device Voltage (V)	20.53	13.70	10.27	8.21	6.84	5.87

Table A.4: Calculated values of V_π for $Al_{0.8}Ga_{0.2}As/In_{0.53}Ga_{0.47}P$ MOS devices of various lengths oriented in the < 011 > direction. This calculation assumes $r_{12} = r_{32} = r_{52} = 1.4 \cdot 10^{-12}$ m/V.

Device Length (mm)	3.0	4.5	6.0	7.5	9.0	10.5
MOS Device Voltage (V)	2.68	1.79	1.34	1.07	0.89	0.77

Table A.5: Calculated values of V_π for $Al_{0.8}Ga_{0.2}As/In_{0.53}Ga_{0.47}P$ MOS devices of various lengths oriented in the < 011 > direction. This calculation assumes $r_{12} = r_{32} = r_{52} = 0.7 \cdot 10^{-12}$ m/V.

Device Length (mm)	3.0	4.5	6.0	7.5	9.0	10.5
MOS Device Voltage (V)	5.36	3.57	2.68	2.14	1.79	1.53

Table A.6: Calculated values of V_π for $Al_{0.8}Ga_{0.2}As/In_{0.53}Ga_{0.47}P$ MOS devices of various lengths oriented in the < 011 > direction. This calculation assumes $r_{12} = r_{32} = 0$ m/V and $r_{52} = 1.0 \cdot 10^{-12}$ m/V, corresponding to the behavior of a bulk semiconductor modulator.

Device Length (mm)	3.0	4.5	6.0	7.5	9.0	10.5
MOS Device Voltage (V)	11.25	7.50	5.63	4.50	3.75	3.22

Table A.7: Calculated values of V_π for $Al_{0.26}Ga_{0.74}As/Al_{0.18}Ga_{0.82}As$ MOS devices of various lengths oriented in the < 011 > direction. This calculation assumes $r_{12} = r_{32} = r_{52} = 1.4 \cdot 10^{-12}$ m/V.

Device Length (mm)	3.0	4.5	6.0	7.5	9.0	10.5
All AlGaAs MOS Device Voltage (V)	1.83	1.22	0.92	0.73	0.61	0.52

Table A.8: Calculated values of V_π for $Al_{0.26}Ga_{0.74}As/Al_{0.18}Ga_{0.82}As$ MOS devices of various lengths oriented in the $< 011 >$ direction. This calculation assumes $r_{12} = r_{32} = r_{52} = 0.7 \cdot 10^{-12}$ m/V.

Device Length (mm)	3.0	4.5	6.0	7.5	9.0	10.5
All AlGaAs MOS Device Voltage (V)	3.66	2.44	1.83	1.47	1.22	1.05

Table A.9: Calculated values of V_π for $Al_{0.26}Ga_{0.74}As/Al_{0.18}Ga_{0.82}As$ MOS devices of various lengths oriented in the $< 011 >$ direction. This calculation assumes $r_{12} = r_{32} = 0$ m/V and $r_{52} = 1.0 \cdot 10^{-12}$ m/V, corresponding to the behavior of a bulk semiconductor modulator.

Device Length (mm)	3.0	4.5	6.0	7.5	9.0	10.5
MOS Device Voltage (V)	7.69	5.13	3.85	3.08	2.57	2.20

Appendix B

Modulator Process

- Photolithography exposures require a prior blank exposure of a dummy wafer to determine bulb intensity and adjust exposure time accordingly.
- Similarly, a dummy wafer is first used in PECVD deposition to examine the layer quality and chamber cleanliness.
- Solvent cleans are performed often, and consist of a rinse in acetone/methanol/isopropanol and drying by nitrogen. The clean removes particles and debris (fundamental problems in fabrication) and is an essential component of the process.
- Prior to a BCl_3 etch, the CF_4/O_2 clean and CHF_3/O_2 runs may require repetition for a sufficiently clean chamber.

Photolithography: Employs the first mask to define the MZ modulator arms

1. Dehydration bake: 20 min, 95°C oven
2. Resist spin: AZ5214 Image reversal resist, 1.4 μm thick

Dispense: 500 rpm, 6 sec

Spread: 750 rpm, 6 sec

Spin: 4k rpm, 30 sec

3. Prebake: 35 min, 95°C oven
4. Exposure: Dosage$\approx$13.95 mJ/cm^2, Electronic Visions 620
5. Reversal Bake: 60 sec, 106°C hotplate (with aluminum plate)

6. Flood exposure: Dosage≈560 mJ/cm^2

7. Development: 55 sec, AZ422 developer; 30 sec H_2O rinse

Metal Deposition: Evaporation of hard mask metal over MZ arms to protect contact interface

8. Chamber clean: 3 min, CF_4/O_2 4 sccm/20 sccm, 300 V

9. Plasma ashing: He/O_2 5 sccm/10 sccm, 20 mTorr, 150 W, 10 sec

10. Electron beam evaporation: Ni (100 nm)

11. Lift off: Soak in either acetone or 80°C n-methylpyrrolidine

12. Clean: Solvent rinse, spin dry

III-V reactive ion etch: Remove unprotected, doped GaAs and AlGaAs layers to prevent device shorting

13. Chamber clean: CF_4/O_2 10.8 sccm/23.8 sccm, 36 mTorr, 59 W, continued until voltage drops below 290 V

14. Chamber coating: 20 min, CHF_3/O_2 16.2 sccm/4.1 sccm, 11 mTorr, 250 V

15. Chamber conditioning: 20 sec, BCl_3 15 sccm, 11 mTorr, 320 V

16. Etch: 8 min, BCl_3 13 sccm, 11 mTorr, 390 V

Oxide Deposition: 250 nm layer of high frequency SiO_x serves as protection for passive devices during second III-V etch

17. Deposition: 295 sec (8.45 Å /sec rate deposition rate), 550 mTorr, 300°C platen, 250°C shower head, 30 W, 13.56 MHz;
N_2O (1420 sccm), N_2 (392 sccm), SiH_4 (12 sccm)

Photolithography: Employs the second mask to define passive waveguides and power splitters

18. HMDS

19. Resist spin: AZ5214 Image reversal resist, 1.4 μm thick
Dispense: 500 rpm, 6 sec

Spread: 750 rpm, 6 sec

Spin: 4k rpm, 30 sec

20. Prebake: 35 min, 95°C oven
21. Exposure: Dosage≈13.95 mJ/cm^2, Electronic Visions 620
22. Reversal Bake: 60 sec, 106°C hotplate (with aluminum plate)
23. Flood exposure: Dosage≈560 mJ/cm^2
24. Development: 55 sec, AZ422 developer; 30 sec H_2O rinse

Oxide reactive ion etch: Transfers photoresist pattern to oxide hard mask

25. Chamber clean: 3 min, CF_4/O_2 4 sccm/20 sccm, 300 V
26. Plasma ashing: He/O_2 5 sccm/10 sccm, 20 mTorr, 150 W, 10 sec
27. Oxide etch: 9 min (30 nm/min etch rate), CF_4 15 sccm, 10 mTorr, 50 V
28. Resist removal: Soak in either acetone or 80°C n-methylpyrrolidine followed by a short ashing

III-V reactive ion etch: Define ridges and passive devices

29. Chamber clean: CF_4/O_2 10.8 sccm/23.8 sccm, 36 mTorr, 59 W, continued until voltage drops below 290 V
30. Chamber coating: 20 min, CHF_3/O_2 16.2 sccm/4.1 sccm, 11 mTorr, 250 V
31. Chamber conditioning: 20 sec, BCl_3 15 sccm, 11 mTorr, 320 V
32. Etch: BCl_3 13 sccm, 11 mTorr, 390 V

Planarization: Evens surface topology in preparation for top-contact evaporation

33. Clean: Solvent rinse, dry with N_2
34. Dehydration bake: 15-20 min, 130°C oven
35. Adhesion layer: AP3000, static dispense, spread 300 rpm (5 sec), spin 2-3k rpm (20 sec)
36. Bake: 5 min, 100° hotplate
37. BCB application: Static dispense, spread 500-750 rpm (5 sec), spin 3k rpm (25 sec)

38. Bake: 1 min, 100° hotplate

39. Curing: Anneal tube furnace

Flow N_2 >20 scfh for 30 min

Ramp temperature to 250°C , set N_2 flow to 5-15 scfh

60 min at 250°, ramp down to room temperature

BCB Etchback: Etch of BCB to reveal MZ modulator arms

40. BCB etch: CF_4/O_2 12 sccm/8 sccm, 15 mTorr, 100V (etch rate 90-100 nm/min). Inspect with microscope to track progress.

Photolithography: Employs the fourth mask to define the top metal contacts

41. Resist spin: AZ5214 Image reversal resist, 1.4 μm thick

Dispense: 500 rpm, 6 sec

Spread: 750 rpm, 6 sec

Spin: 4k rpm, 30 sec

42. Prebake: 35 min, 95°C oven

43. Exposure: Dosage≈13.95 mJ/cm^2, Electronic Visions 620

44. Reversal Bake: 60 sec, 106°C hotplate (with aluminum plate)

45. Flood exposure: Dosage≈560 mJ/cm^2

46. Development: 55 sec, AZ422 developer; 30 sec H_2O rinse

Metal Deposition: Evaporation of top metal contacts over MZ arms

47. Electron beam evaporation: Ti/Pt/Au (300 Å, 200 Å, 2000 Å)

48. Lift off: Soak in either acetone or 80°C n-methylpyrrolidine

49. Clean: Solvent rinse, spin dry

Backside Processing: Lapping of substrate and backside metal deposition

50. Resist spin: AZ5214 Image reversal resist Dispense: 500 rpm, 6 sec

Spread: 750 rpm, 6 sec

Spin: 4k rpm, 30 sec

51. Resist Bake: 30 min, 95°C, oven 52. Backside lapping: Mount sample on glass chuck using a thin film bonding wax

Remove excess wax, rinse with TCE, isopropanol

Lap substrate with grit to 175 μm thickness

Rinse sample thoroughly with H_2O

53. Polish backside: H_2SO_4:H_2O_2:H_2O (3:1:1) (etch rate of 5.9 μm/min in water bath)

54. Electron beam evaporation of backside contact: Ge/Au/Ni/Au (300 Å, 600 Å, 300 Å, 2000 Å)

55. Dismount sample from chuck: Heat TCE and clean off wax.

56. Rapid thermal anneal: Temperature no higher than 400°C

Appendix C

Experiments

Photolithography and Metal Lift Off

Previous process: Resist coating: samples are coated with AZ5214: Dispense 500 rpm (6 sec), spread 750 rpm (6 sec), spin 4k rpm (30 sec)

Prebake: 35 min, 95°C oven

Exposure: 7 mJ/cm^2 <Dosage< 18 mJ/cm^2 (varied greatly), Electronic Visions 620

Reversal Bake: 30 min, 95°C oven

Flood exposure: Dosage≈560 mJ/cm^2

Development: 90 sec, AZ422 developer; 30 sec H_2O rinse

Optimized Photolithography

Prebake:

Table C.1: Evaluation of AZ5214 photoresist pre-bake

Temperature	Duration	Method
95°C	30 min	oven
95°C	35 min	oven

A longer prebake solidifies photoresist sufficiently and prevents it from adhering to the mask during contact photolithography.

Reversal bake (Experiment 1):

Samples were coated with AZ5214. Samples were positioned on an aluminum plate for the hotplate reversal bake. The ideal image reversal bake is in the temperature

Table C.2: Determining the 5°c range for AZ5214 photoresist reversal bake temperature

Prebake	Reversal bake	Flood Exposure	Resist removed
95°C, 35 min; oven	95°C, 60 sec; hotplate	60 sec	Yes
95°C, 35 min; oven	100°C, 60 sec; hotplate	60 sec	Yes
95°C, 35 min; oven	105°C, 60 sec; hotplate	60 sec	Yes
95°C, 35 min; oven	110°C, 60 sec; hotplate	60 sec	No

range of 105°C to 110°C.

Reversal bake (Experiment 2):

Samples were coated with AZ5214 and prebaked at 95°C for 35 min in an oven. A first exposure with the Electronic Visions 620 aligner provided a dosage of 13.95 mJ/cm^2. A 106°C, 60 sec hotplate bake is the proper image reversal bake.

Table C.3: Determining the accurate AZ5214 photoresist reversal bake temperature

Exposure	Reversal bake	Flood Exposure
1.5 sec	105°C, 60 sec; hotplate	60 sec
1.5 sec	106°C, 60 sec; hotplate	60 sec
1.5 sec	107°C, 60 sec; hotplate	60 sec
1.5 sec	108°C, 60 sec; hotplate	60 sec

Table C.4: Evaluation of Hard Mask Metals

Material(s)	**Thickness**	**Result**
Ti/Ni/Pt	500 Å/2000 Å/500 Å	Peeled off
Ti/Ni/Pt	500 Å/1500 Å/500 Å	Peeled off
Ni	500 Å	Successful lift off
Ni	2000 Å	Peeled off
Ni	1000 Å	Successful lift off

References

[1] S.T. Cundiff and J. Ye. Femtosecond optical frequency combs. *Reviews of Modern Physics*, 75:325–342, 2003.

[2] G. Lengyel, K.W. Jelley, and R.W.H. Engelmann. A Semi-Empirical Model for Electroabsorption in GaAs/AlGaAs Multiple Quantum Well Modulator Structures. *Journal of Quantum Electronics*, 26(2):296–304, 1990.

[3] C. Thirstrup. Refractive Index Modulation Based on Excitonic Effects in GaInAs-InP Coupled Asymmetric Quantum Wells. *Journal of Quantum Electronics*, 31(6):988–996, 1995.

[4] E.F. Schubert. *Light Emitting Diodes [Electronic Version]*. Cambridge University Press, 2003.

[5] Ryan D. Williams. *Photonic Integrated Circuits for Optical Logic Applications*. PhD thesis, MIT, Cambridge, MA, 2007.

[6] M.K. Smit and C. Van Dam. PHASAR-Based WDM-Devices: Principles, Design and Applications. *Journal of Selected Topics in Quantum Electronics*, 2(2):236–250, 1996.

[7] F. Riehle. *Frequency Standards: Basics and Applications*. Wiley-VCH, 2006.

[8] S.T. Cundiff, J. Ye, and J.L. Hall. Optical frequency synthesis based on mode-locked lasers. *Review of Scientific Instruments*, 72(10):3749–3771, 2001.

[9] T. Brown and W. Sibbett. *Ultrafast Photonics*. CRC Press, 2004.

[10] M.S. Leeson, F.P. Payne, R.J. Mears, J.E. Carroll, J.S. Roberts, M.A. Pate, and G. Hill. Design and Fabrication of Planar Resonant Franz-Keldysh Optical Modulator. *Electronic Letters*, 24(25):1546–1547, 1988.

[11] B. Kïupfer, P. Kiesel, M. Kneissl, S. Dankowski, N. Linder, G. Weimann, and G.H. Döhler. Polarization-Insensitive High-Contrast GaAs/AlGaAs Waveguide Modulator Based on the Franz-Keldysh Effect. *Photonics Technology Letters*, 5(12):1386–1388, 1993.

[12] E.J. Murphy. *Integrated Optical Circuits and Components: Design and Applications*. CRC Press, 1999.

[13] T.E. Van Eck, L.M. Walpita, W.S.C. Chang, and H.H. Wieder. Franz-Keldysh electrorefraction and electroabsorption in bulk InP and GaAs. *Applied Physics Letters*, 48:451–453, 1986.

[14] L. Viña, E.E. Mendez, W.I. Wang, L.L. Chang, and L. Esaki. Stark Shifts in GaAs/GaAlAs quantum wells studied by photoluminescence spectroscopy. *Journal of Physics C: Solid State Physics*, 20(18):2803–2815, 1987.

[15] J.A. Brum and G. Bastard. Electric-field-induced dissociation of excitons in semiconductor quantum wells. *Physical Review B*, 31(6):3893–3898, 1985.

[16] M.S. Tobin and J.D. Bruno. Quantum-confined Stark effect modulator based on multiple triple-quantum wells. *Journal of Applied Sciences*, 89(3):1885–1889, 2001.

[17] W.H. Chen, W.K. Kuo, S.L. Huang, and Y.T. Huang. On-Wafer Electrooptic Probing Using Rotational Deformation Modulation. *Photonic Technology Letters*, 12(9):1228–1230, 2000.

[18] C.R. Pollock. *Fundamentals of Optoelectronics*. Irwin, 1995.

[19] R.C. Alferness. Waveguide Electrooptic Modulators. *Transactions on Microwave Theory and Techniques*, 30(8):1121–1137, 1982.

[20] R.G. Hunsperger. *Integrated Optics: Theory and Technology*. Springer, 2002.

[21] R.G. Walker. High-Speed III-V Semiconductor Intensity Modulators. *Journal of Quantum Electronics*, 27(3):654–667, 1991.

[22] A. Markina. *Design and Simulation for the Fabrication of Integrated Semiconductor Optical Logic Gates*. PhD thesis, MIT, Cambridge, MA, 2005.

[23] G.R. Hadley and R.E. Smith. Full-Vector Waveguide Modeling Using an Iterative Finite-Difference Method with Transparent Boundary Conditions. *Journal of Lightwave Technology*, 13(3):465–469, 1995.

[24] G.R. Hadley. Transparent Boundary Condition for the Beam Propagation Method. *Journal of Quantum Electronics*, 28(1):363–370, 1992.

[25] P.-L. Liu and B.-J. Li. Semivectorial Beam-Propagation Method for Analyzing Polarized Modes of Rib Waveguides. *Journal of Quantum Electronics*, 28(4):778–782, 1992.

[26] Y.-L. Hsueh, M.-C. Yang, and H.-C. Chang. Three-Dimensional Noniterative Full-Vectorial Beam Propagation Method Based on the Alternating Direction Implicit Method. *Journal of Lightwave Technology*, 17(11):2389–2397, 1999.

[27] R. Scarmozzino and R.M. Osgood Jr. Comparison of finite-difference and Fourier-transform solutions of the parabolic wave equation with emphasis on integrated-optics applications. *Journal of the Optical Society of America A*, 8(5):724–731, 1991.

[28] N.-N. Feng, G.-R. Zhou, C. Xu, and W.-P. Huang. Computation of Full-Vector Modes for Bending Waveguide Using Cylindrical Perfectly Matched Layers. *Journal of Lightwave Technology*, 20(11):1976–1980, 2002.

[29] F.L. Teixeira and W.C. Chew. PML-FDTD in Cylindrical and Spherical Grids. *Microwave and Guided Wave Letters*, 7(9):285–287, 1997.

[30] W.W. Lui, C.-L. Xu, T Hirono, K. Yokoyama, and W.-P. Huang. Full-vectorial wave propagation in semiconductor optical bending waveguides and equivalent straight waveguide approximations. *Journal of Lightwave Technology*, 16(5):910–914, 1998.

[31] S. Adachi. *GaAs and Related Materials: Bulk Semiconducting and Superlattice Properties.* World Scientific, 1994.

[32] P. Bhattacharya. *Semiconductor Optoelectronic Devices.* Prentice Hall, 1994.

[33] L.B. Freund and W.D. Nix. A critical thickness condition for a strained compliant/epitaxial film system. *Applied Physics Letters*, 69(2):173–175, 1996.

[34] J.W. Matthews and A.E. Blakeslee. Defects in epitaxial multilayers: I. misfit dislocations. *Journal of Crystal Growth*, 27:118–125, 1974.

[35] L.L. Chang and K. Ploog. *Molecular Beam Epitaxy and Heterostructure.* Springer, 1985.

[36] R.G. Walker, I. Bennion, and A.C. Carter. Low-Voltage, 50 Ω, GaAs/AlGaAs Travelling-Wave Modulator with Bandwidth Exceeding 25GHz. *Electronic Letters*, 25(23):1549–1550, 1989.

[37] J. P. Dakin and R.G. Brown. *Handbook of Optoelectronics.* CRC Press, 2006.

[38] C.E. Zah, J.S. Osinski, C. Caneau, S.G. Menocal, L.A. Reith, J. Salzman, F.K. Shokoohi, and T.P. Lee. Fabrication and Performance of 1.5 μm GaInAsP Travelling-Wave Laser Amplifiers with Angles Facets. *Electronic Letters*, 23(19):990–992, 1987.

[39] R. Kirchoff, C. Carriere, K. Bruza, N. Rondan, and R. Sammler. Benzocyclobutenes: A New Class of High Performance Polymers. *Journal of Macromolecular Science. Part A: Pure and Applied Chemistry*, 28:1079–1113, 1991.

[40] Zheng Cui. *Micro-Nanofabrication Technologies and Applications.* Springer, 2005.

[41] G. Franz, W. Hösler, and R. Treichler. Sidewall passivation of GaAs in BCl_3-containing atmospheres. *Journal of Vacuum Science and Technology B*, 19(2):415–419, 2001.

[42] R. Spickermann, N. Dagli, and M.G. Peters. GaAs/AlGaAs electro-optic modulator with bandwidth >40GHz. *Electronic Letters*, 31(11):915–916, 1995.

[43] Y. Cui and P. Berini. Modeling and Design of GaAs Traveling-Wave Electrooptic Modulators Based on Capacitively Loaded Coplanar Strips. *Journal of Lightwave Technology*, 24(1):544–554, 2006.

[44] J. P. Dakin and R.G. Brown. *Handbook of Optoelectronics.* CRC Press, 2006.